# Coils, Fields and Xenon

## Towards Measuring Xenon Spin Precession in a Magnetic Field for the UCN Collaboration

by

Joshua Nikolai Wienands

Bachelor of Science, Astronomy, The University of British Columbia, 2005

A THESIS SUBMITTED IN PARTIAL FULFILLMENT
OF THE REQUIREMENTS FOR THE DEGREE OF

**Master of Science**

in

THE FACULTY OF GRADUATE AND POSTDOCTORAL STUDIES
(Physics)

The University of British Columbia
(Vancouver)

August 2016

# Abstract

In this thesis I present my work on building a set of magnetic coils for the purpose of performing nuclear magnetic resonance (NMR) on Boltzmann polarized protons in water, and on hyperpolarized $^{129}$Xe. The coils were designed to be used as a method for testing the degree of polarization achieved in $^{129}$Xe, and for testing the capability of an in-house developed continuous wave (CW) ultraviolet (UV) laser to drive a 2-photon transition in $^{129}$Xe. This laser will be used to measure the precession frequency of $^{129}$Xe in a magnetic field, in order to precisely measure the magnitude of that field.

This work is being done for the ultra-cold neutron (UCN) collaboration's flagship experiment: to measure the neutron electric dipole moment (EDM). Previous neutron EDM experiments have only found an upper limit, and have been limited in precision largely because of systematic errors in the magnetic field strength measurement. These experiments, such as the one performed at Institut Laue-Langevin (ILL), which has given us the current lowest limit, used $^{199}$Hg as a co-magnetometer. The UCN EDM experiment will add $^{129}$Xe in addition to the $^{199}$Hg, to make a dual co-magnetometer. By using multiple species of atoms in the measurement, systematic effects can be greatly reduced.

I have characterized the coils that I built by performing NMR on protons in water. I measured the inhomogeneity in the $B_0$ field, across the sample container, to be 18.9$\pm$0.9 $\mu$T. It turns out that the homogeneity of the $B_0$ field can be improved significantly, and it will likely be necessary to do so in order to perform similar experiments on hyperpolarized $^{129}$Xe. I also found the $T_1$ time of water in this setup to be 2.7$\pm$0.2 s.

# Preface

This thesis covers some of the research I did for the ultra-cold neutron (UCN) collaboration's flagship experiment, which attempts to find a non-zero value for the neutron electric dipole moment (EDM). This work was done under the supervision of Dr. David Jones and Dr. Kirk Madison at the University of British Columbia (UBC). In this thesis, there are some brief descriptions of two laser systems that are being built by Emily Altiere, in Chapter 1. A very similar system is described in detail in her thesis[1]. With permission from Emily, I have used and modified a figure created by her for my Fig. 1.6. There are also some descriptions of a $^{129}$Xe polarizer that is being built by Eric Miller, in Chapters 1 and 2.

The work described in this thesis focuses on the construction of magnetic coils that will be used to test the effectiveness of the ultraviolet (UV) lasers, and the degree of $^{129}$Xe achieved. The simulations described in Chapter 3 were coded and run by myself, with advice from Dr. Chris Bidinosti and Dr. Jeff Martin from the University of Winnipeg as to what coil geometries to pursue. The measurements in Chapter 4 were performed by myself.

# Table of Contents

# List of Tables

# List of Figures

# Glossary

**AC** alternating current

**AFP** adiabatic fast passage

**BBO** barium borate

**CW** continuous wave

**DC** direct current

**EDM** electric dipole moment

**EMF** electromotive force

**FID** free induction decay

**IC** integrated circuit

**ILL** Institut Laue-Langevin

**IR** infrared

**LBO** lithium triborate

**MDM** magnetic dipole moment

**MRI** magnetic resonance imaging

**NMR** nuclear magnetic resonance

**OPSL** optically pumped semiconductor laser

**PCB** printed circuit board

**PPM** parts per million

**RF** radio frequency

**SEOP** spin exchange optical pumping

**SNR** signal to noise ratio

**TTL** transistor-transistor logic

**UBC** the University of British Columbia

**UCN** ultra-cold neutron

**UV** ultraviolet

# Acknowledgments

I would like to thank Dr. David Jones and Dr. Kirk Madison, my supervisors, for their guidance and help during my Master's at the University of British Columbia (UBC). Thanks also to Arthur Mills, Emily Altiere and Eric Miller. Their presence in the lab, their advice, and the conversations I had with them were invaluable for the completion of this thesis. Jeff Maki, a fellow graduate student at UBC, gave me hours of his free time to help me understand the quantum mechanics involved in the optical transitions and nuclear magnetic resonance (NMR) that are described in this thesis. Thanks to Bernhard Zender, from the Physics Engineering projects lab, both for his help in using the water jet cutter, the laser cutter and the 3d printer effectively, and also for his enthusiasm in helping me, Emily Altiere and Eric Miller design and construct the apparatuses we needed to conduct our experiments.

Special thanks to Dr. Chris Bidinosti and Dr. Jeff Martin from the University of Winnipeg are also in order, for their help in my understanding of NMR, and their advice on the various possible coil geometries.

Thanks to my family, Uli, Sylvia and Robin, and to my Mother-in-law, Jennifer, and sister-in-law, Rebecca, for all of their support during my time at UBC. Thanks, finally, to my wife Kimberly, for supporting my decision to go away for two and a half years to pursue this degree. I could not have done this without your patience and understanding.

# Chapter 1

# Introduction

## 1.1 Neutron Electric Dipole Moment (EDM) Experiments

### 1.1.1 Neutron EDM

The neutron is an electrically neutral particle, but it is made up of three charged quarks (an up quark with charge +2/3, and two down quarks, each with a charge of -1/3), so there is the possibility of a non-zero electric dipole moment (EDM). The neutron is also known to have a magnetic dipole moment (MDM)[2], so a non-zero EDM would result in a violation of both parity ($P$) and time reversal ($T$) symmetry. This can be seen by analyzing the Hamiltonian of a neutron in a magnetic and electric field.

$$H = \mu_{\mathrm{n}}\mathbf{B}\cdot\frac{\mathbf{S}}{|\mathrm{S}|} - d_{\mathrm{n}}\mathbf{E}\cdot\frac{\mathbf{S}}{|\mathrm{S}|}, \tag{1.1}$$

where $\mu_{\mathrm{n}}$ is the neutron MDM, $\mathbf{B}$ the magnetic field it sits in, $\mathbf{S}/|\mathrm{S}|$ is the direction of the spin vector, $d_{\mathrm{n}}$ the neutron EDM, and $\mathbf{E}$ the electric field. Under $P$ reversal, $P(\mathbf{B}\cdot\mathbf{S}) = \mathbf{B}\cdot\mathbf{S}$ but $P(\mathbf{E}\cdot\mathbf{S}) = -\mathbf{E}\cdot\mathbf{S}$ and under $T$ reversal, $T(\mathbf{B}\cdot\mathbf{S}) = -\mathbf{B}\cdot\mathbf{S}$ but $T(\mathbf{E}\cdot\mathbf{S}) = \mathbf{E}\cdot\mathbf{S}$ [3]. In both cases, the Hamiltonian is not invariant if the neutron has both a non-zero MDM ($\mu$), and a non-zero EDM ($d$). Since the neutron is already known to have a non-zero MDM, the measurement of the neutron EDM is a useful test for fundamental symmetries in the universe. The $T$ violation is of

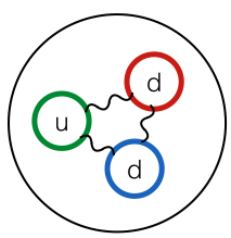


**Figure 1.1:** A neutron is made up of 3 charged quarks, an up quark with charge +2/3, and two down quarks, each with a charge of -1/3. Despite being electrically neutral, there is a possibility for the neutron to have a non-zero electric dipole moment

particular interest because under the *CPT* theorem, it also implies a *CP* violation. In the standard model, this *CP* violation comes from the weak interaction, and it predicts a neutron EDM on the order of $10^{-32}e$ cm[4]. Models beyond the standard model, such as supersymmetry theories, have additional sources of *CP* violation, and predict a larger neutron EDM. Thus, constraining this value is one test for the validity of these theories[3].

In principle, the method for measuring the neutron EDM is quite simple. A nucleus with nonzero spin, in an electric and/or magnetic field will precess over time. That is, the direction of the angular momentum of that nucleus will change. The frequency of this precession is determined by the strength of the electric and magnetic fields as well as the electric and magnetic dipole moments of the nucleus. To determine the effect from the electric field alone (and thus the EDM), the precession frequency can be measured with parallel electric and magnetic fields and then anti-parallel fields. If the magnetic field stays constant, and the electric field is flipped, the change in precession frequency can be used to calculate the EDM.

The challenge in performing this experiment comes from the scale of the neutron MDM and EDM. The neutron MDM has been measured to be $\mu_\mathrm{n} = -1.91304272(45)\mu_\mathrm{N}$, where $\mu_\mathrm{N} = 1.05155 \times 10^{-14}e$ cm is the nuclear magneton[5]. With the best constraint on the neutron EDM being $|d_\mathrm{n}| < 2.9 \times 10^{-26}e$ cm[6], this is a difference of at least 12 orders of magnitude. This massive difference makes the EDM measurement very challenging. It can be mitigated somewhat by making the magnetic field as small as possible and the electric field as large as possible, but there are practical constraints that limit this. For example, electric breakdown limits the possible strength of the electric field, and the ability to shield the experiment from external magnetic fields limits how small the experimental magnetic field can be. The difference in magnitude between the two terms is still large enough that uncertainties in the magnitude of the magnetic field term dominate over the entire value of the electric field term. For this reason, one major goal with current neutron EDM experiments is to reduce uncertainties in the measurement of the magnetic field strength. I will discuss the method the ultra-cold neutron (UCN) project is planning on using to do so in Section 1.2.

Chapters 1 and 2 will go over some of the theory of how the magnetic field measurement is performed, as well as some details about the theory of several nuclear magnetic resonance (NMR) techniques and how sources are polarized. Section 2.7.3 details which techniques are used specifically in the experiments I performed for this thesis. The time constrained reader may wish to refer to that section to help inform themselves about which theory sections to concentrate on.

### 1.1.2 Ramsey's Method of Separated Oscillating Fields

The neutron EDM is measured using Ramsey's method of separated oscillating fields. This method involves using a source of spin polarized neutrons, placed initially in a strong, static magnetic field, $\mathrm{B}_0$. The method is shown in Fig. 1.2. The coordinate system is defined such that the $z$ axis is along the $\mathrm{B}_0$ field. The spins of the polarized neutrons are initially spin up, as shown in step a). An RF $\mathrm{B}_1$ field, at the frequency of the neutrons' precession, is then applied briefly in a $\pi/2$ pulse to shift the spin vector of the neutrons into the $xy$ plane, step b). The pulse duration can be given by the following equation:

$$t_{\pi/2} = \frac{\pi}{2\gamma B_1}, \tag{1.2}$$

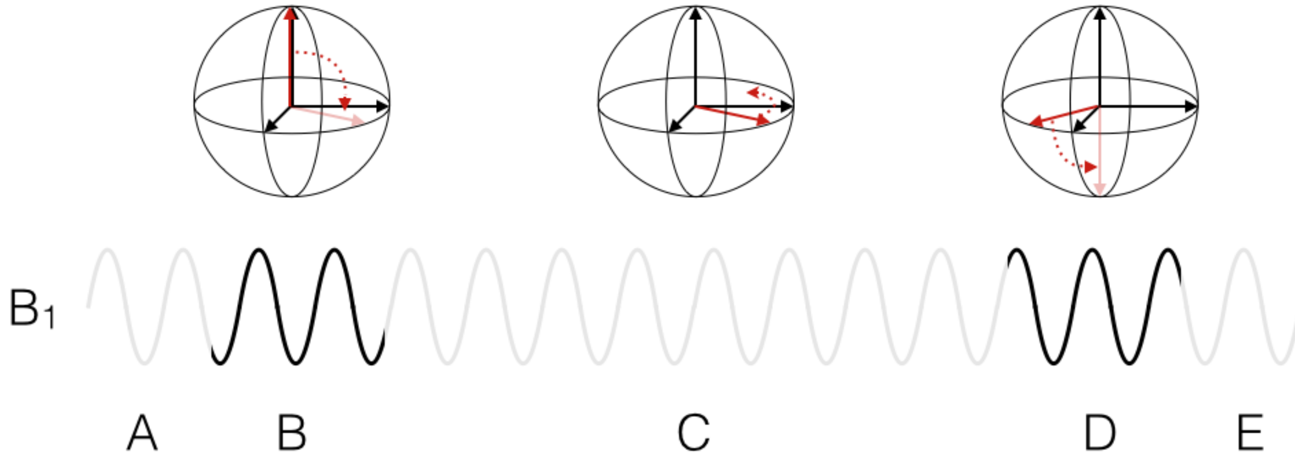


**Figure 1.2:** This is a representation of Ramsey's Method of separated oscillating fields. The top row shows a Bloch sphere representation of the particle's spin, and the second the state of the $B_1$ field. This field provides the $\pi/2$ spin flips, and for the method to work, the two flips need to be exactly in phase. The $B_1$ field is on during the darkened portions of the sine wave, and the grey shows how the phase would evolve if the field were on. A) Initially the particles are all spin up. B) An RF $\pi/2$ pulse, at the frequency that the particles precess, is applied, flipping the spin into the *xy* plane. C) The particles' spin precesses freely in the static field. D) A second $\pi/2$ pulse is applied, in phase with the first. E) If the $\pi/2$ pulses are exactly on resonance, the spin is now in the down state.

where $\gamma$ is the nucleus's gyromagnetic ratio, and $B_1$ the strength of the RF field. This is simply the Larmor precession equation, $\omega = \gamma B$, solved for the time it takes to complete $1/4$ of a period. Ideally the $B_1$ field would rotate with the precessing neutrons, but such a field is very difficult to create. Instead a field oscillating on some axis in the *xy* plane is used, with a correction to the field's strength or duration, according to the rotating wave approximation, explained in detail in Section 1.1.3.

After the initial $\pi/2$ pulse, the neutrons' spin vectors are aligned on the *xy* plane, and will be precessing coherently around the $B_0$ field, seen in step c) of Fig. 1.2. This coherence will be maintained as long as the field is homogeneous over the population of the source neutrons. The effects of inhomogeneities will be discussed in Section 2.4.2. The neutrons are allowed to precess freely for a duration $t_{\text{fp}}$, and are then subject to another $\pi/2$ pulse, step d). At this point, if the $\pi/2$ pulses were exactly on resonance with the neutron spin precession due to the $B_0$ field, and were applied for the proper duration, then the entire population will be put into the opposite spin state from the original, step e). This is because the two Ramsey pulses are in phase with each other, and at resonance, will also be in phase with the neutron spin. The final spin state is then measured along the $z$ axis. For an out of resonance pair of Ramsey pulses, the final spin state will be some superposition of the original and opposite spin state.

In order to precisely measure the resonant frequency, this experiment is done many times in succession, with the frequency of the $B_1$ field adjusted slightly for each data point. The result of these measurements is a pattern of fringes, called Ramsey Fringes. A theoretical representation of these fringes is shown in Fig. 1.3. These occur because there is a strong revival of the original spin state when the neutrons are exactly opposite in phase compared to the second Ramsey pulse at the end of the free precession period. The second pulse then flips the spin back to the original state, rather than driving it to the opposite state. There are also periodic dips when they are in phase at the end of the free precession period. If the Ramsey pulse frequency is slightly off-resonant, a $\pi/2$ pulse will actually shift the spin by less than $\pi/2$. The final state is then a superposition, with a small amplitude in the original spin state. These dips get more and more shallow as one moves off resonance. At the resonant frequency, one measures the strongest signal in spin in the opposite direction. This is the precession frequency of the neutrons in the electric and magnetic field.

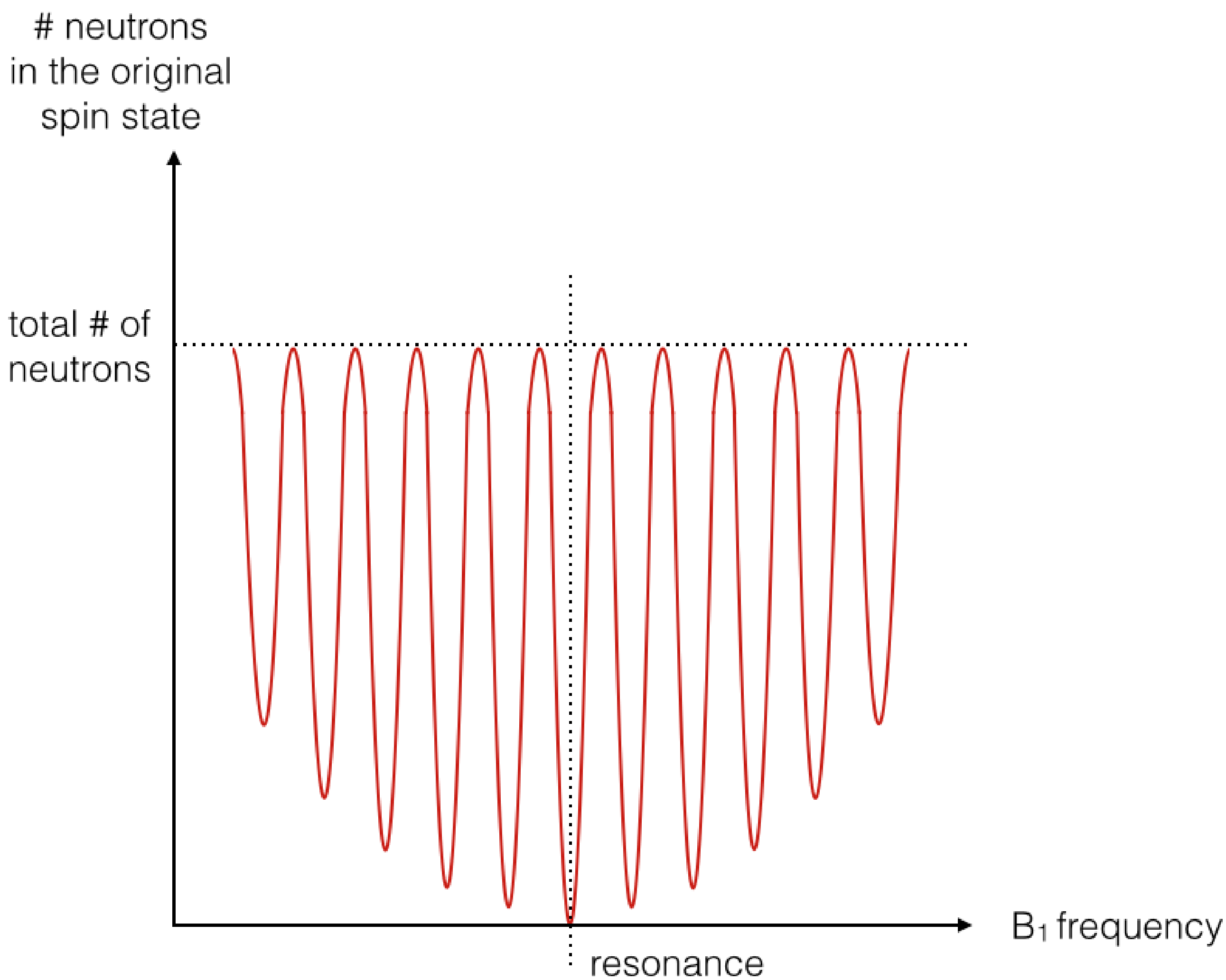


**Figure 1.3:** The Ramsey fringe pattern resulting from doing repeated measurements using Ramsey's method of separated oscillating fields, scanning the $B_1$ frequency across the resonance. In theory, the central dip will go to zero, and the full population of particles will always return to the original spin state if they are exactly out of phase at the end of the free precession time.

### 1.1.3 Rotating Wave Approximation

Since the spin vector of the neutrons is precessing around the $B_0$ field as this $\pi/2$ $B_1$ pulse is being applied, the $B_1$ field cannot simply be a constant field. In the ideal case it would be rotating in the *xy* plane, at the same frequency as the Larmor precession of the source atoms around the $B_0$ field. However, it is simple to show, using the rotating wave approximation, that a field oscillating along the *x* or *y* axis can also rotate the neutrons' spin vectors in the same way as a rotating field would, up to a shift in the effective field strength, called the Bloch-Siegert Shift.

Consider a $B_1$ field oscillating along the *x*-axis, which can be defined like so:

$$B_1 = B\cos(\omega t)\hat{\imath}. \tag{1.3}$$

This field is shown in Fig. 1.4, panel a). Mathematically, it can also be represented as two counter-rotating waves instead:

$$B_1 = \frac{B}{2}(\cos(\omega t)\hat{\imath} - \sin(\omega t)\hat{\jmath}) + \frac{B}{2}(\cos(\omega t)\hat{\imath} + \sin(\omega t)\hat{\jmath}), \tag{1.4}$$

shown in panel b). The total field experienced by the neutrons also includes the $B_0$ field, so the total field can be written as

$$B_{\text{total}} = \frac{B}{2}(\cos(\omega t)\hat{\imath} - \sin(\omega t)\hat{\jmath}) + \frac{B}{2}(\cos(\omega t)\hat{\imath} + \sin(\omega t)\hat{\jmath}) + B_0\hat{k}. \tag{1.5}$$

Now, convert this to a frame rotating at frequency $\omega'$ in the *xy* plane. In this frame, the frequencies of the counter-rotating $B_1$ fields are changed, increasing one and decreasing the other. There is also a correction that has to be made to the total field when considering the effect of the total field on the neutrons, $-\omega'/\gamma\,\hat{k}$. This correction comes from how the time derivative of the angular momentum behaves in the rotating frame, see [7] for the mathematical details.

$$B_{\text{rot}} = \frac{B}{2}(\cos((\omega-\omega')t)\hat{\imath} - \sin((\omega-\omega')t)\hat{\jmath}) + \frac{B}{2}(\cos((\omega+\omega')t)\hat{\imath} + \sin((\omega+\omega')t)\hat{\jmath}) + (B_0 - \omega'/\gamma)\hat{k}. \tag{1.6}$$

If the rotating frame is chosen to follow the precession of the neutrons, then $\omega = \omega'$. In this frame, one of the rotating $B_1$ fields is stationary, while the other rotates at $2\omega$. Also, $B_0 = \omega'/\gamma$, completely cancelling the field along the $\hat{k}$ direction. The total effective field experienced by the neutrons is

$$B_{\text{eff}} = \frac{B}{2}\hat{\imath} + \frac{B}{2}(\cos(2\omega t)\hat{\imath} + \sin(2\omega t)\hat{\jmath}). \tag{1.7}$$

These two fields are shown in the rotating frame, in Fig. 1.4, in panel c). In this rotating frame, the neutrons will precess around $B_{\text{eff}}$. This precession is much slower than $2\omega$, so the quickly rotating part of $B_{\text{eff}}$ has little effect. The precession around $B_{\text{eff}}$ is almost entirely from the static part of the field.

The rapidly rotating field does have a small contribution to the neutron precession, called a Bloch-Siegert Shift. This shift actually manifests itself as a change in precession frequency around the $B_0$ field in the lab frame. The correction is[8]

$$\omega_{\mathrm{BS}} = \frac{(\gamma B_1)^2}{2\omega}. \tag{1.8}$$

For the experiments performed in this thesis, this corresponds to a shift of less than one Hz, compared to the precession frequency of tens of kHz, and so, is completely neglected. In general, this term becomes less and less relevant as the magnitude of $B_1$ is reduced compared to $B_0$. A full derivation of this shift can be found in a 1955 paper by Ramsey[9], or for the even more general case of an elliptical $B_1$ field, in the original 1940 paper on the subject by Bloch and Siegert[10].

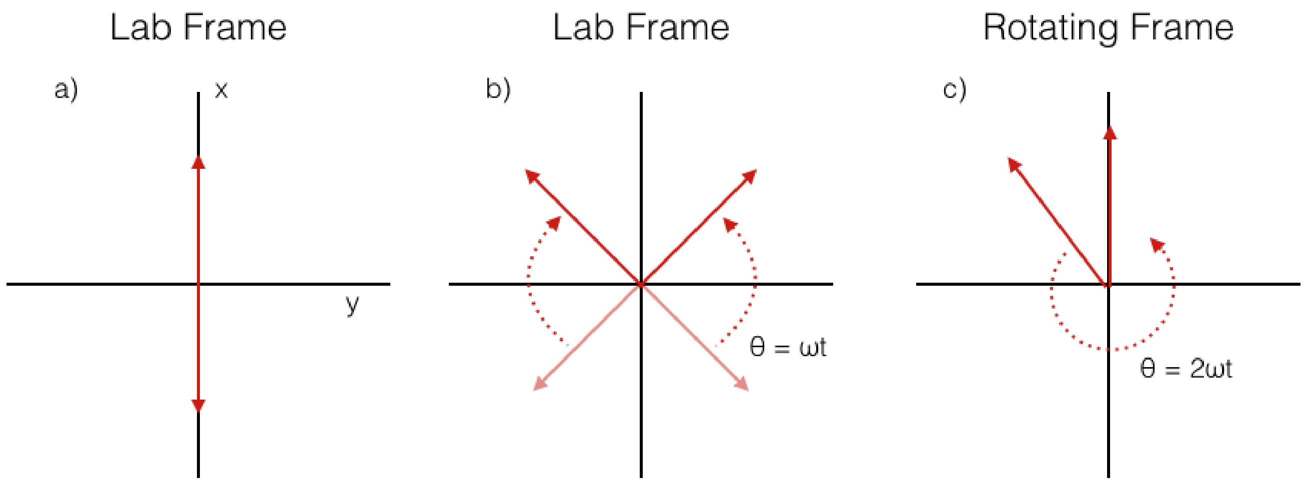


**Figure 1.4:** Shown is an oscillating field under the rotating wave approximation. The actual field in the lab frame is shown in a). It is decomposed into the clockwise and counter-clockwise parts in b). The two counter-rotating fields are shown in c), in a frame that rotates with one of the fields. That field is then stationary, while the other rotates at twice the frequency as it does in the lab frame.

### 1.1.4 Past Neutron EDM Experiments

Early neutron EDM experiments used fast-moving beams of neutrons, so the experiments had to be performed in very short time scales. The very first experiment was performed by J. H. Smith, E. M. Purcell and N. F. Ramsey, and used a beam of neutrons at a temperature of about 500 K. They found a neutron EDM of -0.1$\pm$2.4$\times$10$^{-20}$ $e$ cm[11]. At the time, a non-zero neutron EDM was not expected, since there was no reason to believe that time reversal invariance was violated in the universe. However, *CP* invariance was found to be violated in 1964, so making more precise measurements of the neutron EDM became very interesting[12].

There were a number of further experiments done using a hot beam of neutrons until techniques were discovered to cool neutrons further. Ultra-cold neutrons (UCNs) were used starting in the early 80s[13]. The first result from an experiment using UCNs was performed at the Leningrad Nuclear Physics Institute, obtaining a result of $|d_n| < 1.6 \times 10^{-24}$ $e$ cm[14]. The neutrons are cooled to about 6 m/s, cold enough to undergo total internal reflection with the chamber walls. The paper predicts that the neutron EDM measurement can be brought down to about $10^{-27}$ $e$ cm with this technique, by increasing the neutron storage time (the storage time in their experiment was about 5 s).

There is a limit to this time, however, because neutrons are known to have a mean lifetime of only 880.7±1.3±1.2 s[15].

The current upper limit on the neutron EDM is $|d_\mathrm{n}| < 2.9 \times 10^{-26}$, from a measurement performed at Institut Laue-Langevin (ILL)[6]. Modern neutron EDM experiments measure the exact magnetic field strength in the experiment by performing spectroscopy on a co-habitating atomic species, called a co-magnetometer.

### 1.1.5 Ultracold Neutrons

It was speculated, in the 40s and 50s, that neutrons which were cold enough, would undergo total internal reflection at any angle of incidence, off of certain types of surfaces, and so could be stored in bottles for their entire lifetime[16]. This speculation came from the scattering formula deduced and experimentally confirmed, by Enrico Fermi:

$$\sin(\theta) \leq \sqrt{V/E} \tag{1.9}$$

where $\theta$ is the angle of incidence at which the neutrons undergo total internal reflection, $E$ is the neutron's energy, and $V \approx 10^{-7}$ eV for many relevant materials, is now known as the material's "Fermi potential."[16] At energies below $V$, all angles $\theta$ satisfy the inequality. This also corresponds to the neutrons' de Broglie wavelengths becoming large compared to the inter-atomic spacing of the material of the walls.

The first neutron EDM experiment to use UCNs was performed in 1980, in the Leningrad Nuclear Physics Institute. There, a Beryllium converter, kept cold by flowing 20 K Helium through it, was used to cool the neutrons to about a velocity of 6.8 m/s. Despite a neutron flux density of about an order of magnitude lower than previous experiments done at ILL with a warm neutron beam, at LNPI they were able to significantly reduce the upper limit on the neutron EDM measurement, to $|d_\mathrm{n}| < 1.6 \times 10^{-24}$[14].

### 1.1.6 Co-Magnetometer

Noise and drifts in the magnetic field strength will be seen in the measurement of the neutron precession frequency, so to correct for these, it is necessary to carefully monitor the magnetic field during the EDM experiment. In early experiments, this was done by placing magnetometers around the experimental chamber. Precision was improved by introducing a magnetometer that co-habitates with the neutrons, a "co-magnetometer". This has generally been done using $^{199}$Hg, since it interacts little with neutrons and has a well known EDM and MDM. Such a co-magnetometer (with modifications that will be described in the next section, 1.1.7) will be used in the UCN EDM experiment.

The Ramsey method described in Section 1.1.2 will be used to measure the EDM of the neutron, but a similar method will also be used to precisely measure the magnetic field the neutrons occupy. The atoms in the co-magnometer will be polarized along the same axis as the neutrons, and a $\pi/2$ flip will also be applied to them. After this flip, the atoms are allowed to precess freely, and unlike for the neutrons, their precession frequency can be monitored constantly rather than only at the end of their free precession time, by optical detection, described in Section 1.2. By using atoms with a well-known EDM and MDM, the magnetic field strength can be calculated from the measured precession frequency of these atoms. This field measurement is then used to apply corrections to the neutron precession frequency that was measured.

### 1.1.7 Future Experiments

One major constraint on the precision of previous neutron EDM experiments comes from systematic effects from using $^{199}$Hg as a co-magnetometer, such as the $\vec{v} \times \vec{E}$ effect. This effect comes about when the $^{199}$Hg is moving in a strong electric field. In its own frame of reference, it also experiences an associated magnetic field. Under completely random motion, this effect should average out, but if there is even a slight overall rotation of the $^{199}$Hg, then the precession frequency will systematically be measured as too high or too low. Since the direction of the electric field changes during the experiment, the shift from the $\vec{v} \times \vec{E}$ effect changes as well. This looks *exactly* like the effect expected from a non-zero neutron EDM, so it is absolutely critical that this effect is well understood and reduced as much as possible in the experiment.

There is also inevitably a small gradient in the uniform magnetic field, and thus some field inhomogeneity. So, for the UCN experiment, any $^{199}$Hg nuclei that spend more time along the edges of the experimental cell will experience a different field, and different precession frequency than those that do not, introducing additional uncertainty in the field measurement.

Both of these effects can be mitigated by introducing a second type of atom to the magnetometer. This second atom would be affected differently by these systematic effects, since it would have a different gyromagnetic ratio, as well as a different average velocity at room temperature (and so, experience a different strength of $\vec{v} \times \vec{E}$ effect). This gives us additional data points that can be used to reduce uncertainty in the magnetic field measurement. The atom chosen needs to interact as weakly as possible with the neutrons themselves, however. $^{129}$Xe is an atom that fits all of these criteria.

## 1.2 Xenon

Xenon is a noble gas, atomic number 54 on the periodic table. One reason $^{129}$Xe is ideal as a co-magnetometer in neutron EDM experiments is that it interacts very little with neutrons. This means that a higher density of $^{129}$Xe can be used, which improves the signal to noise ratio (SNR) for the magnetic field strength measurement. Unfortunately, other aspects of the experiment still constrain the pressure of $^{129}$Xe that can be used. The major one being that at the strength of electric fields produced in the experimental chamber, too high of a pressure results in electrical breakdown.

### 1.2.1 Xe-129 Energy Levels

The precession frequency of the $^{129}$Xe is measured by driving a $\sigma^+$ transition with an ultraviolet (UV) laser. Two photons of 252.4 nm will drive the transition[17], and due to the two units of angular momentum added by the 2-photon absorption, the spin +1/2 ground state has no available excited state. The relevant transition, as well as the available decay channels after absorption are shown in Fig. 1.5. As a $^{129}$Xe atom precesses, it moves in and out of the this "dark" state, so the absorption rate varies sinusoidally. Since it is a two photon transition, this absorption rate is very small, so rather than trying to measure it directly, it is much easier to measure the resulting infrared (IR) fluorescence after absorption. Eventually, the $^{129}$Xe decays back down to the ground state.

A note on the energy level designations and terminology. The angular momenta of various parts of the atom (the nucleus, the electron cloud, the spin, etc.) are each designated by their own quantum number, listed and described in table 1.1. In this format of writing down the states, we are interested the F, I, and J quantum numbers. The

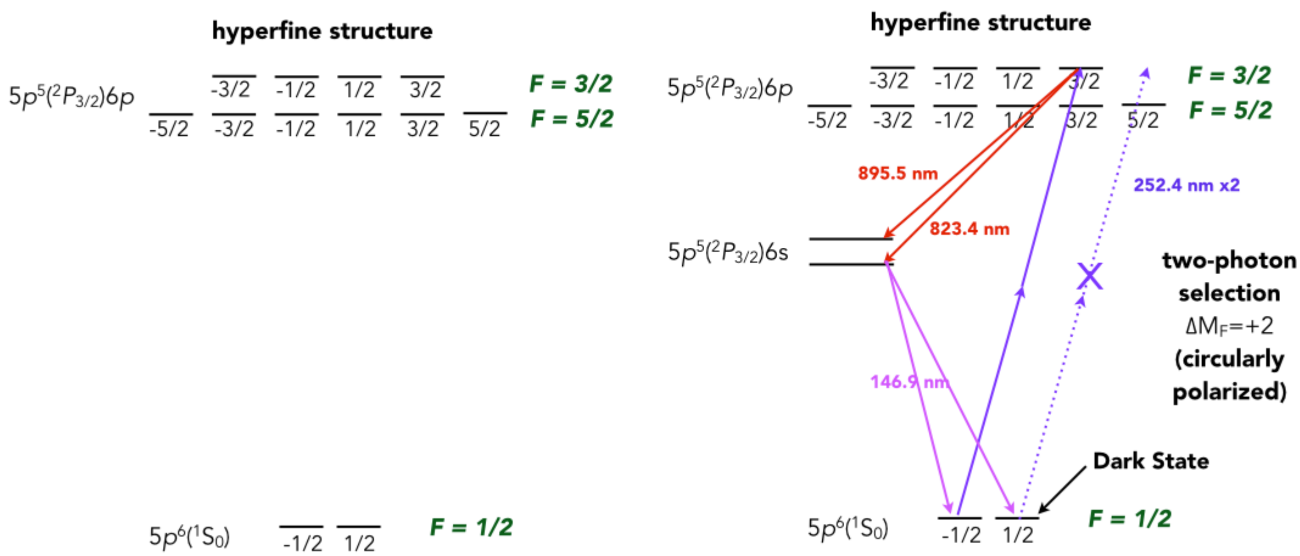


**Figure 1.5:** An energy level diagram of the relevant $^{129}$Xe transition. The diagram on the left is shown without absorption or decay channels for clarity. Light with wavelength of 252.4 nm drives the transition shown on the right, in a 2-photon process. When measuring the $^{129}$Xe precession frequency, $\sigma+$ polarized light is shined on the atoms. Under 2-photon absorption, this adds two units of angular momentum to the atom, meaning that the spin +1/2 ground state has no available excited state. This is called a "dark" state. As the atom's precession brings it in and out of this dark state, a sinusoidally varying absorption rate is observed.

| Letter | description |
|---|---|
| S | spin angular momentum |
| L | orbital angular momentum |
| J = L + S | total electron angular momentum |
| I | total nucleus angular momentum |
| F = I + J | total atomic angular momentum |

**Table 1.1:** The various angular momentum quantum numbers and what they represent.

ground state is designated as $5p^6(^1S_0)$. The term before the parentheses, $5p^6$, is the term that describes all of the "core" electrons, with all but the outermost layer of electrons truncated. For the ground state, this means that all of the orbitals, up to and including the 5p state, are filled. In this case, the total angular momentum of the electrons adds up to 0. Since the electrons must each occupy a different state by the Pauli exclusion principle, the spin and orbital angular momenta of electrons in a filled orbital must add up to 0, and in a ground state noble gas, there are no partially filled orbitals. Because the electrons have no total angular momentum, there is no hyperfine splitting for ground state $^{129}$Xe.

The nucleus for $^{129}$Xe has angular momentum I = 1/2, so for the ground state, F = 1/2 and $m_f = -1/2$ or $+1/2$. In the excited state, $5p^5(^2P_{3/2})6p$, one 5p electron has been excited to the 6p state. The core has one less electron (so, $5p^5$) and the excited electron is now considered a valence electron, and appears in the term at the end. In this case, the total electron angular momentum adds up to J = 2. The nucleus' angular momentum has not changed, so

I = 1/2 still. Combining J and I, F can take on the values F = 3/2 or 5/2, the antisymmetric and symmetric states, respectively. These F states are only split by about 2 GHz, due to hyperfine splitting. In general, pulsed lasers are too broad, spectrally, to resolve these states, which is unfortunate since they are better suited for detecting a 2-photon transition, having much higher peak intensities than continuous wave (CW) lasers. Table 1.2 shows the state equations for each of the F states and their projections, $m_f$. The coefficients for each state in the superpositions are found by using Clebsch-Gordan coefficients, which are used when adding up angular momenta in quantum mechanical systems.

Electrons at the same principle quantum number, *n* have their degeneracy lifted by various means. Due to the electron's spin and charge, it has an MDM. It is moving in an electric field generated by the nucleus and other electrons around it, and so, in its own frame, experiences a magnetic field. The energy of the electron is shifted by the interactions between its MDM and this magnetic field. This is known as spin-orbit coupling, and is responsible, in part, for fine splitting, the splitting of the energy of different orbital types within a principle energy level. Hyperfine splitting is due to a similar effect for the proton, where its magnetic dipole moment interacts with the magnetic field created by the moving electron. This effect is several orders of magnitude weaker, and is responsible for splitting the F states.

Energy levels of the individual $m_f$ states are also split via Zeeman splitting in a magnetic field. The shift in frequency for a given $m_f$ state is:

$$\Delta\nu = -\frac{\gamma m_f B_0}{2\pi} \tag{1.10}$$

This shift, and splitting between $m_f$ states, is very weak for the fields used in this experiment, however, and can be ignored. For the $m_f = 5/2$ state, $\Delta\nu = 4.22$ kHz, compared to the hyperfine splitting of the F states, about 2 GHz, and the line-width of the CW UV laser being developed, which is hundreds of MHz.

| F state | $m_f$ state | $m_j$ and $m_i$ states |
|---|---|---|
| F = $\frac{5}{2}$ | $m_f = \pm\frac{5}{2}$ | $\|\frac{5}{2},\pm\frac{5}{2}\rangle = \|\pm 2\rangle\|\pm\frac{1}{2}\rangle$ |
| | $m_f = \pm\frac{3}{2}$ | $\|\frac{5}{2},\pm\frac{3}{2}\rangle = \sqrt{\frac{1}{5}}\|\pm 2\rangle\|\mp\frac{1}{2}\rangle + \sqrt{\frac{4}{5}}\|\pm 1\rangle\|\pm\frac{1}{2}\rangle$ |
| | $m_f = \pm\frac{1}{2}$ | $\|\frac{5}{2},\pm\frac{1}{2}\rangle = \sqrt{\frac{2}{5}}\|\pm 1\rangle\|\mp\frac{1}{2}\rangle + \sqrt{\frac{3}{5}}\|0\rangle\|\pm\frac{1}{2}\rangle$ |
| F = $\frac{3}{2}$ | $m_f = \pm\frac{3}{2}$ | $\|\frac{3}{2},\pm\frac{3}{2}\rangle = \sqrt{\frac{4}{5}}\|\pm 2\rangle\|\mp\frac{1}{2}\rangle - \sqrt{\frac{1}{5}}\|\pm 1\rangle\|\pm\frac{1}{2}\rangle$ |
| | $m_f = \pm\frac{1}{2}$ | $\|\frac{3}{2},\pm\frac{1}{2}\rangle = \sqrt{\frac{3}{5}}\|\pm 1\rangle\|\mp\frac{1}{2}\rangle - \sqrt{\frac{2}{5}}\|0\rangle\|\pm\frac{1}{2}\rangle$ |

**Table 1.2:** Here are the state equations for all of the possible F and $m_f$ states of interest in $^{129}$Xe. The F = 5/2 states are all symmetric and F = 3/2 states are anti-symmetric. For each F and $m_f$ state, the possible combinations of $m_j$ and $m_i$ are shown.

## 1.3 UCN collaboration

The UCN collaboration's flagship experiment is to measure the neutron EDM at TRIUMF. One of the major improvements over previous neutron EDM experiments will be to reduce uncertainty due to systematic errors in the magnetic field strength measurement. This will be done by introducing $^{129}$Xe as a co-magnetometer in addition to the $^{199}$Hg used in previous experiments. The precession frequency is measured by driving a two-photon UV transition, where the $^{129}$Xe precesses in and out of a dark state.

### 1.3.1 High Power CW UV Laser

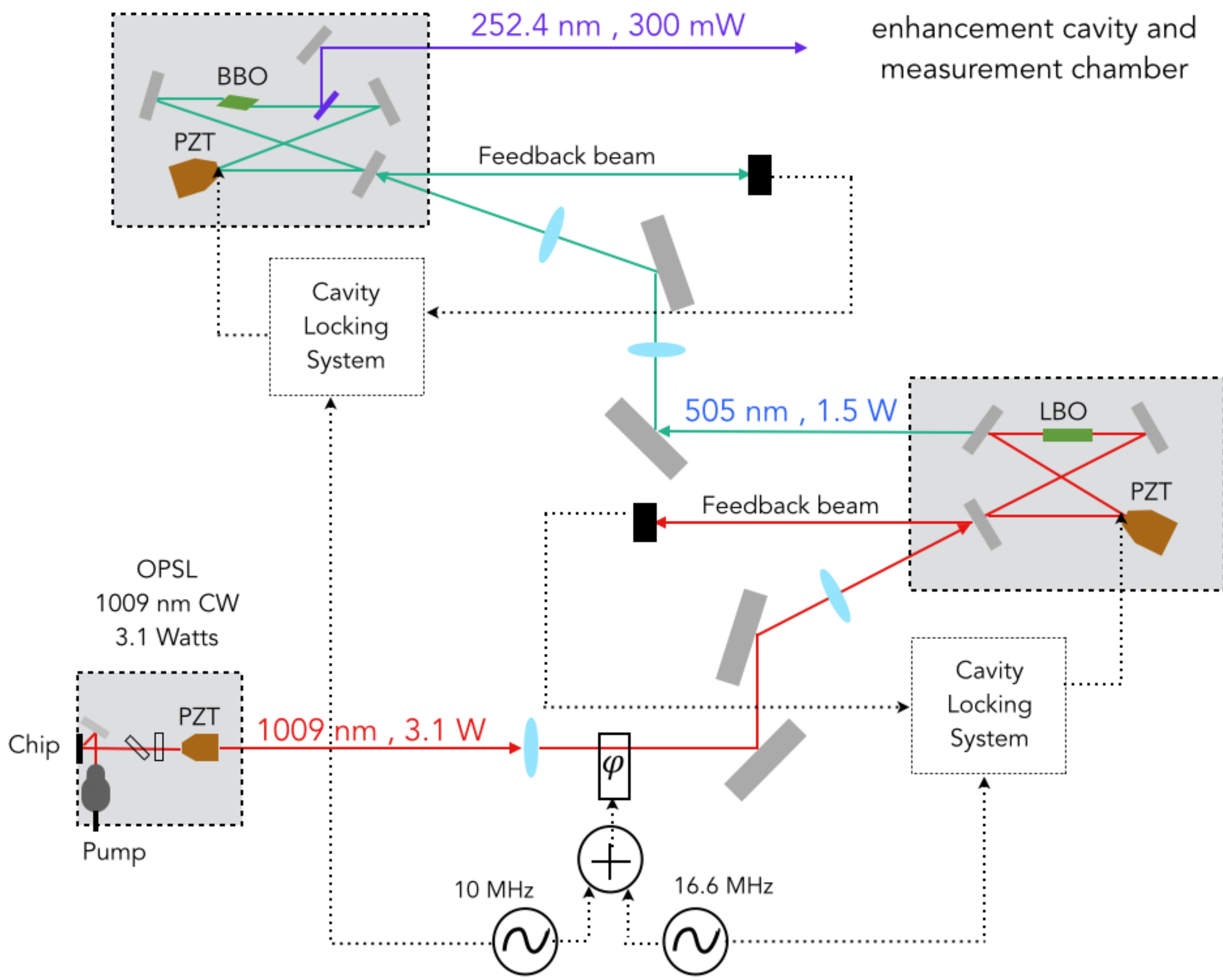


**Figure 1.6:** A schematic of the UV laser that will be used for $^{129}$Xe spectroscopy. This diagram shows work done by a fellow graduate student, Emily Altiere. The 1009 nm optically pumped semiconductor laser (OPSL) is frequency doubled twice in two optical cavities, using non-linear crystals. The total conversion efficiency is about 10%. Light from this laser will be sent to an enhancement cavity surrounding the $^{129}$Xe cell. This figure was modified and printed with permission from Emily Altiere. [1]

This laser is an IR OPSL that we generate the 4th harmonic from. Figure 1.6 is a schematic of the design. The laser itself operates at about 1009 nm, and has a free running line-width of about 100 MHz. Light from the laser is directed into an enhancement cavity, which has a lithium triborate (LBO) crystal in the optical path. This crystal converts a portion of the light into its second harmonic, which is green light at about 505 nm. The reason for using an enhancement cavity is that the conversion efficiency of the crystal depends on the intensity of the light going through it. Outside of the cavity, a single pass of 3W of IR would result in microwatts of green light. With the cavity, we are able to approach 50% conversion efficiency. The output from that cavity is then directed into another enhancement cavity, which generates the second harmonic of the green light, or fourth harmonic of the IR, at 252.4 nm. The type of crystal used in this cavity, barium borate (BBO), is quite sensitive to damage due, in part, to how easily it absorbs moisture from the air, so the cavity is sealed and dry air is flowed through it during operation.

One of the major challenges in developing this laser is mode matching the light into the cavities. Light coupling into the cavities must match the size and shape of the beam that can circulate in the cavity. A system of lenses is used to ensure this. Mode matching into the LBO cavity is relatively simple, since the beam is roughly circular already. It is far more challenging to mode match into the BBO cavity. The green light generated in the LBO cavity is not circular at all, and due to astigmatism from curved mirrors and from the crystal, the vertical and transverse modes of the BBO cavity require a slightly ovular input beam. Cylindrical lenses are used to shape each axis of the input light's profile properly.

The output we get from these enhancement cavities is about 300 mW of 252.4 nm UV light. This light is then collimated so that it is circular in profile and mode matched into the experimental cavity.

### 1.3.2 Testing the UV Laser

To test the UV laser's ability to drive this transition and detect the precession frequency of $^{129}$Xe in a magnetic field, I have built a set of magnetic coils that are used to perform NMR. Building and characterizing these coils, and using them to perform NMR on protons in water is the work that I will present in the rest of this thesis. The coils are set up to be like a simple version of the co-magnetometer that will be used in the actual neutron EDM measurement. There is a cell, containing only $^{129}$Xe, placed in the middle of a magnetic field, and after a $\pi/2$ pulse, the $^{129}$Xe nuclei will precess around that magnetic field. Detection can be done with a pickup coil, or with the UV laser, for comparison, and to make sure that there is a signal present when the laser is being tested. Figure 1.7 shows the laser and the test coils. In Chapter 2 I will go over some NMR theory, and in Chapter 3 I will discuss how to create the magnetic fields that are required for these experiments. The results of my work are shown in Chapter 4.

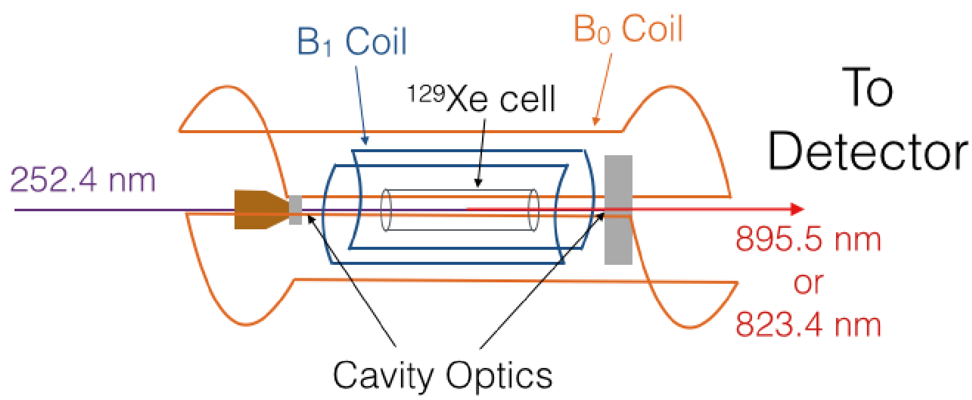


**Figure 1.7:** Here is a schematic of the test coils, the UV enhancement cavity, and the $^{129}$Xe cell. The actual measurement is the intensity of the IR light emitted as the $^{129}$Xe decays back down to the ground state, and we can choose to measure either the 895.5 nm or 823.4 nm emission. The back mirror of the UV enhancement cavity is transparent to IR, but the emission is in all directions, so the detector could be placed elsewhere if needed.

# Chapter 2

# NMR and Free Induction Decay

## 2.1 Introduction

Nuclear magnetic resonance (NMR) is a technique that many people are familiar with through magnetic resonance imaging (MRI), in which NMR is used to non-invasively image organs and other parts of the body. There are numerous other applications for NMR, such as determining the purity of a sample. This can be done by comparing the expected signal, given that the sample were 100% pure, to the actual NMR signal obtained, for example. For the ultra-cold neutron (UCN) neutron electric dipole moment (EDM) experiment, we are interested in using NMR to very precisely determine the strength of a magnetic field.

In general, NMR experiments take advantage of the fact that the spin vector of a nucleus precesses around a magnetic field, usually called $B_0$, if the spins are not aligned with that field. The angular frequency of this precession is given by the gyromagnetic ratio, $\gamma$, of the nucleus, which is simply the ratio of the frequency over the magnetic field strength. That is,

$$\omega_{\text{precession}} = \gamma B_0. \tag{2.1}$$

Precession is described in detail in Section 2.2.1

Conventionally, the $z$ axis is taken to be along the $B_0$ field, a convention I will keep in this thesis. The $x$ and $y$ axes are chosen such that they make a right handed coordinate system. The nuclei are initially polarized along the $B_0$ direction, either due to Boltzmann polarization, or by hyperpolarizing them by external means. These concepts will be described in Section 2.3. The nuclei's spins need to be rotated off of the $B_0$ axis in the experiment, which is usually done using a radio frequency (RF), field. Depending on the experiment, this field may only be on for a short duration, with the goal being a specific rotation of the spin. These are usually called $\pi/2$ or $\pi$ pulses, depending on the desired rotation. These pulses are described in Section 2.7, on free induction decay (FID). Other experiments may leave the RF field on for the entire measurement run.

There are two types of NMR that are of interest to us. The first is a technique called adiabatic fast passage (AFP). Using this technique, it is relatively easy to obtain a signal, making it a useful tool when trying to find evidence of hyperpolarization in a sample, as well as to quantify improvements of that hyperpolarization. The other technique is free induction decay (FID). This technique can be used to precisely determine strength and homogeneity of a magnetic field, and also most closely resembles the technique that will be used in the UCN neutron EDM experiment, making it the ideal method for testing the capability of our ultraviolet (UV) laser. Detection in an FID experiment is traditionally done with a pickup coil. This is the method that I use to determine what signal we should expect from the optical detection method that will be used later to test the UV laser. AFP and FID are described in Sections 2.6 and 2.7, respectively.

## 2.2 Particles in a Magnetic Field

### 2.2.1 Precession

Precession is a rotation of the angular momentum vector around some axis over time. A simple example is a spinning top in a gravitational field. If you start it spinning, and the spin axis isn't aligned perfectly with the direction of gravity, the top wobbles around this axis. A similar effect happens to magnetic dipoles with angular momentum in magnetic fields.

Consider a particle with spin angular momentum $\vec{S}$ in a magnetic field. It has a gyromagnetic ratio, $\gamma$, a dipole moment $\vec{\mu} = \gamma\vec{S}$, and experiences a torque, $\vec{\tau} = \vec{\mu} \times \vec{B}$. This torque is perpendicular to both the direction of the magnetic dipole (which is axis of angular momentum for a non-zero spin nucleus), and the magnetic field. The result is that the particle's spin vector $\vec{S}$ rotates around the magnetic field.

Torque is defined as the change in angular momentum over time, or

$$\vec{\tau} = \frac{\mathrm{d}\vec{S}}{\mathrm{d}t}. \tag{2.2}$$

But, as before, we also have

$$\vec{\mu} = \gamma\vec{S}, \tag{2.3}$$

which can be combined to get

$$\frac{\mathrm{d}\vec{S}}{\mathrm{d}t} = \gamma\big(\vec{S} \times \vec{B}\big). \tag{2.4}$$

If $\vec{B}$ is along the $z$ axis, as $\mathrm{B}_0$ is usually defined in NMR experiments, the form that the solution to equation 2.4 will take is

$$\vec{S}(t) = (\mathrm{S}_{xy}\cos(\gamma \mathrm{B}t + \phi), \mathrm{S}_{xy}\sin(\gamma \mathrm{B}t + \phi), \mathrm{S}_z). \tag{2.5}$$

The tip of $\vec{S}$ traces out a circle at height $\mathrm{S}_z$ on the Bloch Sphere, over time. Equation 2.1 is easily taken from 2.5; the precession frequency is $\omega = \gamma B$, or $f = \gamma B/2\pi$. The direction of the precession can be determined by the right hand rule (or by working out the cross product). It is important to note, however, that if $\gamma$ is negative, such as for $^{129}$Xe, the precession will be in the opposite direction. Figure 2.1 shows precession of the spin of a particle with positive $\gamma$ in a magnetic field pointing along the $z$ axis.

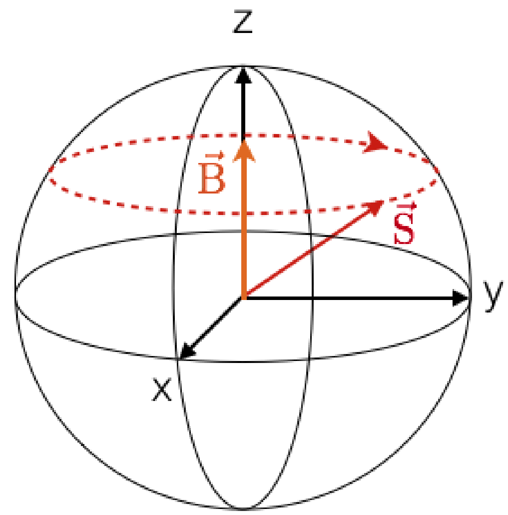


**Figure 2.1:** The spin vector of a particle precesses in a magnetic field, around the field axis. The right hand rule is useful to determine the precession direction, given by $\vec{S} \times \vec{B}$. It is important to note, however, that particles with negative gyromagnetic ratio, $\gamma$, will precess in the opposite direction. The figure shows precession for a particle with positive $\gamma$.

### 2.2.2 Projective Measurements of Spin Angular Momentum

Part of any NMR experiment is a measurement of the nuclei's spins along a particular axis. In some methods, this measurement results in a projection of the spin state onto that axis. In the case of a spin-1/2 particle, this projection then determines the probability of each possible state, +1/2 or -1/2, being measured.

I will follow the derivation in Sakurai's "Modern Quantum Mechanics" [18], with details changed to best fit my work. I will take the $x$ axis to be the axis that the spin is measured along, and the $z$ axis to be the axis the static magnetic field, $B_0$ is along. This is the axis the spins will be precessing around. The $y$ axis direction is such that the coordinate system is right handed.

First, take the case where a single particle's spin is precessing in the $xy$ plane at angular frequency $\omega$. In a magnetic field, with no electric field, the Hamiltonian of this system is

$$H = -\mu \cdot B. \tag{2.6}$$

The energy eigenstates of a spin 1/2 system are then

$$E_{\pm} = \mp \hbar \mu B. \tag{2.7}$$

The precession frequency is $\omega = \mu B$. When $H$ is time independent, like in the case of a static magnetic field, the time evolution operator is given by

$$\mathscr{U}(t, t_0) = \exp\left(\frac{-iH}{\hbar}\right), \tag{2.8}$$

and as long as this operator acts on an energy eigenstate, the Hamiltonian in the exponential can be replaced by the energy of the state being acted on. In this case, there are two eigenstates, spin up and spin down, with energies given by equation 2.7. Note that the energies of these states depend on B; in the absence of a magnetic field, the two spin states are degenerate.

Equations 2.6, 2.7, and 2.8 can be combined to rewrite the time evolution operator, in a static magnetic field, in terms of the frequency of precession:

$$\mathscr{U}(t,0) = \exp\left(\frac{-i\omega S_z t}{\hbar}\right) \tag{2.9}$$

In general, the initial state is superposition of spin up and spin down.

$$|\Psi, t=0\rangle = c_+|S_z+\rangle + c_-|S_z-\rangle. \tag{2.10}$$

If, at some point the particle is measured to be in the $|S_x+\rangle$ state, there is an equal chance of subsequently measuring spin up or spin down along the $z$ axis, so the initial state in that case is

$$|S_x+, t=0\rangle = \frac{1}{\sqrt{2}}|S_z+\rangle + \frac{1}{\sqrt{2}}|S_z-\rangle \tag{2.11}$$

Now, add the time dependence to see how this state evolves in time as the particle's spin precesses around the magnetic field along $z$.

$$|\Psi(t)\rangle = \frac{1}{\sqrt{2}}\exp\left(\frac{-i\omega t}{2}\right)|S_z+\rangle + \frac{1}{\sqrt{2}}\exp\left(\frac{i\omega t}{2}\right)|S_z-\rangle \tag{2.12}$$

The probability, then, to measure spin up along the $x$ axis, $S_x+$, over time is

$$P\big(|S_x+\rangle, t\big) = |\langle S_x+|\Psi(t)\rangle|^2 = \left|\Big[c_+\langle S_z+| + c_-\langle S_z-|\Big]\cdot\left[\frac{1}{\sqrt{2}}\exp\left(\frac{-i\omega t}{2}\right)|S_z+\rangle + \frac{1}{\sqrt{2}}\exp\left(\frac{i\omega t}{2}\right)|S_z-\rangle\right]\right|^2 \tag{2.13}$$

When multiplying this through, it is useful to remember the following properties:

$$\langle S_z+|S_z+\rangle = \langle S_z-|S_z-\rangle = 1 \tag{2.14}$$

$$\langle S_z+|S_z-\rangle = \langle S_z-|S_z+\rangle = 0 \tag{2.15}$$

The result is the following probability:

$$P\big(|S_x+\rangle, t\big) = \left|\frac{1}{2}\exp\left(\frac{-i\omega t}{2}\right) + \frac{1}{2}\exp\left(\frac{i\omega t}{2}\right)\right|^2 = \cos^2\left(\frac{\omega t}{2}\right) = \frac{1}{2} + \frac{1}{2}\cos(\omega t) \tag{2.16}$$

So, the probability of measuring positive spin along the $x$ axis from a particle that is precessing in the $xy$ plane over time is sinusoidal with frequency equal to the precession frequency. This result should not be surprising, as one can simply think of how the projection of the spin onto the $x$ axis changes as it precesses around the $z$ axis on the Bloch sphere.

It is also useful to look at a more general case. In actual experiments, there is always the possibility that the spin flip is not exactly the correct magnitude or duration. That is, the flip may cause the spin of the particle to over- or

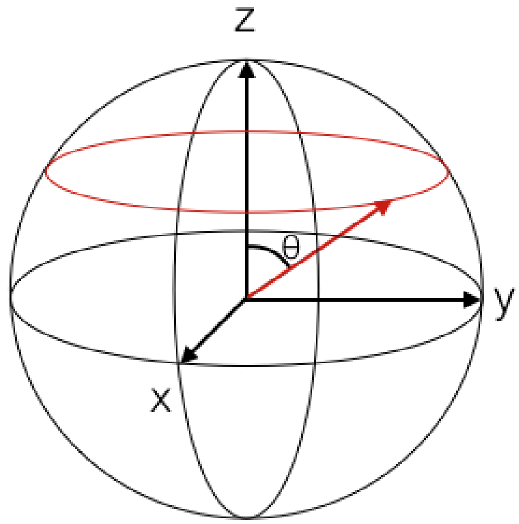


**Figure 2.2:** A particle with a spin state that is a superposition of spin up and spin down along $z$, with the amplitudes of each state given by the angle $\theta$. The arrow is only there to more easily define $\theta$. In a quantum mechanical spin system, the "coordinates" on the Bloch Sphere cannot all be known simultaneously, so the state is more accurately represented as a ring at some height.

undershoot the $xy$ plane on the Bloch Sphere. Furthermore, as will be discussed in Section 2.4.1, the particles' spins will relax toward thermal equilibrium in the magnetic field over time, which is a rotation of the spin vector toward the $z$ axis on the Bloch Sphere.

Take angle $\theta$ to be the polar angle in spherical coordinates (shown in Fig. 2.2), that is, 0° is up along the $z$ axis, 90° in the $xy$ plane and 180° down along the $z$ axis. The initial state is described quantum mechanically by choosing $c_+$ and $c_-$ appropriately. Using the Bloch Sphere makes this easy, by looking at the projection of the spin vector onto the $xy$ plane, $c_+ = \cos(\theta/2)$ and $c_- = \sin(\theta/2)$. Plug that into equations 2.10 and 2.13, to get:

$$P\big(|S_x+\rangle, t; \theta\big) = \left(\frac{1}{2} + \cos(\theta/2)\sin(\theta/2)\right)\cos^2\left(\frac{\omega t}{2}\right) + \left(\frac{1}{2} - \cos(\theta/2)\sin(\theta/2)\right)\sin^2\left(\frac{\omega t}{2}\right) \tag{2.17}$$

This is the probability of measuring spin + in x for a particle whose initial $z$ spin state is arbitrary, defined by $\theta$, and then precesses in a magnetic field along the $z$ axis. Notice, the probability becomes 50% when $\theta = 0°$ or $180°$, as expected, and equation 2.16 is recovered when $\theta = 90°$. Measuring the spin along the $y$ axis instead simply corresponds to a phase shift in the probability to measure spin up or spin down.

## 2.3 Spin Polarization

### 2.3.1 Boltzmann Polarization

A sample that is polarized according to thermal equilibrium is said to be "Boltzmann polarized." In the absence of an electric or magnetic field, the spin states in a given orbital have the same energy (although it turns out that even the electric and magnetic fields from the proton(s) in the nucleus are enough to measurably break this degeneracy). A magnetic field will break the degeneracy between spin states along the direction of the field. Since there is a difference in energy, atoms will not necessarily occupy those states in the same proportion. Instead, the distribution of states in the sample will depend on its temperature and the energy difference between states. In a spin 1/2 system this results in an imbalance between the two spin states. That is, the system will polarize to some degree.

Take a proton in a magnetic field, $B$, for example. This is a spin 1/2 particle, so there are two spin states, which are not degenerate in this field. The energy difference between the two states is $\Delta E = 2\mu_p B$. When the system is in thermal equilibrium, the protons will follow the Boltzmann distribution:

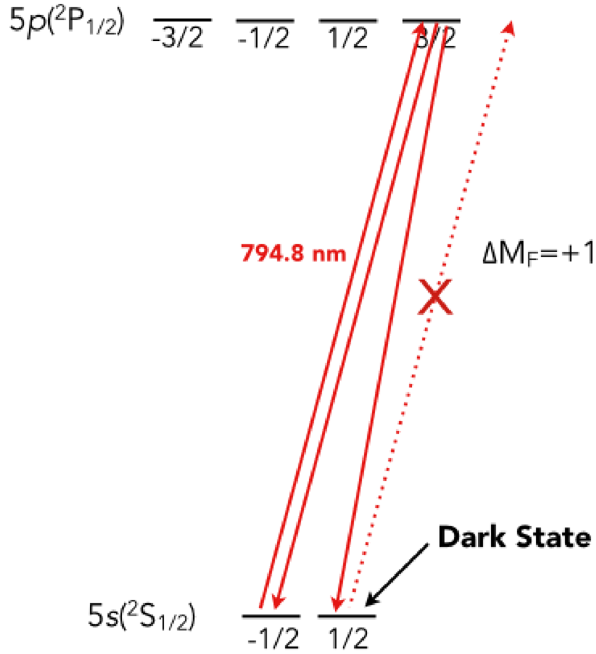


**Figure 2.3:** These are the energy levels of interest for optically pumping Rubidium. Initially, the ground spin states are populated according to the Boltzmann distribution. Atoms in the dark state cannot absorb the circularly polarized 795 nm light [19], and stay in that spin state. Atoms in the bright state will absorb a photon and eventually decay randomly back to either the bright or dark ground state. Any atom that decays into the dark state (the +1/2 state) will stay there, so over time the dark state becomes more populated and the sample becomes hyperpolarized.

$$f(E) = 1 - \frac{1}{A\exp\left(\frac{E}{kT}\right)} \tag{2.18}$$

where $f$ is the probability of a given particle being in the state with energy $E$, $k$ is the Boltzmann constant, $T$ the temperature, and $A$ is a normalization constant. The degree of polarization, $N_+/N_-$, can be determined from the difference in probabilities for each state:

$$\frac{N_+}{N_-} = \exp\left(-\frac{\Delta E}{kT}\right). \tag{2.19}$$

For a room temperature sample of protons, this corresponds to a polarization of about 4.4 parts per million (PPM)[20].

If such a sample is subject to a $\pi/2$ pulse, this polarization remains, and there will be a measurable signal from the spin precession, unlike in the case of a completely unpolarized sample. Even though the polarization is small, a Boltzmann polarized sample of liquid water can be used to generate a measurable NMR signal from protons (by applying the proper fields to the hydrogen atoms in the water molecules).

### 2.3.2 Hyperpolarization

A sample that has been polarized beyond its Boltzmann polarization is said to be "hyperpolarized." A hyperpolarized sample can generate much larger signals than a Boltzmann polarized sample, or generate a signal of similar strength with far fewer particles. This makes it possible to perform NMR on a thin gas. There are several ways to achieve hyperpolarization, but a commonly used one is optical pumping.

To perform optical pumping, circularly polarized light is shined on the atoms, such that for a given spin state, there is no available excited state due to the angular momentum that would be added by absorbing that photo. Atoms in the other spin state, the "bright" state, are able to absorb a photon, however. After absorption, the excited atoms will eventually decay back to the ground state, and end up in a random spin state again. Those that end up back in the bright state will absorb another photon, but those in the dark state will remain there. Over time, the dark state gets filled up, and the entire population is transferred to that state.

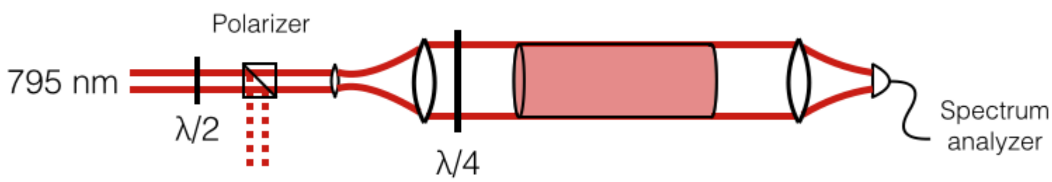


**Figure 2.4:** A schematic for doing optical pumping of Rubidium. The half wave plate and polarizer are used to ensure that the light is polarized (light reflected from the polarizer is dumped or can be used as a way to measure the power of the laser if the degree of polarization from the laser is known and does not change over time). A quarter wave plate then circularly polarizes the light. A pair of lenses acts as a telescope to blow up the beam to about the size of the Rubidium cell and collimate it. After the cell, light is focused onto a spectrum analyzer. In general, some method of attenuating the light is necessary to avoid damaging the analyzer, which is not shown in this diagram. Methods include reflecting the light off of a piece of glass, or using a neutral density filter. Figure 2.5 shows the change in signal expected when shining linearly polarized light versus circularly polarized light into the cell.

Rubidium is often hyperpolarized using this technique. Light from a 795 nm laser [19] is circularly polarized using a quarter wave plate. The relevant states are shown in Fig. 2.3. This beam is expanded to fill the entirety of the cell containing Rb. With the circularly polarized light, the cell quickly becomes transparent as the dark state is filled. If the quarter wave plate is rotated so that it passes the linearly polarized light through, unchanged, the cell is no longer transparent to the light. By focusing the light onto a spectrum analyzer, it is possible to check for this

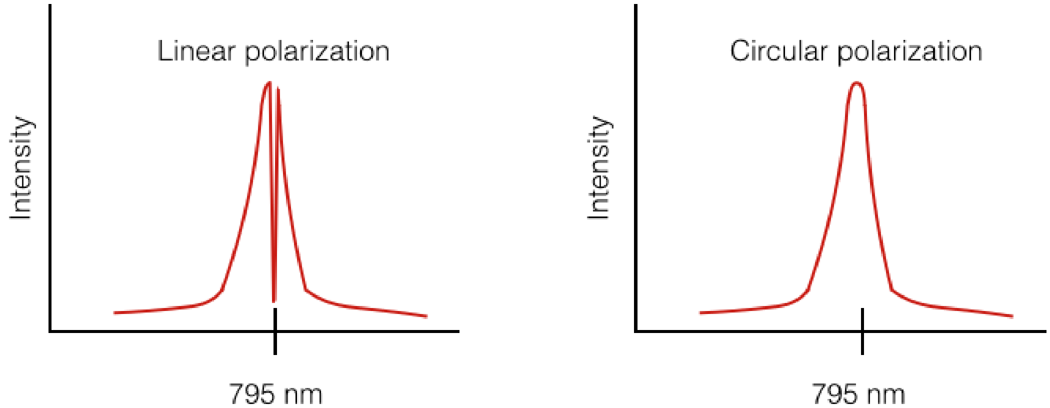


**Figure 2.5:** Shown are the expected signals from a spectrally broad laser being shined on a Rubidium cell under linear polarization (left plot), and circular polarization (right plot), after sufficient time for optical pumping to occur. When shining linearly polarized light, such as the schematic shown in Fig. 2.4 with the quarter wave plate removed or set such that it does not alter the linear polarization, the Rubidium is able to absorb all of the light within the transition's bandwidth. However, when the light is circularly polarized, one of the spin states in the ground state does not have a corresponding excited state with the correct angular momentum to transition to. Atoms in this "dark state" do not absorb photons. After several decay periods, all of the atoms are driven into this dark state as they absorb a photon and then decay randomly back into the bright state (where they can absorb another photon) or the dark state (where they remain and are transparent to the light). Once all of the atoms are in the dark state, the entire cell is transparent and the dip in the spectrum disappears.

change in absorption. Figure 2.4 shows a typical optical pumping setup, and Fig. 2.5 shows the difference in the spectrum between sending linearly polarized light vs. circularly polarized light through the Rubidium cell.

To polarize the $^{129}$Xe in our experiments, we use a process called spin exchange to transfer spin polarization from a sample of optically pumped Rubidium to the $^{129}$Xe through van der Waals interactions. Nitrogen is used as a mediator in these interactions. This technique overall is called spin exchange optical pumping (SEOP) [21]. The setup involves flowing the $^{129}$Xe mixture through the Rubidium cell, and directly from there to the experimental chamber.

## 2.4 Spin Relaxation

A sample that is in a static magnetic field aligned along the $z$ axis, but polarized along some axis in the $xy$ plane will lose that polarization over time. There are several of these relaxation mechanisms, and they are generally described by their time scales, called $T_1$, $T_2$, and $T_2^*$.

### 2.4.1 $T_1$

The $T_1$ lifetime is defined by how quickly the magnetization of the atoms in the direction of the $B_0$ field reaches thermodynamic equilibrium, or Boltzmann polarization. This necessarily results in a de-magnetization of the atoms in the $xy$ plane. This effect is shown in Fig. 2.6. If the sample is initially polarized along $x$ or $y$, the magnetization along the $z$ axis over time is

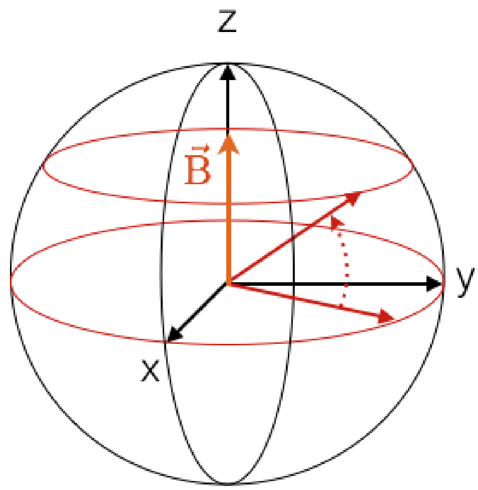


**Figure 2.6:** Shown is the effect of $T_1$ relaxation. The spin moves toward thermodynamic equlibrium along the $z$ axis (specifically, along the direction of $B_0$). This causes the projection in the $xy$ plane to decrease in amplitude, and a loss of signal strength in NMR experiments.

$$M_z(t) = M_{z,eq}(1 - \mathrm{e}^{-t/T_1}). \tag{2.20}$$

In this case, the $T_1$ time is the time it takes for the sample to recover $1 - 1/e$ or about 63% of its magnetization at thermal equilibrium.

Historically, this is also known as the spin-lattice relaxation time, since this relaxation depends on interactions with the sample's surroundings. This time becomes very short when the rotation rate of the molecules or atoms is similar to that of the Larmor precession frequency. In general, stronger magnetic fields are associated with longer $T_1$ times, since the rotation rate is generally smaller than the precession frequency, even with the $B_0$ field at around a tenth of a mT in strength. Stronger magnetic fields bring the precession frequency even further from this resonance.

### 2.4.2 $T_2$ and $T_2^*$

The $T_2$ lifetimes are determined by local field inhomogeneities, which cause atoms to precess at different frequencies, resulting in dephasing over time. This effect is split into two types, the $T_2$ lifetime, caused by time-varying inhomogeneities, and $T_2^*$, caused by inhomogeneities that are constant or slowly varying over the lifetime of the experiment. It is not strictly correct to call $T_2^*$ a "relaxation" process, since it is not random, and in fact, as will be described in this section, the dephasing caused by these effects can be reversed, and a signal can be recovered in a spin echo experiment.

The $T_2$ lifetime describes how the component of the magnetization perpendicular to $B_0$ relaxes:

$$M_\perp(t) = M_\perp(0)\exp\left(\frac{-t}{T_2} - \gamma\Delta B_0\right), \tag{2.21}$$

Where $\Delta B_0$ is the difference between the maximum and minimum field strength in the region of interest. This is also called spin-spin relaxation, since one possible source of a rapidly time-varying inhomogeneity occurs when two atoms move past each other. The field one atom generates can perturb the total field, and the precession frequency, of the other. Whenever two atoms interact in this way, they are dephased from the rest of the sample. The $T_2$ lifetime also includes other rapidly varying inhomogeneities such as atoms moving across spatially small regions of constant inhomogeneity, or random fluctuations in the field to current noise, and so on. Any process that causes atoms to experience a non-uniform field that changes on the time scale of the experiment is included in the $T_2$ lifetime.

The $T_2^*$ lifetime is caused by a gradient in the $B_0$ field. Two atoms that are spatially separated experience a different, but constant in time, magnetic field, so they have different precession frequencies. The $T_2^*$ lifetime is defined as

$$\frac{1}{T_2^*} = \frac{1}{T_2} + \gamma \Delta B_0. \tag{2.22}$$

Because this inhomogeneity is invariant in time, it does not cause a random dephasing process and it is theoretically possible to recover a signal from a sample that has dephased this way. Note that in general as you increase the strength of $B_0$, its gradient will also increase, making the $T_2^*$ time faster. In fact, it is the number of periods of precession it takes for the sample to dephase that will stay constant (ignoring non-linear effects), rather than the time.

### 2.4.3 Spin Echo

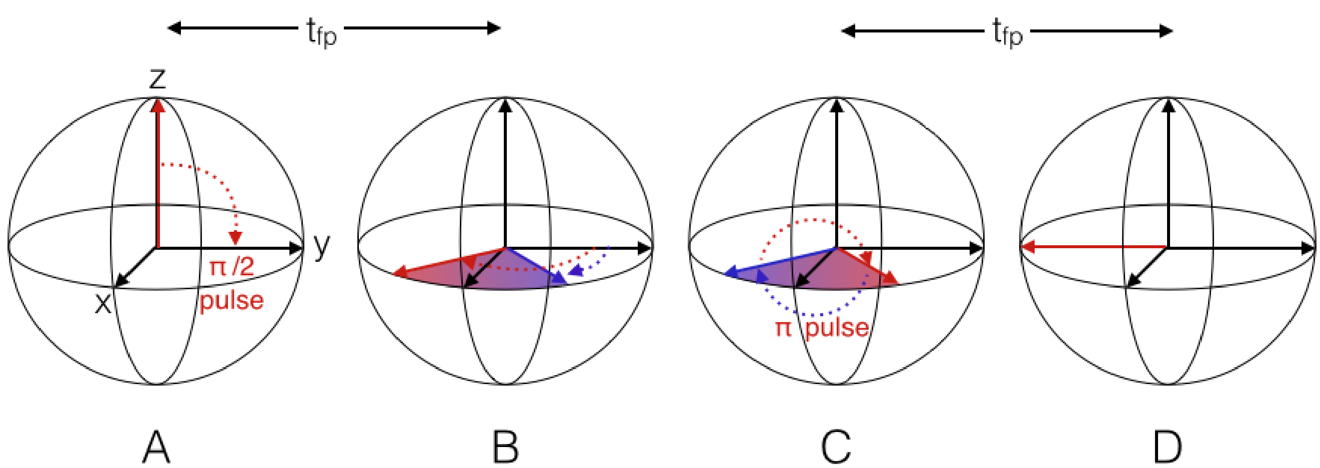


**Figure 2.7:** A spin echo experiment. The atoms begin with spin aligned with the $B_0$ field. A) They are given a $\pi/2$ pulse. B) They precess freely in the static field. Atoms in a stronger part of the field precess faster, colored red here. Those in a weaker field precess more slowly, colored blue. Since the field strength varies smoothly, there will be a distribution of phases, shown as a gradient here. C) After some time, a $\pi$ pulse flips the spins around the $x$ axis. The more slowly precessing atoms are now ahead in phase compared to the more rapidly precessing atoms. D) After a time equal to the time between pulses, the atoms are all in phase again.

$T_2^*$ and $T_2$ can be determined by performing a spin echo experiment. In such an experiment, a sample that is polarized along the $B_0$ direction is first subject to a $\pi/2$ pulse. The spins precess around the $B_0$ field, but due to

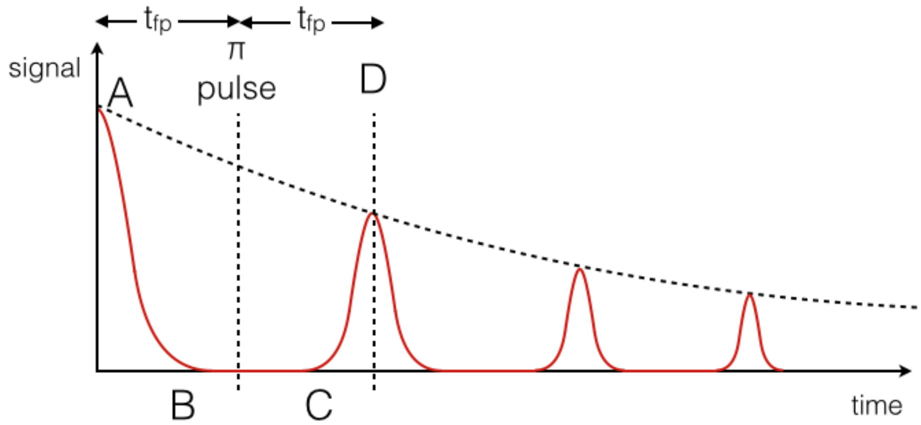


**Figure 2.8:** Here is what a demodulated signal from a spin echo experiment should look like. Multiple echoes are shown, but only the first is annotated. The numbers correspond to the stages of the spin flip experiment described in Fig. 2.7. The signal is recovered after each $\pi$ pulse, but is weaker each time. The peak envelope can be fit exponentially, with a decay constant due to the $T_1$ and $T_2$ times. $T_2^*$ is given by how quickly the signal is lost after each peak.

the field's gradient, the individual nuclei precess at slightly different frequencies. This results in dephasing and eventually the signal is lost. This decay in signal will be exponential, with $T_2^*$ as the time constant. A $\pi$ pulse then rotates all of the spins about some axis in the *xy* plane. This effectively swaps the phases of all of the atoms. The slower precessing atoms are now ahead in phase compared to the faster precessing atoms, and vice versa. After an amount of time equal to the time between the $\pi/2$ and $\pi$ pulses, the atoms are briefly back in phase, and a signal is seen again. This is called a spin echo. The echo is always weaker than the initial signal because the polarization (and thus, magnetization) is never completely recovered. All of the factors that contribute to weakening the echo, such as noise in the field, nuclei interacting with each other, and so on, determine the $T_2$ lifetime.

This experiment can be repeated, changing the delay between pulses, and by tracing the envelope of peak heights, one should see an exponential decay. The time constant of this decay is $T_2$. A spin echo experiment is detailed and diagrammed in Figs. 2.7 and 2.8.

## 2.5 Detection

### 2.5.1 Detection Via Pickup Coil

A common method for measuring the precession frequency is to measure the electromotive force (EMF) induced by Faraday induction from the changing magnetic field generated by the spin of the particles. Faraday induction on a single loop of wire is given by:

$$\varepsilon = -\frac{\mathrm{d}\phi}{\mathrm{d}t} \tag{2.23}$$

where $\varepsilon$ is the EMF and $\phi = BA$ is the magnetic flux through the coil; the field strength times the area enclosed by the loop. For N loops, the signal is simply multiplied by N, so

$$\varepsilon_{tot} = -N\frac{d\phi}{dt} \tag{2.24}$$

The negative sign is due to Lenz's law. The EMF generated drives a current that creates a magnetic field which opposes the change in the field due to the precession of the nucleus.

In a stronger magnetic field, the nucleus precesses more rapidly, which means that the magnetic field generated by the its spin changes more rapidly, and generates a larger EMF in the pickup coils. However, as discussed in Section 2.4 and Chapter 3, a stronger field also results in a signal that decays more rapidly, unless the $B_0$ field is made more homogeneous.

The signal detected in the pickup coil will be sinusoidal, as $d\phi/dt$ will change based on the angle made between the pickup coil axis and the polarization axis. The frequency of the signal will be exactly the precession frequency of the nuclei, and since that should be well known, one can use a lock-in amplifier to amplify the signal and filter out noise at other frequencies.

### 2.5.2 Optical Detection

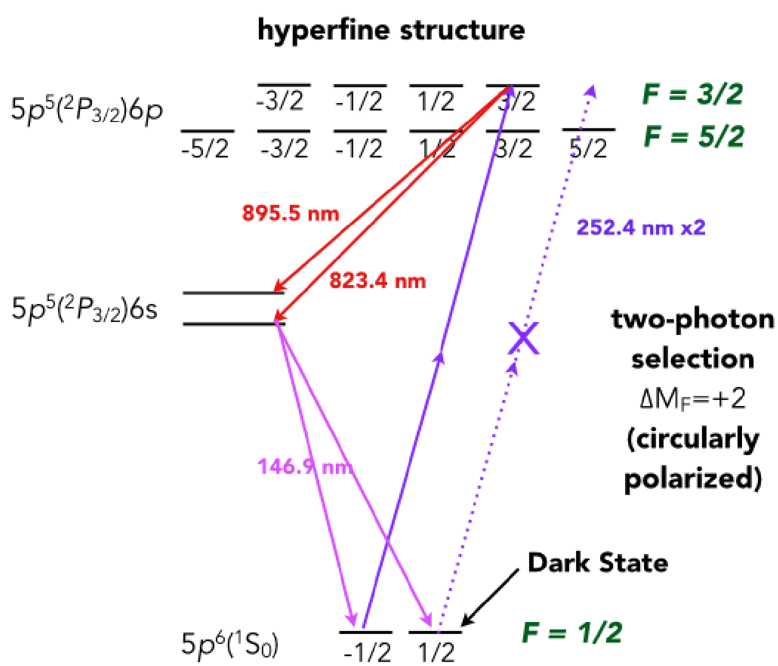


**Figure 2.9:** $^{129}$Xe has a dark state when driving the 252.4 nm two photon transition from the ground state using circularly polarized light. When using $\sigma+$ light, the +1/2 state cannot absorb the UV light, since there is no excited state with the proper amount of angular momentum. The atoms in this state are transparent to this light.

Detection in the UCN experiment will be done optically, instead of using a pickup coil. Circularly polarized light will be shined on the $^{129}$Xe. For one spin state in the $^{129}$Xe ground state there is no excited state available due to the additional angular momentum from the absorbed light, creating what is called a dark state, shown in Fig. 2.9. Atoms in the dark state will not absorb this light, so the absorption is dependent on the spin state of the $^{129}$Xe. As the atom precesses, the probability of absorption varies sinusoidally, at the precession frequency of the $^{129}$Xe.

This type of measurement results in a projection of the atom's spin along the axis of absorption, so the behaviour of the signal should look like it is described in Section 2.2.2. An atom that absorbs a photon also ends up dephased, since the decay back to the ground state is completely independent of the phase of precession in the atoms around it. This can be an issue when there is a high rate of absorption, but in the case of $^{129}$Xe, we are driving a two photon transition, so the absorption rate is very low, and dephasing from this is negligible.

The amplitude of the signal from this method depends entirely on the absorption rate of the UV light, and is independent of the rate of precession. This is useful for the UCN EDM measurement, since the magnetic field will be made as weak as possible. Unfortunately this absorption rate is very low, so it is much easier to detect the infrared (IR) emission as the $^{129}$Xe decays back to the ground state rather than try to detect the actual absorption. The relevant $^{129}$Xe energy levels, and wavelengths of the light used and measured are shown in Fig. 2.9. There are two IR decay channels from the excited state, and we will decide on which one to measure based on calculations of the branching ratio between the two channels.

## 2.6 Adiabatic Fast Passage (AFP)

### 2.6.1 Overview

In an AFP [1] experiment, nuclei are first polarized along the $B_0$ field direction. This field is also called the static field, although it is actually ramped slowly. The RF field, $B_1$, is left on for the duration of the experiment. For most of the $B_0$ ramp, the $B_1$ field is out of resonance with the nuclei's spin precession. In this case, it has little effect on the spin of the nuclei. However, as the ramp scans through the field strength at which the $B_1$ field is resonant with the nuclear spin precession, this spin gets flipped. The $B_0$ field then ramps back out of resonance and the spin axis remains stationary again until the next ramp.

To understand how the spin flip works in detail, it is useful to look at a rotating reference frame, that rotates at the $B_1$ frequency. Figure 2.10 shows the spin flip process. In this rotating frame, the nuclei and fields behave somewhat differently. $B_1$ is a static field, and the precession frequency of the nuclei around $B_0$ is $\omega' = \omega - \omega_{B_1}$. This also means that the $B_0$ field strength is effectively reduced, so $B_0' = B_0 - \omega/\gamma$.

Starting at the peak of a ramp of $B_0$, the nuclei are precessing slightly faster than the $B_1$ frequency. That is, in this rotating frame, $\omega'$ is small and positive. The strength of $B_0'$ is then also small and positive, and the total effective field felt by the nuclei is $B_{\text{eff}} = B_0' + B_1$. At the peak of a ramp, $B_{\text{eff}}$ is dominated by $B_0'$, and the field points mostly along the $z$ axis, which is the axis of the $B_0$ field and of the nuclei's initial polarization. As the $B_0$ field ramps down, however, $B_0'$ approaches 0, and $B_{\text{eff}}$ tilts towards the $xy$ plane, as can be seen in the first two plots in Fig. 2.10. If the ramp is slow enough to be adiabatic, the spin of the nuclei will follow $B_{\text{eff}}$ as it tilts.

The ramp down continues, and $B_0'$ becomes negative, so $B_{\text{eff}}$ tilts below the $xy$ plane, until $B_0'$ once again dominates over $B_1$, this time in the negative direction. The polarization has been transferred to the spin down state. This process is shown in the last plot in Fig. 2.10. This figure also shows how the spin vector rotates on the Bloch sphere during the spin flip.

[1] The name "adiabatic *fast* passage" may sound odd, but it is called fast to differentiate it from adiabatic slow passage, where the ramp is slow compared to the relaxation times. A detailed description is found in Bloch's 1946 paper on nuclear induction[22].

Due to this new polarization direction, the nuclei are not in thermal equilibrium anymore, however, so over time, determined by the $T_1$ lifetime, they will relax back to a thermal polarization. The $B_0$ ramp needs to be quick enough that this relaxation takes a long time compared to the spin flip.

### 2.6.2 Speed of the $B_0$ ramp

There are some constraints on how quickly or slowly $B_0$ can be ramped in a successful AFP experiment. For obvious reasons, the $B_0$ field must ramp through the spin flip faster than the time constant for any relaxation process (relaxation effects are discussed in a previous section, 2.4). That is,

$$\frac{B_1}{T_1}, \frac{B_1}{T_2^*} << \frac{dB_0}{dt}. \tag{2.25}$$

$B_0$ must also ramp slowly enough, though, for the spin to follow adiabatically. The spins of the nuclei will "lock" to the local direction of the magnetic field as long as that field does not change too rapidly. The condition for adiabaticity in this case is[23]:

$$\frac{dB_0}{dt} << \gamma B_1^2. \tag{2.26}$$

In general, these constraints on the ramp speed are actually rather forgiving, since the relaxation times and the adiabatic condition tend to be quite far apart.

### 2.6.3 Detection and Signal

Detection is usually done via pickup coil, which is the method we use in our setup for AFP. The signal is a voltage, generated by Faraday induction from the precessing spins, in the pickup coil. Since the $B_0$ field is ramped repeatedly, a signal is produced every time the precession frequency scans through the $B_1$ frequency. For hyperpolarized samples, the signal decays over time as the sample returns to the Boltzmann polarization, but for Boltzmann polarized samples, this repetition is seen indefinitely with no loss. This is a tremendous advantage, since such samples can be used to average a signal over many ramps, to greatly improve signal to noise ratio (SNR). This is invaluable especially when working with a newly constructed setup, where the noise characteristics are not yet well known. A well tuned and noise controlled AFP experiment should produce an easily recognizable signal without averaging, however.

The signal itself is a sin wave, which increases in amplitude as the ramp approaches resonance. Each ramp up or down produces a peak in the envelope of the wave. The height of this peak, as well as the phase of the sin wave itself within this envelope, depends on how quickly the ramp is repeated compared to the $T_1$ lifetime. Because of this, it is possible to use AFP to measure the $T_1$ time of the sample used, by varying how quickly the ramp through resonance is repeated.

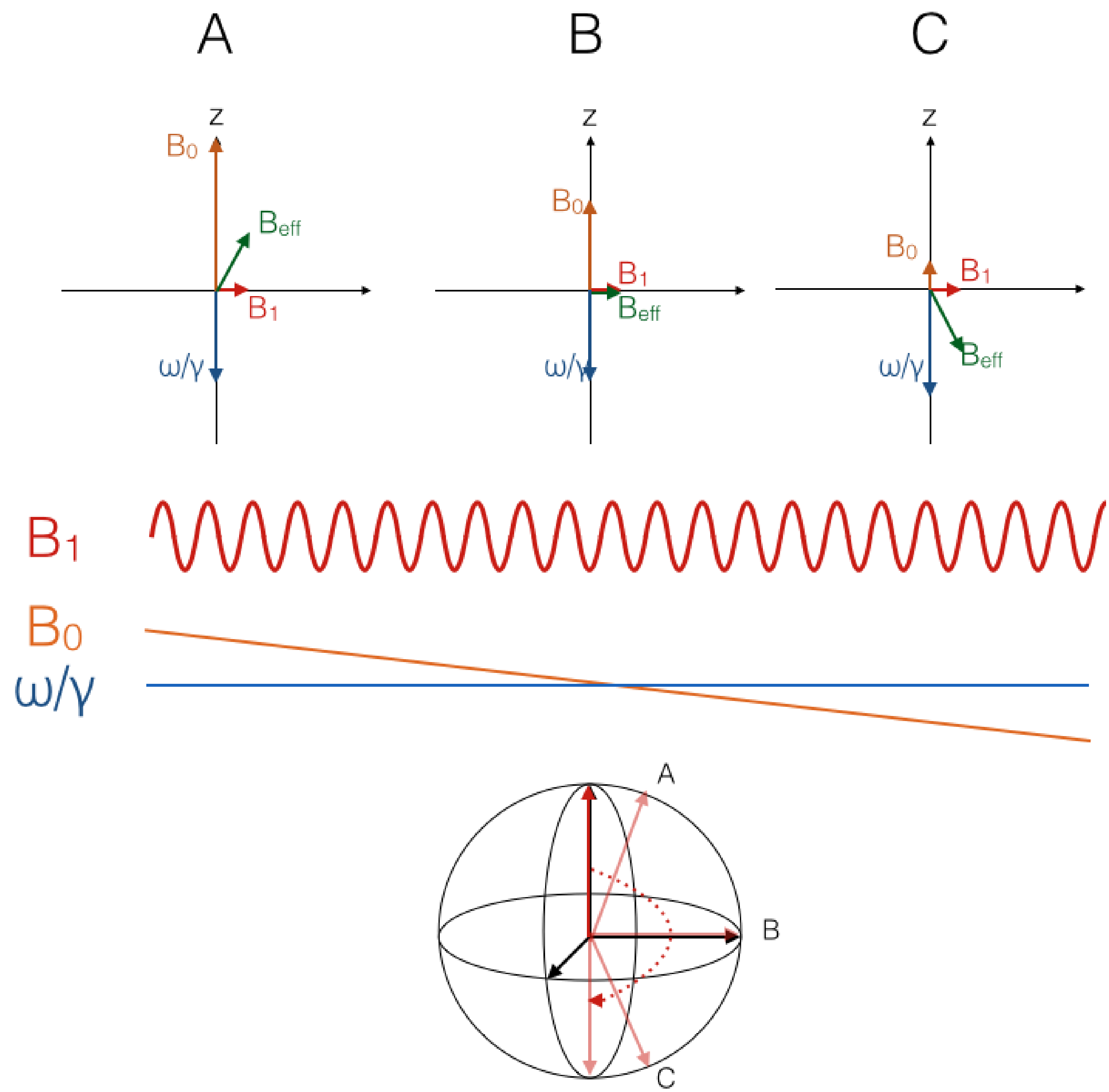


**Figure 2.10:** Adiabatic fast passage in a frame rotating at the $B_1$ frequency. $B_1$ is static in this frame, and the total effective magnetic field, $B_{eff}$ is the sum of the fields $B_0$, $B_1$ and $\omega/\gamma$. $B_{eff}$ tilts from pointing up along the $z$ axis to down along the $z$ axis as $B_0$ ramps through the $B_1$ resonance. At the top, the directions and strengths of the fields are shown at various points on the $B_0$ ramp. During the ramp, the magnitude of $B_0$ crosses over the magnitude of $\omega/\gamma$. At the bottom a Bloch Sphere representation of the direction of polarization through this process is shown.

## 2.7 Free Induction Decay

### 2.7.1 Overview

Free induction decay is, in principle, a very simple NMR experiment. Nuclei are spin polarized and placed in a magnetic field, $B_0$, and are allowed to precess freely after a $\pi/2$ pulse is applied. Over time, the nuclei de-polarize due to various relaxation processes that were described in Section 2.4.

A $\pi/2$ pulse is an RF pulse that is applied for exactly the duration necessary to rotate the spin vector by $\pi/2$ radians. It is driven by the $B_1$ field. Since the pulse needs to be applied for a precise period of time, effects from the rotating wave approximation need to be taken into account. The approximation is explained in detail in Section 1.1.3, but I will repeat the basic principle here. The nuclei are precessing, and their spin vectors trace out a circle on the *xy* plane. The $\pi/2$ pulse would ideally be driven by a field that follows the spin vector precisely, but such a field is difficult to create. A field that oscillates along some axis in the *xy* plane is equivalent to two counter-rotating fields on that plane. The field following the precession drives the $\pi/2$ flip, and the field rotating in the opposite direction does so quickly enough to have a negligible effect on the spin flip (this small effect is called the Bloch-Siegert shift and is small enough to ignore for FID). The main thing to note is that such a field has only half the effect on the nuclei's spins than a field that only rotates along with the spin vectors, so twice the duration than one might expect is needed to drive the $\pi/2$ pulse. To determine the pulse duration needed, one can simply calculate how long a fourth of a period of precession is for a given $B_1$ field strength:

$$\omega = \gamma B_1 \tag{2.27}$$

$$T = \frac{2\pi}{\gamma B_1} \tag{2.28}$$

The duration of the pulse is a fourth of this period, but with half of the strength of $B_1$, so

$$T_{\pi/2,\,\mathrm{RWA}} = \frac{\pi}{\gamma B_1}. \tag{2.29}$$

with $B_1$ being the actual amplitude of the RF pulse.

After the $\pi/2$ pulse, the polarization is measured as it diminishes over time due to relaxation effects. FID is an excellent way to measure the homogeneity of a magnetic field, as long as the $T_1$ and $T_2$ times are already well known, or are at least known to be much longer than $T_2^*$, since inhomogeneities have a clear and easily measured effect on the decay rate of the FID signal.

### 2.7.2 Detection and Signal

In essence, FID is a method for determining how quickly a non-equilibrium spin magnetization returns to equilibrium in a sample of atoms, and so, a potentially very accurate way to measure the $B_0$ field's homogeneity. Unlike AFP, which is quite resilient to relaxation processes, the signal in an FID experiment decays on the $T_2^*$ time scale. With a Boltzmann polarized sample, FID can be repeated if the sample has been given enough time (several $T_1$ periods) to return to its Boltzmann polarization. If the experiment is repeated before this $T_1$ relaxation, the amplitude of the FID signal will be diminished. With a hyperpolarized sample, the sample needs to be replaced to repeat the experiment.

This makes it very difficult to average many FID runs, potentially limiting the SNR that can be achieved.

Detection can be done with a pickup coil, just like AFP, where Faraday induction generates an EMF in the coil as the spins precess. The signal is sinusoidal, with frequency equal to the precession frequency of the sample in the $B_0$ field, with an exponentially decaying envelope. Unless the $\pi/2$ flip is repeated after the sample relaxes back to Boltzmann polarization, that is the entirety of the experiment. A spin echo can also be performed, by applying a $\pi$ pulse after $T_2^*$ relaxation is over, but not $T_1$. The details are explained in Section 2.4.2. The result is a brief revival of polarization, but weaker than the initial signal.

### 2.7.3 FID in the Context of UCN

FID is the technique that will be used to measure the magnetic field in the neutron EDM experiment. Detection will be done optically, with two atomic sources used simultaneously to independently measure the field and reduce systematic effects that occur when only one source is present. It is somewhat of a misnomer to call this method free induction decay, since there is no induction being measured, however, the technique differs only by the detection method. A continuous wave (CW) UV laser has been developed by another graduate student in our group, Emily Altiere, which will be used for detecting the precession frequency of $^{129}$Xe.

To demonstrate that this laser is capable of measuring the precession frequency of the $^{129}$Xe, I am constructing a set of coils to generate the necessary fields for FID. The first test is to perform AFP on Boltzmann polarized water (protons), with a pickup coil. This has several benefits. One is that detection with a pickup coil depends on fewer variables than with the laser. We do not need to ensure a precise wavelength, and we do not need to worry about alignment between many optical components, cavities and detectors. Using water as a source also eliminates the uncertainty in how well polarized $^{129}$Xe we have, as well as allowing us to see a baseline to compare the eventual $^{129}$Xe signal to. The signal from water can also be repeated and averaged over many runs, since its polarization is based on thermal equilibrium. After AFP, FID is performed on the water sample as well, in order to more precisely characterize the magnetic field generated by the coils. These two experiments are the scope of this thesis.

In the future, the coils can be adjusted and optimized based on the results of these experiments, and then the same experiments can be performed on hyperpolarized $^{129}$Xe, to determine the degree of polarization achieved, and to determine what signal to expect from the optical detection. The $^{129}$Xe itself is externally polarized via SEOP and then transported to the measurement cell.

On the optical side of the experiment, the first step is to see successful $^{129}$Xe spectroscopy. Simply, we will shine UV light on the $^{129}$Xe atoms and look for the IR emission. This will be done in a UV enhancement cavity. After that, we will look for a precession signal.

Once it has been determined that the laser is capable of measuring the magnetic field, it will first be used to measure the $^{129}$Xe EDM. This value is not yet known to enough precision to achieve the precision goal of the UCN neutron EDM measurement.

# Chapter 3

# Coils and Fields

## 3.1 Introduction

The experiments described in this thesis require several different magnetic fields, with different constraints on each of them. There is a strong, static magnetic field, $B_0$, and a weaker, radio frequency (RF) field that oscillates at the source particle's precession frequency in the $B_0$ field, the $B_1$ field, which must be perpendicular to $B_0$. There also needs to be a way to measure the precessing nuclei's spins, one method being to use a pickup coil and measure the Faraday induction as the magnetic field generated by the polarized particles changes direction during precession. Such a coil needs to be perpendicular to $B_0$ as well, and as will be described in Section 3.7, should also be perpendicular to $B_1$.

These experiments rely on a large number of in phase nuclei to make measurements. The precession frequency of the nuclei depends on the $B_0$ field, and since nuclei with even slightly different precession frequencies within a source will rapidly go out of phase, the magnitude of $B_0$ needs to be very uniform. The exact requirement depends on experimental factors, such as the actual precession frequency of the nuclei, and the in phase time needed to make a reasonable measurement. The bulk of this chapter will discuss the generation of a homogeneous $B_0$ field under the conditions imposed by the optical measurement with our ultraviolet (UV) laser.

The fields themselves are generated by an electrical current, and there are several potentially useful coil geometries for creating a uniform field. In Sections 3.2 and 3.3 I will go over the two geometries I considered for the $B_0$ coils, the Helmholtz configuration, and the saddle configuration. To determine their usefulness in these experiments, I coded some simulations, and took advantage of some known analytic solutions to compare my results along the axes where the analytic solution is easily solvable. The goal is to make as homogeneous as possible a $B_0$ field, across the experimental region, which is a glass cell, 200 mm long and with a diameter of 25.4 mm, filled with $^{129}$Xe. One challenge is that the $B_0$ field needs to be directly above a steel optical table. As will be discussed in Section 3.4, the steel distorts the magnetic field, potentially increasing the field's inhomogeneity.

Figure 3.1 shows the coils that are used in this experiment (in this case with saddle coils for the $B_0$ field), and the cell, above the steel optical table. $B_0$ points straight up out of the table, and defines the $z$ axis in this thesis. The $x$ axis is down the long axis of the $^{129}$Xe cell, and the $y$ axis is oriented such that the coordinate system is right handed. The center of the cell defines the origin.

All of the Matlab code used in the simulations described in this chapter is reproduced in the Appendix.

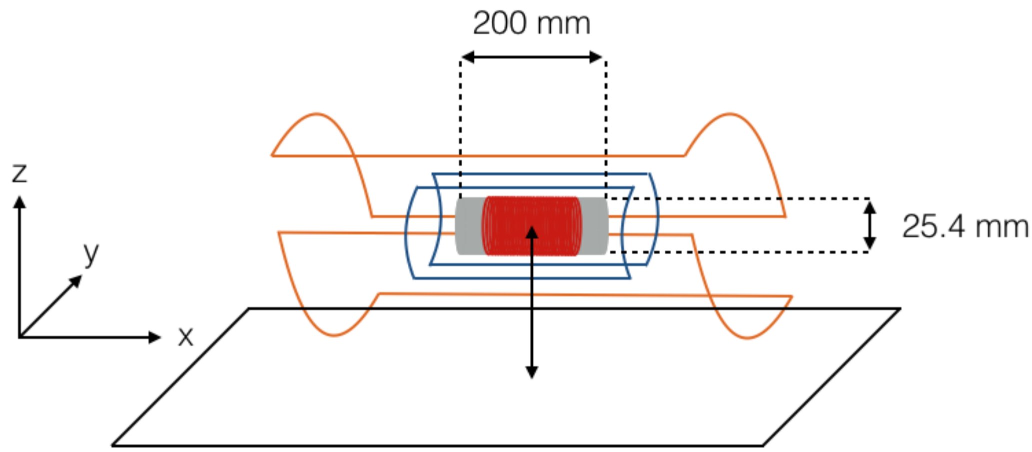


**Figure 3.1:** This is a schematic of the coils needed to perform NMR experiments, shown with Saddle shaped coils, as well as the $^{129}$Xe cell that will be used. The entire setup is suspended above a steel optical table. The cell is a 25.4 mm diameter cylinder, 200 mm long, and placed in the center of the setup. A pickup coil is wrapped around it (red). The $B_0$ (orange) and $B_1$ (blue) coils are also shown.

## 3.2 Helmholtz Configuration

The Helmholtz configuration is named after the German physicist Hermann von Helmholtz. It is a very simple geometry for creating a uniform magnetic field in a small space between the coils. This configuration, shown in Fig. 3.2, consists of two loops of wire of equal radius. There is an equal current, running in the same direction, through each loop, and they are separated by their radius. The geometry can be adjusted by changing their separation if

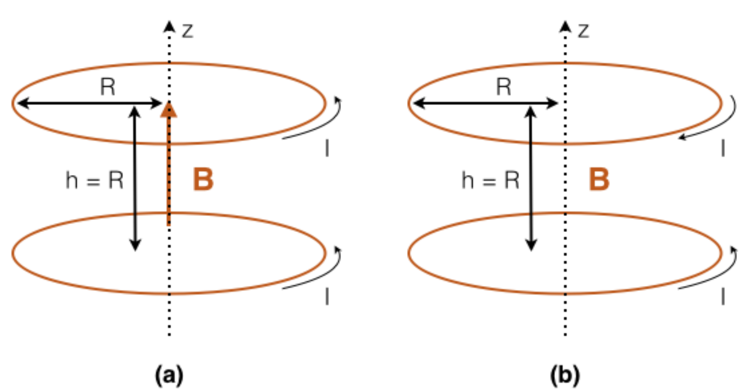


**Figure 3.2:** (a) A pair of current loops in the Helmholtz configuration. The distance between them is equal to the radius of each loop, and the field generated points straight up. The field is relatively homogeneous near the center of the coils. (b) The anti-Helmholtz geometry, where the current in each loop runs in opposite directions. The magnetic field generated from these is a gradient, which is linear near the center of the coils. The field strength at the center is 0.

certain effects are desired. For example, by moving them farther from each other, there is a local minimum in the field at the center. The current in one loop can also be reversed, to produce an anti-Helmholtz geometry. The resulting field is a linear gradient.

Calculating the field along the $z$ axis for the Helmholtz configuration is simple, since all of the field components other than the $z$ component cancel out. A loop of wire in the $xy$ plane generates a field on the $z$ axis that is given by[24]:

$$B_z(z) = \frac{\mu_0 I}{2} \frac{R^2}{(R^2+z^2)^{3/2}}. \tag{3.1}$$

Modifying the equation to get the field of a Helmholtz pair is simply a matter of moving the coordinates a bit so that the origin is at the center of the pair, and adding the contributions of both coils.

$$B_z(z) = \frac{\mu_o I}{2} \frac{R^2}{(R^2+(z+R/2)^2)^{3/2}} + \frac{\mu_o I}{2} \frac{R^2}{(R^2+(z-R/2)^2)^{3/2}}. \tag{3.2}$$

The field elsewhere does not have a simple analytic solution, and to calculate it, I used a finite differences simulation instead. In such a simulation, a differential equation is split into many discrete parts, and the contribution of each part is added together. In this case, the equation is the Biot-Savart Law:

$$\mathrm{d}\vec{B} = \frac{\mu_0 I \mathrm{d}\vec{l} \times \vec{r}}{4\pi |r|^3}, \tag{3.3}$$

where, $\mu_0 = 4\pi \times 10^{-7}$ is the permeability of free space, $I$ is the current going through the piece of wire and $\vec{r}$ is the vector pointing from the piece of wire, $\mathrm{d}\vec{l}$, to the point you are calculating the field for. The integral form of this equation leads to equation 3.1.

To calculate the field at a given point with a computer, $\mathrm{d}\vec{l}$ cannot be infinitely small, like when using the analytic solution. First, a size for $\mathrm{d}\vec{l}$ is chosen, and the Biot-Savart law is used to calculate the field generated by the piece of wire with length $\mathrm{d}\vec{l}$. This is then iterated over the entire loop, and all of the contributions from the pieces of wire are added up. However, these pieces of wire are necessarily approximated as straight, so the simulation actually generates the result for a field from a polygon. This approximation gets more accurate for smaller $\mathrm{d}\vec{l}$, but at the cost of computing time since there are more iterations to go through and sum up. Thus, there is a trade-off between accuracy and speed in the simulation. Fortunately, the simulation can be compared to the analytic result along the $z$ axis, so there is a means to determine what size $\mathrm{d}\vec{l}$ is necessary for the desired precision.

It is also useful to test that the simulation really does get more accurate for smaller $\mathrm{d}\vec{l}$. The simulation is run repeatedly over the region where the analytic solution is known, for smaller and smaller $\mathrm{d}\vec{l}$. Since a small region is calculated, it is possible to go to higher precision than would be practical for the entire simulation. The results are analyzed to look for convergence (the simulation should converge on a value rather than, for example, oscillating) and to see what size $\mathrm{d}\vec{l}$ is necessary to achieve the desired precision. This is known as a convergence test.

The result of testing my simulation for a Helmholtz pair is show in Fig. 3.3. The simulation was tested both at the center (top plot) and at the edge of the $^{129}$Xe cell (bottom plot). The value at the center does not require much resolution at all in the simulation, and the field at the edge of the cell converges very rapidly. It is accurate to 5 decimal places, even at only 16 pieces per loop. Since this simulation does not take long to run, I divided up the loops into 50 pieces.

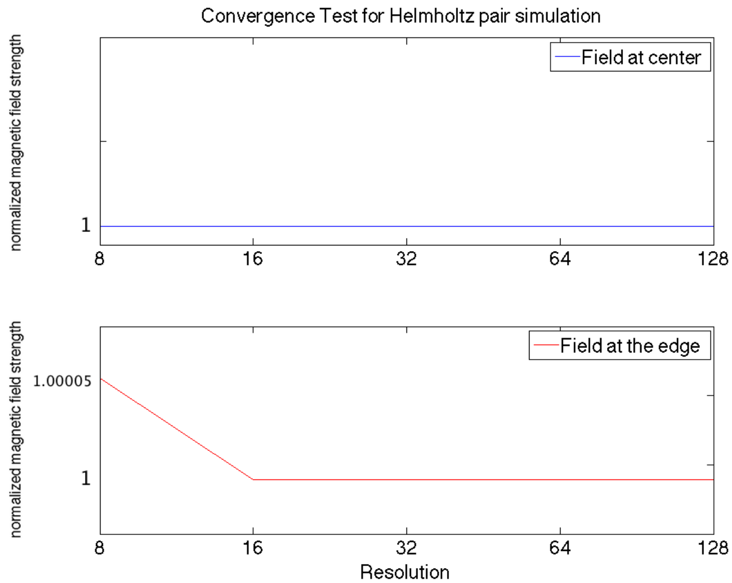


**Figure 3.3:** This is the convergence test for the Helmholtz pair simulation. The $y$ axis shows the value of the magnetic field at the center and edge of the $^{129}$Xe cell calculated at the resolution given by the $x$ axis. The resolution is the number of straight line pieces the coils are divided into when performing the simulation. At the center of the cell, the simulation is accurate even at very low resolutions. The field calculated at the edge of the cell benefits from a higher resolution, but converges rapidly.

Figure 3.4 shows the results of the analytic and the simulated results, for the magnitude of the $B_0$ field along the $z$ axis. These plots are for coils with radius $R = 300$ mm, 100 windings and a current of 4.04 A, generating a field at the center of about 1.2 mT. There is good agreement for both methods, suggesting that the simulation should be accurate over the entire experimental region.

## 3.3 Saddle Coil Configuration

Another possible configuration to create a homogeneous magnetic field is called the saddle coil. This geometry also consists of two coils, but rather than than two loops, each coil consists of two straight pieces, or “rungs,” and two curved sections, “arcs,” connecting the rungs. Figure 3.5 shows the geometry needed to create a vertical magnetic field.

### 3.3.1 Simulation

The field generated by the rungs has a simple analytic expression, which can be derived directly from the integral form of the Biot-Savart law, and using some quantities defined in Fig. 3.6.

$$\int_{\mathrm{A}}^{\mathrm{B}} \frac{\mu_0 I}{4\pi} \frac{\vec{r} \times \mathrm{d}\vec{l}}{|r|^3} \tag{3.4}$$

It is simplest in this case to calculate the magnetic field’s magnitude, and determine the direction by other methods such as the right hand rule, rather than by carrying through the vector properties of the cross product, so:

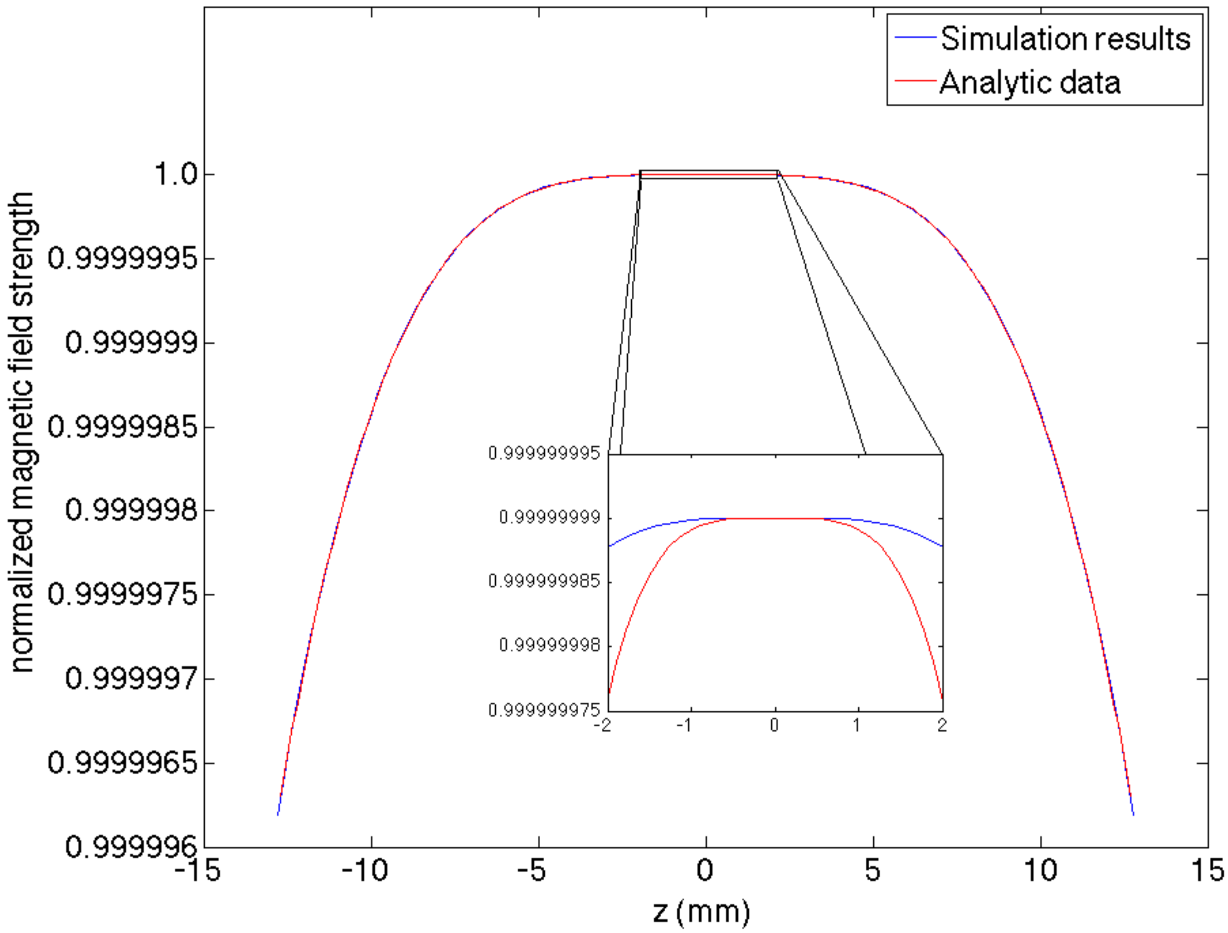


**Figure 3.4:** Simulated and analytic results for the magnetic field in the z direction, along the z axis, for a Helmholtz pair of coils, with total current of 404 A, and a coil radius and separation of 300 mm.

$$|\vec{r} \times \mathrm{d}\vec{l}| = r\mathrm{d}l\sin(\theta + 90) = r\mathrm{d}l\cos(\theta). \tag{3.5}$$

Both $r$ and d$l$ can also be written in terms of $\theta$:

$$r = \frac{s}{\cos(\theta)} \tag{3.6}$$

$$r\mathrm{d}\theta = \mathrm{d}l\cos(\theta) \tag{3.7}$$

As shown in Fig. 3.6, $s$ is the distance from the wire to the measurement point and $\theta$ the angle made by $s$ and $r$. Equations 3.4, 3.6 and 3.7 can be put together, and after canceling some terms, and changing the limits of integration to the initial and final angles:

$$\mathbf{B} = \int_{\theta_1}^{\theta_2} \frac{\mu_0 I \cos(\theta)}{4\pi s} \mathrm{d}\theta = \frac{\mu_0 I}{4\pi s} \left[\sin(\theta_2) - \sin(\theta_1)\right]. \tag{3.8}$$

Equation 3.8 only gives the magnitude of the magnetic field, but the direction is then easily determined by the right hand rule. For example, in Fig. 3.6, the field comes out of the page at the point shown.

The contributions to the field by the arcs of the saddle coil must be calculated with a finite difference simulation again, like the calculation for the Helmholtz configuration. Figure 3.7 shows the convergence test on the number of pieces to divide the coil into. In this test, the exact result was used for the rungs, which was added to the simulated result for the arcs. The $x$ axis of these plots is the number of pieces the arcs were divided into for the simulation. The plots show the result for the field at the center, as well as for the inhomogeneity along the $x$ axis. In my simulations for the saddle coils I divided up the arcs into 200 pieces. This slightly overestimates the field strength and inhomogeneity, but the computation time becomes prohibitive for higher resolutions.

The final results of these simulations are shown at the end of the next section, in Fig. 3.8, along with the analytic results to compare them to.

### 3.3.2 Analytic Formulae

There are also analytic formulae that can be used to check the simulation results. They are actually valid for all space, but are computationally very expensive except near the axes. Because of this, it is actually more efficient to use a simulation to determine the field, and compare it to the analytic results along the axes.

The field generated by a saddle shaped coil can be found to be[25]:

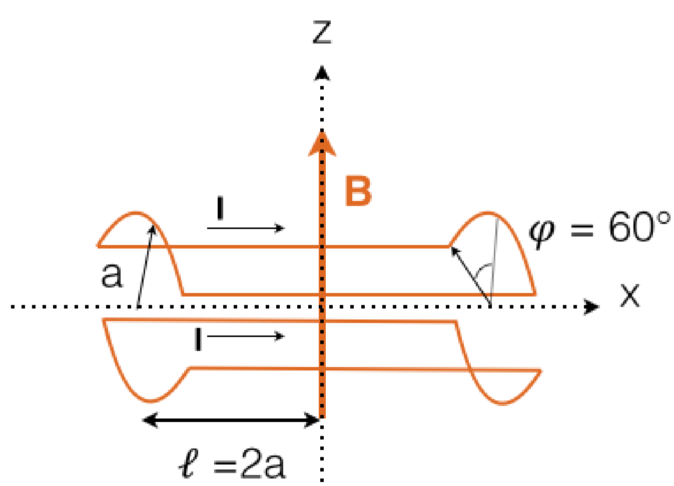


**Figure 3.5:** The saddle coil geometry. Shown are common ratios for parameters: the half-length $l$ is twice the radius $a$ of the arcs, which have a half-span $\varphi$ of 60°. For consistency with the Helmholtz configuration, B at the center points along the $z$ axis, and the coil axis is in the $x$ direction. The current flows in the same direction in each coil.

$$\begin{pmatrix} B_\rho \\ B_\phi \\ B_x \end{pmatrix} = \frac{\mu_0}{2\pi} \sum_{m=-\infty}^{\infty} \mathrm{e}^{im\phi} \int_{-\infty}^{\infty} \mathrm{d}k\, \mathrm{e}^{ikx} \times \begin{pmatrix} \frac{k^2}{im} a^2 P_m(a) F_x^m(k) \\ \frac{k}{\rho} a^2 Q_m(a) F_x^m(k) \\ \frac{k^2}{m} a^2 Q_m(a) F_x^m(k) \end{pmatrix} \tag{3.9}$$

where

$$P_m(a) = \begin{cases} I'_m(k\rho)K'_m(ka) & \text{when } \rho < a \\ I'_m(ka)K'_m(k\rho) & \text{when } \rho > a \end{cases} \tag{3.10}$$

$$Q_m(a) = \begin{cases} I_m(k\rho)K'_m(ka) & \text{when } \rho < a \\ I'_m(ka)K_m(k\rho) & \text{when } \rho > a \end{cases} \tag{3.11}$$

and

$$F_x^m(k) = \frac{-i4I}{\pi ka} \sin(kl) \sin(m\varphi) \delta_{m,\text{odd}}. \tag{3.12}$$

Here, $\rho$, $\phi$ and $x$ are cylindrical coordinates (I use $x$ rather than $z$ to maintain consistency with the $z$ direction being the direction of the generated magnetic field), $\mu_0 = 4\pi \times 10^{-7}$ is the permeability of free space, $a$ is the radius, $\varphi$ half of the span, and $l$ half of the length of the coils, $I$ and $K$ are the modified Bessel functions and $I'$ and $K'$ are their derivatives.

The region of interest is the field inside the coils, so $\rho < a$. The result is given in Bidinosti 2005 [25], but I will

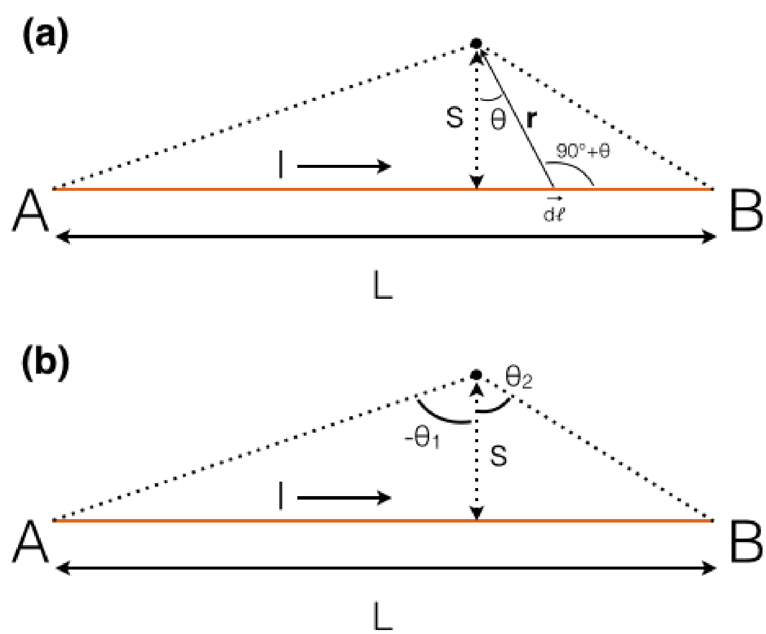


**Figure 3.6:** Calculating the magnetic field generated by a straight wire. (a) Shows the variables used in the integral in equation 3.4. (b) Shows the relevant variables that are used to directly calculate the field for the whole length of wire, equation 3.8. Note that $\theta_1$ is negative when taken directly from $s$ as shown.

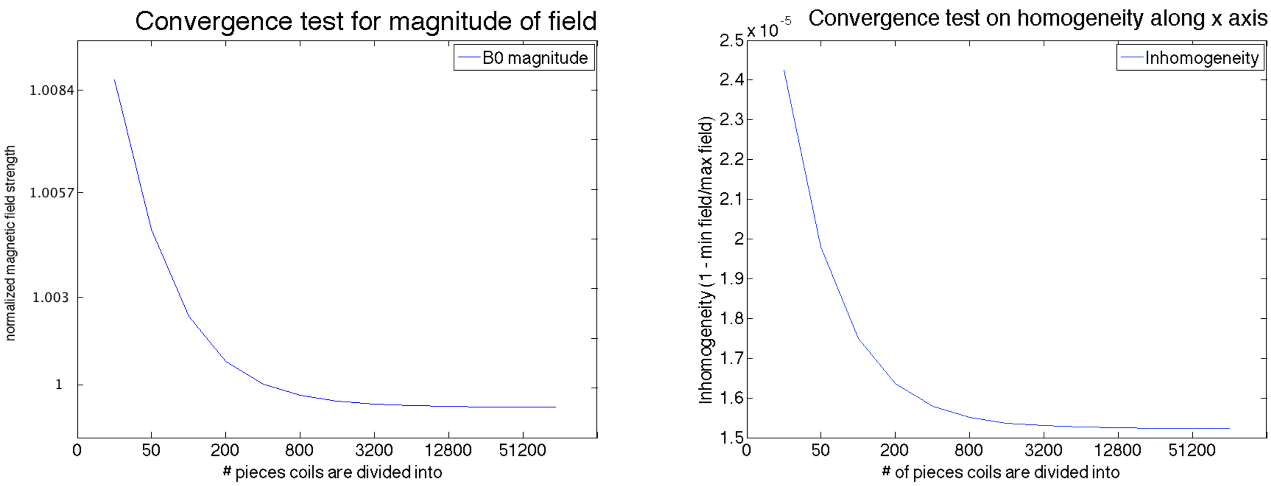


**(a)** Convergence test for the magnitude of the field at the center of a saddle coil configuration. The field strength converges to a bit below 1.488 mT.

**(b)** Convergence test for the inhomogeneity of the field along the $x$ axis. The inhomogeneity converges to about 15 parts per million.

**Figure 3.7**

briefly show the derivation for $B_\rho$. The first step is to combine the equations 3.9, 3.10, and 3.12 (equation 3.11 is used for $B_\phi$ and $B_x$, but not $B_\rho$). Constants can be pulled out to the front and combined, leaving:

$$B_\rho = \frac{-2\mu_0 a I}{\pi^2} \sum_{m=-\infty}^{\infty} [\cos(m\phi) + i\sin(m\phi)]\delta_{m,\text{odd}} \int_{-\infty}^{\infty} \mathrm{d}k\, [\cos(kx) + i\sin(kx)] \frac{k}{m} I'_m(k\rho) K'_m(ka) \sin(kl)\sin(m\varphi), \quad (3.13)$$

where I have also used $\mathrm{e}^{ix} = \cos(x) + i\sin(x)$. This can be simplified by considering the symmetry in $m \to -m$ and $k \to -k$. These identities for the modified Bessel functions and their derivatives are also useful[26]:

$$I'_m(x) = \frac{1}{2}\left[I_{m-1}(x) + I_{m+1}(x)\right], \quad (3.14)$$

$$K'_m(x) = -\frac{1}{2}\left[K_{m-1}(x) + K_{m+1}(x)\right], \quad (3.15)$$

$$I_{-m}(x) = I_m(x), \quad (3.16)$$

$$K_{-m}(x) = K_m(x). \quad (3.17)$$

Putting them together, $I'$ and $K'$ are symmetric functions, as is cos. Sin and $k/m$, however are antisymmetric for each transformation, so out of the four terms that come out of multiplying out the exponential, only the $\cos(m\phi)\cos(kx)$ term is symmetric overall. The rest are all antisymmetric and cancel out when the whole sum or integral is computed, as they both run from $-\infty$ to $\infty$. For the surviving term, the limits of integration and the sum can both be changed to be completely positive. The term then needs to be multiplied by four, since each change in the limit of integration or sum removes half of the contribution to the total field. The result is:

$$B_\rho = \frac{-8\mu_0 Ia}{\pi^2} \sum_{m=1,3,5,...}^{\infty} \cos(m\phi) \int_0^\infty \mathrm{d}k \frac{k}{m} \cos(kz) I'_m(k\rho) K'_m(ka) \sin(kl) \sin(m\varphi). \tag{3.18}$$

The equations for $B_\phi$ and $B_x$ can be obtained in a similar fashion and after some rearranging of terms for compactness, are[25]:

$$\begin{pmatrix} B_\rho \\ B_\phi \\ B_x \end{pmatrix} = \frac{8\mu_0 Ia}{\pi^2} \sum_{m=1,3,5,...}^{\infty} \sin(m\varphi) \int_0^\infty \mathrm{d}k \, \sin(kl) K'_m(ka) \times \begin{pmatrix} \frac{-k}{m} \cos(m\phi)\cos(kx) I'_m(k\rho) \\ \frac{1}{\rho} \sin(m\phi)\cos(kx) I_m(k\rho) \\ \frac{k}{m} \cos(m\phi)\sin(kx) I_m(k\rho) \end{pmatrix}. \tag{3.19}$$

This equation can be further manipulated to put it into a more useful form to compare simulations to. The $z$ component (which is vertical out of the table, transverse to the saddle coil, see Fig. 3.1) of the field can be calculated along the $x$, $y$ and $z$ axes. The $x$ axis is fairly simple, since for $\rho = 0$, only the $m = 1$ term contributes to the field in the $z$ direction. This is because as $\rho \to 0$,

$$I_m(k\rho) \to \left(\frac{k\rho}{2}\right)^m / m! \tag{3.20}$$

and

$$I'_m(k\rho) \to \frac{1}{2} \left(\frac{k\rho}{2}\right)^{m-1} / (m-1)!. \tag{3.21}$$

For $m > 1$ these both go to 0, but for $m = 1$, $I'_1(k\rho) \to 1/2$. So, to get the field in the $z$ direction, along the $x$ axis, the $B_\rho$ equation for $\rho = 0$ and $\phi = 0$, and equation 3.15 can be used, to obtain:

$$B_z(x) = \frac{2\mu_0 a}{\pi^2} \sin(\varphi) \int_0^\infty \mathrm{d}k \; k \sin(kl) \cos(kx) \left[K_2(ka) + K_0(ka)\right]. \tag{3.22}$$

The $z$ axis goes up out of the table, so $\phi = 0$. The field in the $z$ direction along this axis is just $\mathrm{B}_\rho$ with $\rho = z$, again making use of equations 3.14 and 3.15:

$$B_z(z) = \frac{2\mu_0 Ia}{\pi^2} \sum_{m=1,3,5,...}^{\infty} \sin(m\varphi) \int_0^\infty \mathrm{d}k \frac{k}{m} \sin(kl) \cos(kx) \left[K_{m-1}(ka) + K_{m+1}(ka)\right] \left[I_{m-1}(kz) + I_{m+1}(kz)\right]. \tag{3.23}$$

And finally, the $y$ axis is parallel to the table, at $\phi = \pi/2$, and with the field in the $z$ direction being $\mathrm{B}_\phi$, and $\rho = y$.

$$B_z(y) = \frac{4\mu_0 Ia}{\pi^2} \sum_{m=1,3,5,...}^{\infty} \sin(m\varphi) \sin(m\frac{\pi}{2}) \int_0^\infty \mathrm{d}k \frac{\sin(kl)}{y} \left[K_{m-1}(ka) + K_{m+1}(ka)\right] I_m(ky). \tag{3.24}$$

Equation 3.22 can be calculated for good precision in the magnetic field calculation, even when truncating the integration for computation time. Equations 3.23 and 3.24 involve an infinite sum, so these need to be approximated by also truncating the sum in addition to truncating the integration. Fortunately, I found them to converge very rapidly, and including just the first three terms ($m = 1,3,5$) is sufficient for accuracy to about 10 parts in $10^9$.

| Number of terms in sum ($m$ = 1, 3, 5...) | limit of integration | value for $B_0$ (T) at cell edge | normalized $B_0$ |
|---|---|---|---|
| 2 | 100 | 0.001487225401 | 1.000015150589 |
| 2 | 1000 | 0.001487225399 | 1.000015149245 |
| 2 | 10000 | 0.001487225399 | 1.000015149245 |
| 3 | 100 | 0.001487202871 | 1.000000001345 |
| 3 | 1000 | 0.001487202869 | 1 |
| 3 | 10000 | 0.001487202869 | 1 |
| 4 | 100 | 0.001487202961 | 1.000000061861 |
| 4 | 1000 | 0.001487202960 | 1.000000061189 |
| 4 | 10000 | 0.001487202960 | 1.000000061189 |

**Table 3.1:** Test for precision for the calculation of the magnetic field of a pair of saddle coils. I chose to include 3 terms in the sum and use $k$ = 1000 as the limit of integration. This should be accurate to 10 parts in $10^9$.

Truncating the integration to $k$ = 1000 for calculating the field along each axis is acceptable for similar precision. This is easily enough precision to be useful as a check for the accuracy of the Biot-Savart simulation. The test for precision of the analytic calculation is shown in table 3.1. Higher values of $m$ are required for an accurate calculation as one goes further from the origin, so this precision test was done at the edge of the cell containing the polarized $^{129}$Xe, or about 12.7 mm from the center of the coils, rather than at the center.

Shown in Fig. 3.8 is the results of running these analytic formulae in Maple, as well as the results from the simulation described in Section 3.3.1. For the $y$ and $z$ axes, the calculation is run over the cell's radius in each direction, which is half an inch, or about 12.7 mm. For the $x$ axis, which is the long axis of the coil and cell, it is run over the length of the cell, which is about 100 mm in each direction.

For both the Helmholtz configuration, and the saddle configuration, the cell region has very small inhomogeneity, small enough for either to be useful without modification to perform adiabatic fast passage (AFP) and free induction decay (FID). However the magnetic field can be distorted by external fields, or by nearby magnetic metals. This becomes a serious issue due to the constraints imposed on our setup by the requirements to do the optical detection, specifically the requirement that these coils are placed just above our steel optical table. This is described in Section 3.4. The saddle geometry has the benefit that it can be extended along the $x$ direction, meaning that the region of good homogeneity can easily be made larger along that axis without increasing the size of the coils in other directions. This is useful since the $^{129}$Xe cell being used is quite long and thin.

## 3.4 Image Fields

Due to the nature of the $^{129}$Xe spectroscopy experiment, these coils need to be placed just above the same optical table that the UV laser is built on. This is mainly due to the enhancement cavity for the UV light that will surround the $^{129}$Xe cell. The optical components in this cavity must be mechanically very stable, so that the feedback and locking electronics can reduce fluctuations in the cavity length to sub-wavelength amplitudes. There is a significant drawback for this in terms of the homogeneity of the magnetic fields, though. The optical table is made of steel, which will deform nearby fields significantly due to its relatively high $\mu_r$.

Fortunately, these effects can be approximated and simulated, using the method of images. The idea is similar to using image charges in electrostatics, where an imaginary "image charge" can be placed on the other side of a

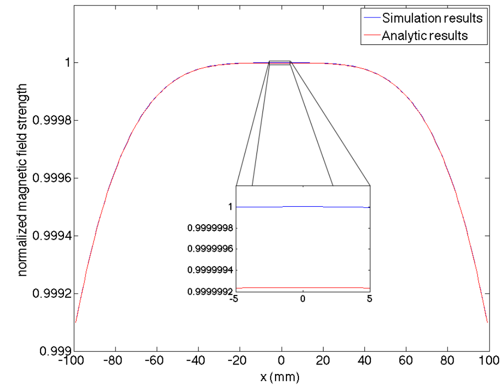


**(a)**

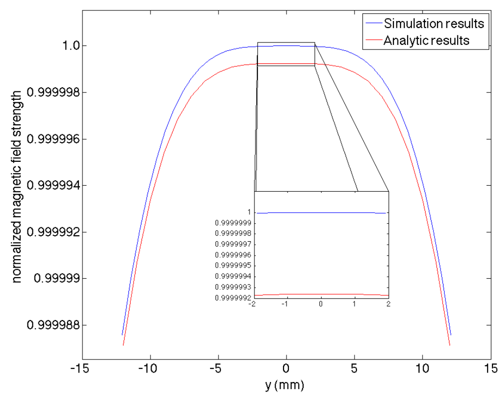


**(b)**

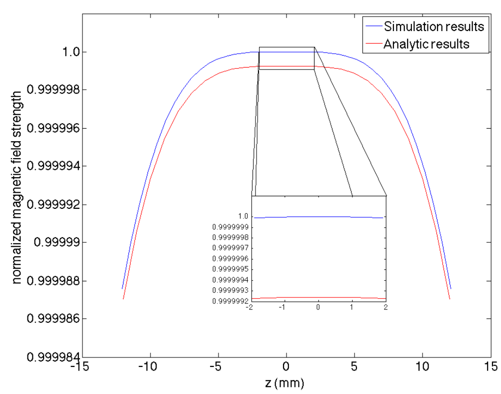


**(c)**

**Figure 3.8:** A comparison of the analytic and simulated results for the magnetic field in the $z$ direction, created by saddle coils. Plot (a) shows the field along the $x$ axis, plot (b) the $y$ axis and plot (c) the $z$ axis. The results agree very closely.

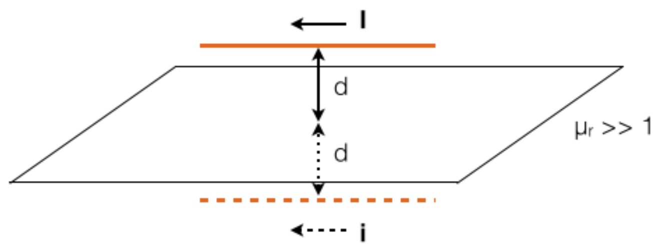


**Figure 3.9:** The image current of a piece of straight wire above a high permeability material such as steel. The current of the image (i) goes the same direction as the actual current (I).

planar conductor from a test charge, to create a plane of zero potential. In the magnetostatic case, one can use an "image current" instead. Assuming an infinite, flat plane boundary, the image current is simple to calculate[27]:

$$i = \frac{\mu_r - 1}{\mu_r + 1} I, \tag{3.25}$$

where $\mu_r = \mu/\mu_0$ is the relative permeability of the material creating the boundary, $I$ is the actual current, and $i$ is the image current. The image current sits on the opposite side of the boundary, the same distance away as the actual current. There are two limiting cases in which calculating the image current is trivial. One case is when $\mu_r = 0$, such as in the case of a superconducting boundary, in which $i = -I$. The other case is when $\mu_r \gg 1$, so $i \approx I$. Steels tend to have $\mu_r$ on the order of 1000 or more, so I use $i = I$ in my image field calculations. A straight piece of current above a high-$\mu$ material and its image are shown in Fig. 3.9.

Once the image current has been calculated, the field generated by this current can be calculated using the same techniques as for the field from the actual current. The only change is that the position of the image current is different; it is below the table rather than around the origin. In the case for geometries where the coils don't have current running in the same direction (the anti-Helmholtz configuration, for example), care must be taken to ensure that the image currents are chosen to be going in the correct direction for the top and bottom coils. The image is a mirror of the actual coils.

Equation 3.9 can also be used to find the field outside of the coils in a saddle coil geometry, analytically, which is useful to calculate the image field. The relevant formulae can be obtained in the same way as equation 3.19, but choosing the appropriate $P_m$ and $Q_m$ for $\rho > a$. The result is very similar to the field inside the coils:

$$\begin{pmatrix} B_\rho \\ B_\phi \\ B_x \end{pmatrix} = \frac{8\mu_0 I a}{\pi^2} \sum_{m=1,3,5,\ldots}^{\infty} \sin(m\varphi) \int_0^\infty \mathrm{d}k \, \sin(kl) I'_m(ka) \times \begin{pmatrix} \frac{-k}{m}\cos(m\phi)\cos(kx)K'_m(k\rho) \\ \frac{1}{\rho}\sin(m\phi)\cos(kx)K_m(k\rho) \\ \frac{k}{m}\cos(m\phi)\sin(kx)K_m(k\rho) \end{pmatrix}, \tag{3.26}$$

and the corresponding field in the $z$ direction along the $z$ axis is

$$B_z(z) = \frac{2\mu_0 a I}{\pi^2} \sum_{m=1,3,5,\ldots}^{\infty} \sin(m\varphi) \int_0^\infty \mathrm{d}k \, \sin(kl) \left[ I'_m(ka) K'_m(kz) \right]. \tag{3.27}$$

I ran this calculation in Maple along the $z$ direction to have something to compare the simulation to. The calculation off axis was prohibitive in terms of the time required (and in this case, the $x$ and $y$ axes are not "on axis"

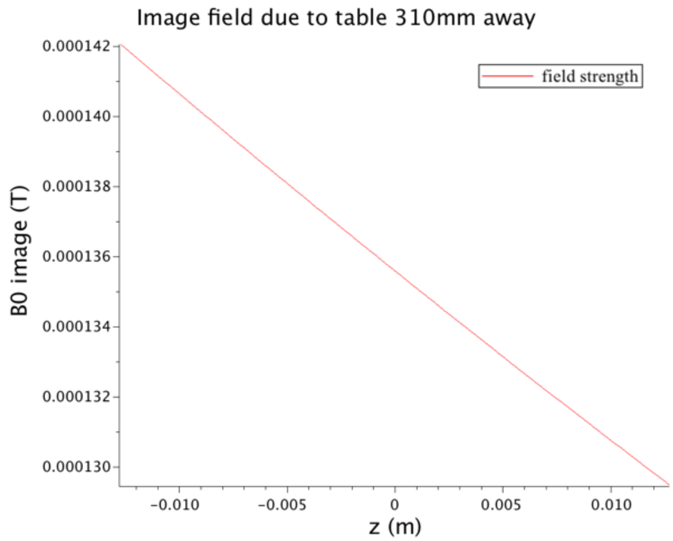


**Figure 3.10:** A calculation of the field along the z axis due to the image current from a saddle coil.

| Number of terms in sum ($m$ = 1, 3, 5...) | value for $B_0$ (T) at center | normalized $B_0$ |
|---|---|---|
| 2 | 0.00013643552773 | 1.0062202016 |
| 3 | 0.00013551496688 | 0.9994310101 |
| 4 | 0.00013559262322 | 1.0000037302 |
| 5 | 0.00013559262322 | 1.0000037302 |
| 6 | 0.00013559207121 | 0.9999996591 |
| 7 | 0.00013559211775 | 1.0000000024 |
| 8 | 0.00013559211775 | 1.0000000024 |
| 9 | 0.00013559211743 | 1 |

**Table 3.2:** Precision test for the image field produced at the center of a pair of saddle coils by a steel optical table, with the integration limits being $k = 0$ to $k = 1000$. Seven terms in the sum is sufficient for 10 parts in $10^9$ precision.

for the image field), but just calculating the exact field on the $z$ axis is still a good check. Figure 3.10 shows the result of this calculation across the diameter of the cell.

Even on axis, the integral and the sum in equation 3.26 need to be truncated to calculate within a reasonable time frame. Table 3.2 shows the results of adjusting the limits of the sum. To get to 10 parts in $10^9$ precision, 7 terms are needed. Figure 3.11 shows the analytic and simulated results for the $B_0$ field in the $z$ direction for a saddle coil with radius $a$ = 180 mm, half-length $l$ = 500 mm and half-span $\varphi = 60°$, sitting 310 mm above a steel table. The effects of the table are very obvious (compare Fig. 3.11 to Fig. 3.8); there is a strong gradient along the $z$ direction that will need to be compensated for. Methods for doing so are described in Section 3.8.

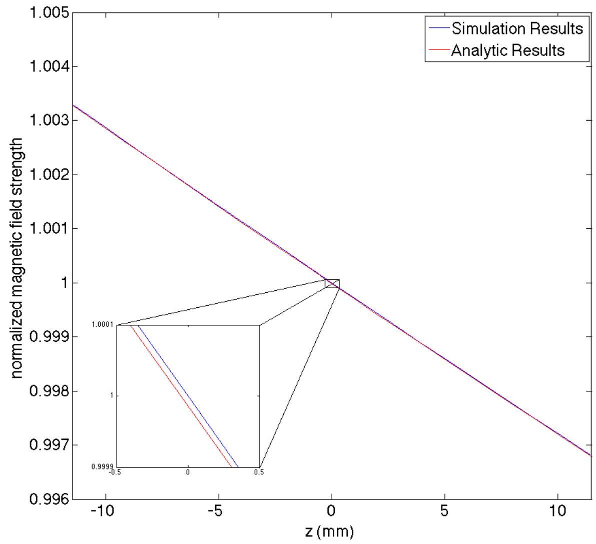


**Figure 3.11:** This is the magnetic field in the $z$ direction, along the $z$ axis, generated by saddle coils with dimensions radius $a$ = 180 mm, half-length $l$ = 500 mm and half-span $\varphi = 60°$ with a high-$\mu_r$ steel table 310 mm away in the -$z$ direction. The plots are calculated using the analytic formula (in red), and using the simulation (in blue). There is strong agreement.

## 3.5 External Fields

The final contribution to the total magnetic field in the experimental region is from all of the other magnetic fields present due to external sources. In most environments, this will be dominated by the earth's own local magnetic field. The strength of this field varies somewhat over the surface, but is generally about 0.25 to 0.65 Gauss, or 25-65 $\mu$T. In particular, around Vancouver, Canada where these experiments took place, it is about 54 $\mu$T[28].

Other contributions can include currents from nearby electronics, and nearby permanent magnets. These tend to contribute very little to the static field, though. The currents used to generate the fields I am using are on the order of hundreds of amps, and are close to the experimental region. There is no reason to have permanent magnets in the experimental region in this experiment, so those are not a concern either, although it is important to make sure that there aren't any placed nearby accidentally. For example, some optical mounts and bases have magnets built in, and these are frequently placed right next to these coils to perform measurements on the UV laser. These must be removed before performing NMR experiments with the coils.

Finally, there is the possibility of nearby magnetic materials, which will distort the field, like the optical table does. This is best mitigated by simply going over all of the components with a weak magnet and determining which ones are attracted to it. If possible, all such components are replaced with non-magnetic ones, such as those made of aluminum or brass. In our lab the biggest offenders are our precision translation stages.

## 3.6 $B_1$

So far, this chapter has focused on the generation of a uniform, static $B_0$ field. NMR experiments also require an RF field to perform the necessary spin flips, however. This $B_1$ field oscillates at the resonant frequency of the nuclei in

| Source | $\gamma$ (MHz/T) | Frequency at 1.5 mT (kHz) |
|---|---|---|
| $^{129}$Xe | -11.777 | 17.666 |
| $H_2O$ (proton) | 42.577 | 63.866 |

**Table 3.3:** Gyromagnetic ratios $\gamma$ and precession frequencies for some sources in a 1.5 mT magnetic field.

the $B_0$ field, and so is at a different frequency for different sources. The purpose of this field is to rotate the spin axis of the source nuclei. In general, NMR experiments begin with a $\pi/2$ pulse to put the spins into the *xy* plane, from the initial polarization along *z*.

The reason this field needs to be oscillating, rather than direct current (DC) like the $B_0$ field is that the nuclei's spins will be precessing around $B_0$ during the flip. An additional DC field would simply rotate the axis of precession. Instead, the oscillating $B_1$ field follows the source nuclei around the *z* axis, to provide a constant torque towards the *xy* axis. When doing FID, $B_1$ is turned off after the spin has been rotated by $\pi/2$. The details of this spin flip and the rotating wave approximation have been explained in Section 1.1.3, but I will give a brief summary here.

The nuclei are precessing, and their spin vectors trace out a circle on the *xy* plane. The $\pi/2$ pulse would ideally be driven by a field that follows the spin vector precisely, but such a field is difficult to create. A field that oscillates along some axis in the *xy* plane is equivalent to two counter-rotating fields on that plane. The field following the precession drives the $\pi/2$ flip, and the field rotating in the opposite direction does so quickly enough to have a negligible effect on the spin flip (this small effect is called the Bloch-Siegert shift and is small enough to ignore for FID). It is important to note, however, that half of the $B_1$ field's strength is lost to the counter-rotating portion, so the duration of the pulse needs to be double than it would be if $B_1$ were to rotate in the plane with the precessing nuclei.

Fortunately, the homogeneity of the $B_1$ field is far less critical than the $B_0$ homogeneity. The effect of an inhomogeneous $B_1$ field on an FID experiment is minor. Source nuclei at different locations in the RF field will experience a slightly different field strength. The result is a spin flip that does not rotate the nuclei's spins by exactly $\pi/2$. This nucleus will then precess around the *z* axis, with the spin vector slightly above or slightly below the *xy* plane on the Bloch sphere. This means that when the time variation of the projection of its spin along the *x* or *y* axis is measured, contrast is lost. The particle will never be fully aligned with the measurement axis, so there will always be a probability of finding it in the opposite spin state. However, unlike inhomogeneities in the $B_0$ field, this effect is not cumulative over time. In fact, the loss of contrast is also not a particularly strong effect to begin with, since the projection onto the *x* axis will not change significantly.

Table 3.3 has the gyromagnetic ratios, $\gamma$, and precession frequencies for $^{129}$Xe and for $H_2O$ (proton) in a 1.5 mT magnetic field. The frequencies are of the order of 10s of kHz.

## 3.7 Pickup Coils

The usual method for detecting an NMR signal is through Faraday induction in a pickup coil, as the magnetic flux through the pickup coil, from the precessing nuclei changes. This method is described in Section 2.5.1. This signal is very small, however, making the dampening of noise in the pickup coils and amplification of the signal very important. The signal can be increased by making the pickup coil circuit into a resonant circuit, by adding a capacitor, which is chosen such that the circuit is resonant at the frequency of interest. This turns the pickup coil

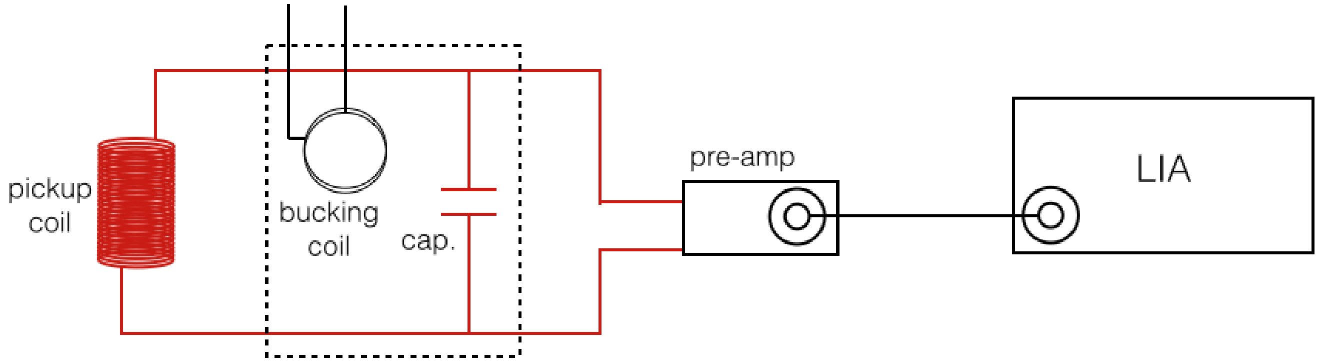


**Figure 3.12:** Here is a typical pickup coil circuit. The coil itself is at the left, and the leads go to a capacitor that tunes the circuit. The voltage across the coil is measured by a lock-in amplifier (LIA), through a pre-amp. The capacitor is usually placed in a small box to protect it from being short circuited by metal objects in the environment. A bucking coil can also be placed in this box to help cancel any cross-talk left from imperfect mechanical decoupling between the pickup and $B_1$ coils.

circuit into an LRC circuit, whose impedance will depend on the frequency of any alternating current (AC) signal driven in the pickup coil. There is a resonance $\omega_0$ at

$$\omega_0 = \frac{1}{\sqrt{LC}} \tag{3.28}$$

where $L$ is the inductance in the circuit and $C$ the capacitance. The resonant frequency does not depend on the resistance in the circuit. Tuning the circuit in this way will make any signal at the resonant frequency build up over several cycles, the same way an optical cavity builds up power circulating within it. Unwanted signals or noise at other frequencies will not build up this way, so this improves signal to noise ratio (SNR). A lock-in amplifier is also usually used to amplify the signal, which amplifies only in a narrow frequency band, and actually damps any noise at frequencies outside of this band. Such amplifiers are typically used when the signal is weak, but of a known frequency. Figure 3.12 shows a typical circuit for detecting an NMR signal.

One significant challenge comes from the fact that the $B_1$ field itself oscillates at the same frequency of the signal that is being measured. This can potentially generate an unwanted signal that is orders of magnitude stronger than the signal from the precessing particles, called cross-talk. The best way to combat this issue is to make the $B_1$ and pickup coils perpendicular to one another. This decouples the pickup coil from the $B_1$ field, since there is no field from the $B_1$ field along the pickup coil axis. Perfect alignment is never quite possible, and a leftover signal from slight misalignment must still be significant. One way this can be compensated for is by introducing a "bucking" coil to the pickup circuit that drives an electromotive force (EMF) that opposes the leftover cross-talk, which is described in more detail in Section 4.2.1.

## 3.8 Shielding and Improving Homogeneities

Externally generated RF fields at the same frequency of the precessing nuclei can be a significant source of noise in NMR experiments. If these are constant, they can theoretically be cancelled with the bucking coil, but changes in direction or amplitude of the externally generated fields cannot be easily dealt with this way. Shielding of some sort is required to improve the SNR. It is also possible to shape the DC ($B_0$) field using a shield made out of a high-$\mu$ material, with the right geometry, potentially improving the field's homogeneity.

Other techniques can also be used to improve the homogeneity of the $B_0$ field. I will describe two in this section: using shim coils and adjusting the current ratio in the main coils. In brief, shim coils are weaker sources of magnetic field that are placed strategically around the main coils to compensate for the inhomogeneities present. Adjusting the current ratio is simply a matter of having a different current go through each coil in a pair. In both cases, the magnetic field generated by the $B_0$ coils and their image fields are modified, and other external static fields can also be compensated for.

### 3.8.1 AC Shielding

One method for shielding the pickup coil from external AC fields is the use of a second coil, with fewer turns but a larger radius, or area. This can be set up in such a way that the ratio

$$N_{\text{inner}} A_{\text{inner}} = N_{\text{outer}} A_{\text{outer}} \tag{3.29}$$

holds, but with the coils wired in opposing directions. For an externally generated field, the magnetic field gradient will be small across the coils, and so the flux through both of these coils will be very similar. Since they are counter-wound, the resulting EMF will mostly cancel. This is not the case for a magnetic field generated by a small source inside the coils, such as the spin signal we are trying to measure. This field will decay on a length scale given by the source dimensions, and so the induced EMF will be weaker for the outer coil. The result is that the signal is only diminished slightly, while noise from externally generated fields is almost completely removed, improving the SNR. Increasing the radius of the outer coil compared to the inner coil (and reducing the number of windings appropriately) results in a less diminished signal, but also is less effective in canceling externally generated fields.

It is more effective, however, if the external fields can be shielded away without reducing the signal at all. This can be done with an RF shield. A shell of conductive material is placed around the coils so that external RF fields generate a current on this shell, but do not penetrate it. This works as long as the cage is sufficiently thick. The required thickness depends on the skin depth for the particular frequency of field and the material used, and also depends on the shield geometry itself. For a cylindrical shield, at a frequency and material such that the skin depth is $\delta$, and for radius $R$, the required thickness $d_0$ is[29]

$$d_0 = \delta^2/R. \tag{3.30}$$

At tens of kHz, this is significantly thinner than just the skin depth alone. This is due to Faraday induction. The shield is, effectively, a current loop, and the oscillating RF field causes a changing magnetic flux, inducing an EMF around the shield. This current generates a field that opposes the RF field, diminishing it inside the shield.

Using a shield like this has the advantage that the signal from the precessing spins is not reduced, but it can use up a lot of room in the experiment, and can make it difficult to access parts of the experiment to make adjustments.

### 3.8.2 DC Shielding

A shield made out of magnetic material, whose permeability, $\mu$, is much different than the permeability of free space, $\mu_0$, will also distort DC fields, in addition to blocking AC fields. A useful way to analyze this distortion is to expand the field in terms of a uniform field and multipoles. The effect of the shield on each multipole can be described in terms of its "reaction factor," or, the proportional change in field strength. For a saddle coil configuration, if the material is high $\mu$, such as steel or mu-metal, the reaction factor will be greater than 1, since the image currents generated are in the same direction as the actual currents. For a low $\mu$ material, such as a superconductor, the reaction factor will be less than 1, due to the negative image currents[25]. This means that the overall strength of the field is intensified with a shield made of high $\mu$ material, and diminished if made of low $\mu$ material. With the right geometry, the homogeneity of static fields inside the shield can also be improved[30].

In theory, for an infinitely long, cylindrical high-$\mu$ shield, if the coil's radius is $0.7784\times$ the shield's inner radius, the reaction factor for the uniform part of the field is maximized compared to other orders. The shield distorts the field inside, just like the optical table distorts nearby fields, but it does so in a way that is beneficial, rather than harmful to the homogeneity of the static $B_0$ field. Since the shield also reduces the strength of the field due to the $B_0$ coils outside of it, it also mitigates or eliminates the effects from nearby magnetic metals, such as the steel optical table.

The analytic results for the magnetic field generated by saddle coils can be modified to include a cylindrical shield [31].

$$R_m(k) = -\frac{I'_m(ka)K_m(kb)}{I_m(kb)} \tag{3.31}$$

if the coil radius is smaller than the inner diameter of the shield. To calculate the total resulting field, in equation 3.19, $K'_m(ka)$ is replaced with $(K'_m(ka)+R_m(k))$.

Unfortunately, for a finite length shield, with or without end caps, it is not clear exactly what the effect on the $B_0$ field would be. To avoid potentially worsening the homogeneity, it was decided not to make a high-$\mu$ shield for our setup. Instead, we used aluminum, which will block AC fields but have little effect on DC fields, having $\mu_r \approx 1$.

### 3.8.3 Shimming the Field

Shimming a magnetic field refers to the addition of weaker currents placed around the primary source of the magnetic field, or an adjustment of the current ratio between the field's primary source coils. Either method can be used to cancel a gradient in the magnetic field. This gradient can come from externally generated fields, such as the earth's magnetic field, or from field distortions of the $B_0$ field.

A simple way to shim a linear gradient in a field is to use an anti-Helmholtz pair of coils. This geometry was described in Section 3.2, and generates a linear gradient of its own. By creating a gradient that opposes the existing gradient that needs to be compensated for, a much more uniform field is generated. This method of shimming makes it easy to adjust the field gradient while having a minimal effect on the field's strength at the center, which is very useful for NMR experiments.

In the case of a saddle coil, adjusting the current ratio also generates a linear gradient. The adjustment can be made several ways. One is to build it into the coils by wrapping fewer windings on one of the coils, but there is no simple way to make further adjustments in that case. Another method is to simply run a different amount of current through each coil. This can be achieved with a variable current shunt, or by simply driving each coil with separate power supplies. This method is simpler than building a separate set of anti-Helmholtz coils, but the field's strength changes along with the homogeneity. Initially, I will use a current ratio to shim the $B_0$ field, but it may be necessary to add anti-Helmholtz coils in the future.

# Chapter 4

# Measurements and Results

In this chapter I will describe the final design of the magnetic coils that I constructed, and I will go over the results from doing nuclear magnetic resonance (NMR) experiments on protons in water, which was done to characterize the fields generated by the coils, as well as to provide a baseline for later comparisons to similar experiments on $^{129}$Xe. The data from these experiments were taken under time constraint, and so were analyzed later. From this analysis, it has become clear that there are several straightforward improvements that can be made to obtain stronger or longer lasting signals in the future.

## 4.1 Final Coil Design

The final design is shown in Fig. 4.1, which includes the AC shield, the $B_0$ and $B_1$ coils, and the $^{129}$Xe cell. The supports, mounts and optics needed for the UV enhancement cavity are also shown. The UV laser itself is behind the shield, towards the left side of the assembly, in this drawing's perspective. The NMR experiments in this chapter are performed on protons in water molecules, so the $^{129}$Xe cell is replaced with a water bottle, with a pickup coil wrapped around it. This bottle is about the same width, but shorter than the $^{129}$Xe cell. A photo of the bottom half of the AC shield and $B_0$ coil, the $B_1$ coil, and an older version of the pickup coil, meant for a wider water bottle than the one used is shown in Fig. 4.2.

### 4.1.1 AC Shield

Since the signal generated in the pickup coil is passed through a lock-in amplifier, noise at frequencies other than the precession frequency is eliminated, but noise near that frequency is amplified along with the signal. I designed an AC shield made out of aluminum to shield the pickup coil from externally generated noise sources.

This shield is 2 m long, and has a radius of 220 mm. The aluminum itself is about an eighth of an inch thick, and was rolled into a cylinder by the the University of British Columbia (UBC) machine shop. Our shop is only able to roll pieces that are up to about 3 feet wide, due to the size of the rollers, so the shield was made in 4 parts, which were riveted together. Since we are doing NMR at low magnetic field strengths, the frequencies that we are interested in are quite low, only tens of kilohertz, which correspond to wavelengths in the tens of kilometers. This means that holes in the shield should not diminish its effectiveness. Some holes in the shield are needed to pass wiring to the coils and UV cavity electronics, and to let the UV laser light in. The shield is also cut in half down the

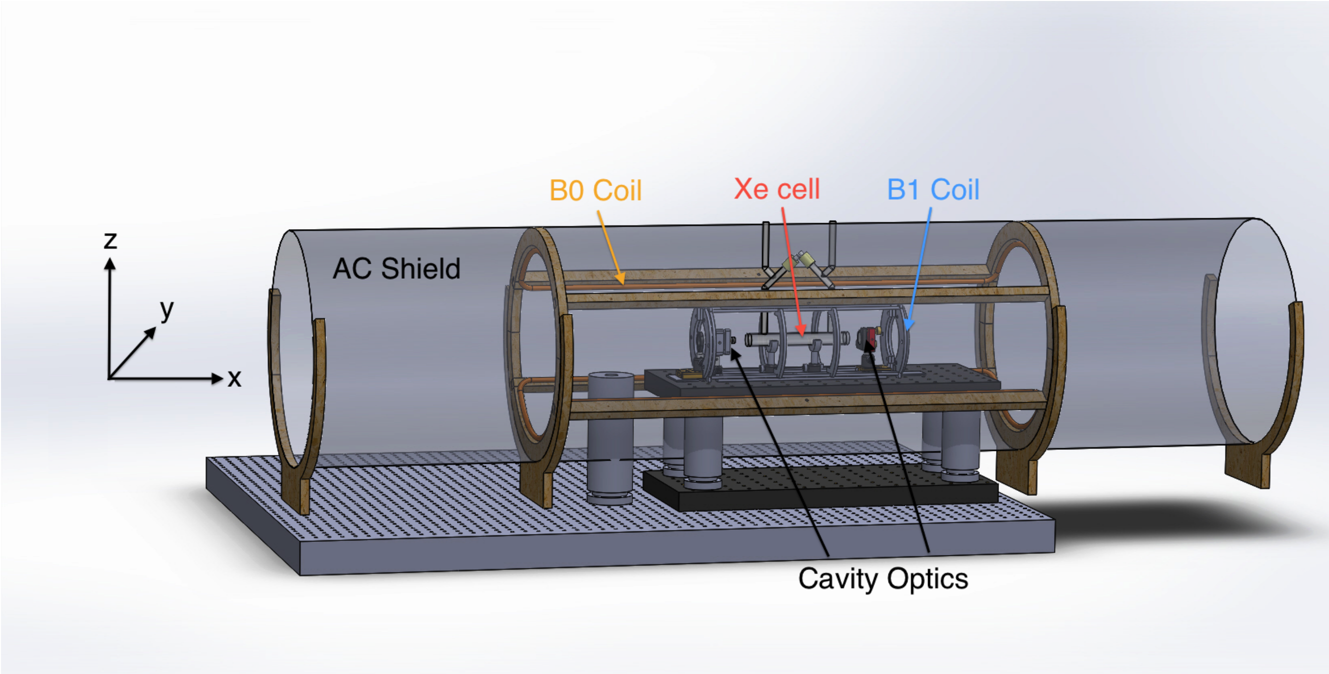


**Figure 4.1:** The full assembly of coils and the $^{129}$Xe cell, and cavity optics. The cell has a pickup coil wrapped around it. The water bottle used to make the measurements in this chapter is about the same width, but is shorter than the $^{129}$Xe cell. The AC shield is also shown, as well as the mounts used to hold that shield in place. The $B_0$ coils are mounted to a wooden frame that attaches to the shield, and the $B_1$ coil is mounted on an acrylic frame. Holes are cut in the shield to accommodate the aluminum pillars that hold up the slab for mounting the $B_1$ coil, cell, and cavity optics. The UV laser's output is behind the shield towards the left side of this assembly. As shown, the $z$ axis points up in this figure, and the $x$ axis down the shield. The $y$ axis is also in the transverse plane, such that the coordinate system is right handed. The origin is taken to be the center of the $^{129}$Xe cell.

long axis, so that the top half can be easily removed for access to the UV cavity, the $B_1$ coil, and the pickup coil. The top half mounts to the bottom half with brass screws and a strip of aluminum.

Mechanical stability is extremely important for the UV cavity to function, but the cavity needs to be at the center of the magnetic fields, so it needs to be raised above the optical table. A heavy, nonmagnetic platform, with threaded brass inserts is raised up on aluminum columns and glued into place with epoxy to use as a platform for the cavity as well as the $B_1$ and pickup coils. The lower half of the shield has holes drilled to accommodate these columns, and is mounted on wooden mounts before the platform is epoxied. The columns are secured to the optical table with aluminum clamps.

### 4.1.2 B0 Coil

The $B_0$ coil design was motivated by the need for a very homogeneous magnetic field, and like described in Chapter 3, a saddle coil geometry is ideal for creating a uniform field across the size and shape of the $^{129}$Xe cell. The exact coil parameters also need to take into account the distorting effects from the high-$\mu_r$ steel optical table. The final $B_0$ coil design has 20 windings of 14 gauge wire wrapped in a saddle shape with rungs 1 m long, and arcs with a radius

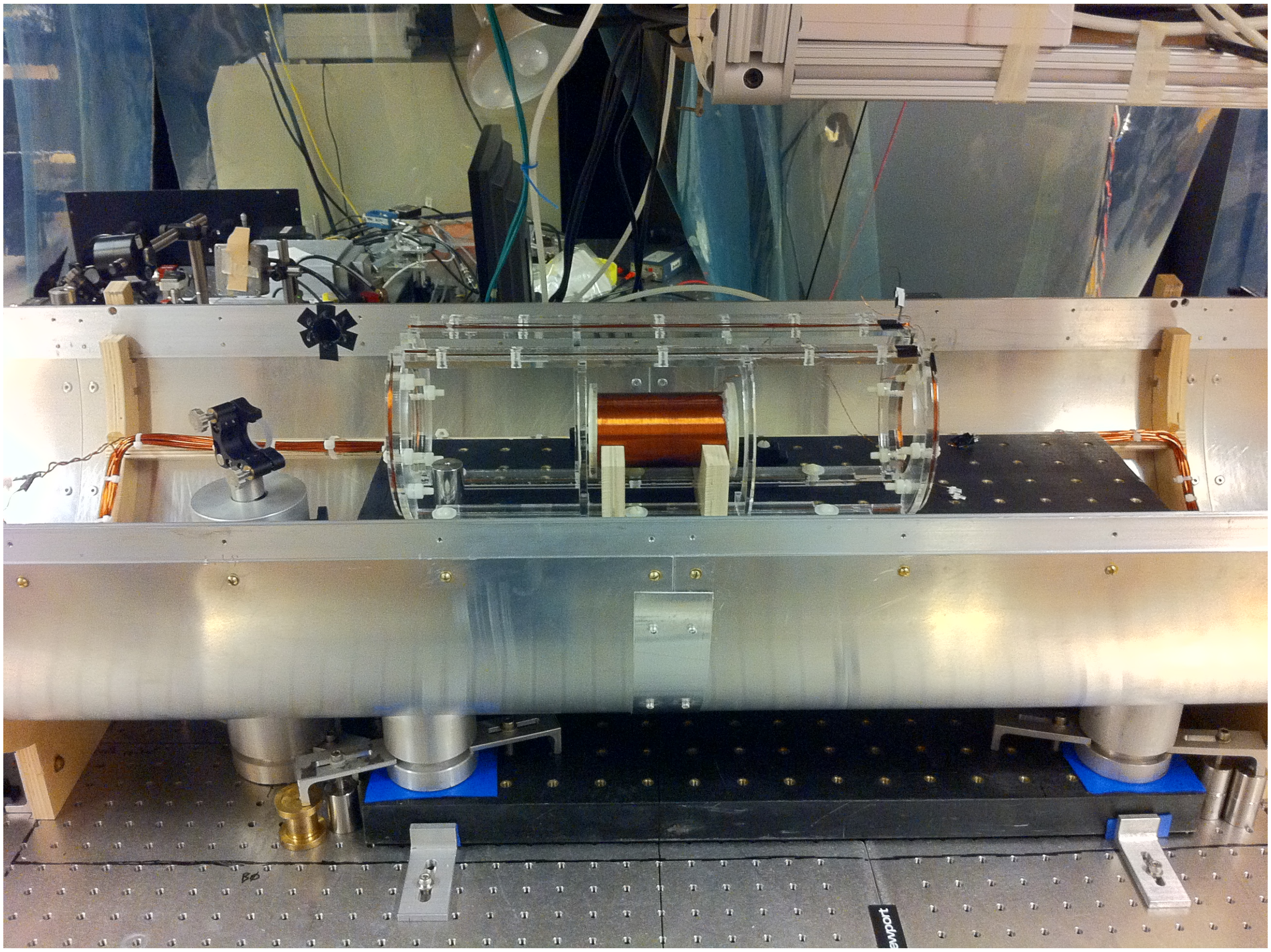

**Figure 4.2:** A photo of the shield, the bottom of the $B_0$ coil, the $B_1$ coil, and an older version of the pickup coil, meant for a wider water bottle than the one used. On the left side there is a mirror that is used to guide the UV laser light to the UV enhancement cavity, which is removed in this photo. The top half of the shield also holds the top half of the $B_0$ coil.

of 180 mm and a span of 120° that generate a field along the $z$ axis. The $B_0$ coils were wrapped around a purpose built wooden frame, then lifted off and mounted to the inside of the AC shield. Part of the bottom half can be seen in Fig. 4.2.

The strength of the field that the coils can generate is limited by the heating of the wire as the current through them is increased. In principle, the current can be increased until either the insulation breaks down and the wire shorts, or until the copper itself melts, but there are other potential problems as the wire temperature increases. The resistance in the wire is dependent on its temperature, so when using a voltage source, such as the power supply we used, the current drifts as the wire approaches the equilibrium temperature. With the AC shield, this heat gets trapped, warming the pickup and $B_1$ coils as well. It is also sometimes necessary to reach into the shield, so there are safety concerns with the wires getting too hot. This coil starts becoming painful to the touch at about 10 A. For these experiments, this limit is not of consequence, since the power supply being used to drive the $B_0$ coil

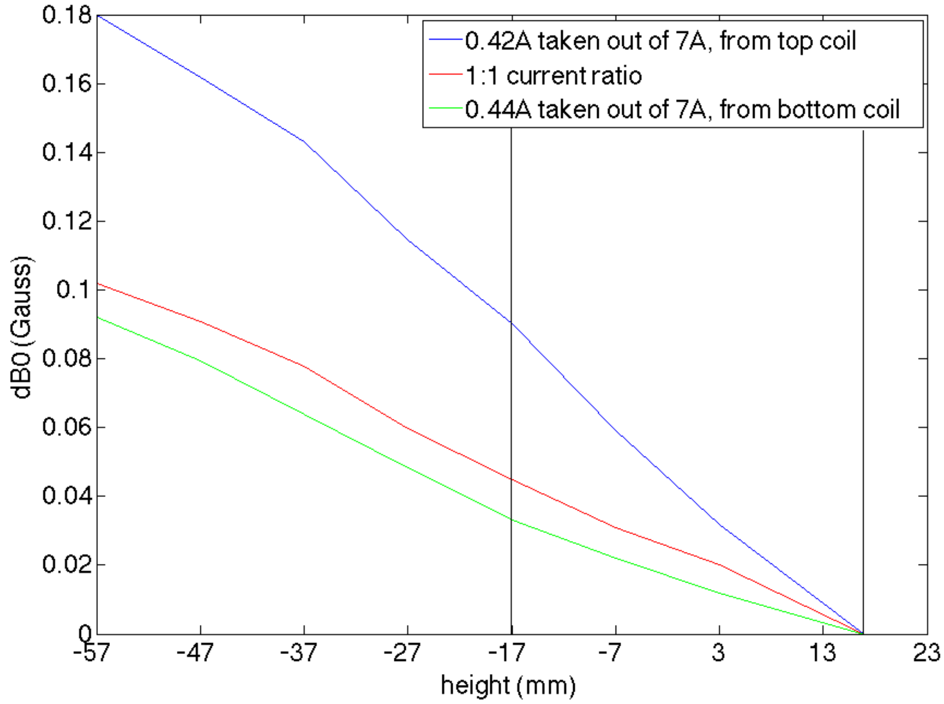


**Figure 4.3:** This is a plot of the $B_0$ field homogeneity measurement along the $z$ axis. The field strength is normalized to 0 at the top of the water bottle. The vertical extent of the water bottle is shown by the black lines, at about -17 mm and +17 mm. The height is zeroed at the cell center. The blue plot is what the experiments in this chapter were performed under, with about 0.42 A taken from the top coil. The variation of the magnetic field strength along the $z$ axis is about 0.1 Gauss (10$\mu$T), or about 1.5% of the magnitude of the magnetic field. Removing the potentiometer, or moving it to the lower coil improves the field homogeneity.

cannot drive more than 8A. It is usually set to about 7 A for the experiments in this chapter, since the adiabatic fast passage (AFP) experiments require ramping this current up and down around its set point. It takes about an hour for the temperature inside the shield to stabilize after turning on the $B_0$ coil.

The field generated by the $B_0$ coils in the cell region was measured with a flux gate. The direct current (DC) field generated by these coils, when placed above the steel optical table, with no compensation for the gradient it creates in the field, was measured to be 0.943 G/A (94.3 $\mu$T/A) at their center. The field gradient along the $z$ axis was also measured, which can be compensated for by adjusting the current ratio between the top and bottom coils. This adjustment is currently done by connecting a potentiometer in parallel with one of the coils, to divert some current away from that coil. Since the flux gate was borrowed from another group, I ended up having to make these measurements after the experiments in this thesis had already been performed, so the current ratio was set based on the simulations described in Chapter 3. However, I mistakenly connected the potentiometer to the top coil rather than the bottom coil, and actually made the gradient worse. Figure 4.3 shows the field gradient in the $z$ direction for various current ratios. The black vertical lines are at the water bottle's walls, so the field inhomogeneity for the experiments in this chapter should be about 0.1 G, or 10 $\mu$T.

The $B_0$ coil circuit consists of a power supply, the coils, and a current stealer circuit attached in parallel to one of the coils. The power supply also has a control input, where a ramped signal is sent for AFP, which is controlled by a function generator.

### 4.1.3 B1 Coil

The $B_1$ coil generates the radio frequency (RF) field that flips the nuclei's spins. This field is generated by another saddle coil, and points perpendicular to the $B_0$ field, along the $y$ axis. The homogeneity of the $B_1$ field is not nearly as critical as the $B_0$ field, so it can be made much smaller, physically. This $B_1$ coil is made of 10 windings of 26 gauge wire in a saddle shape with rungs 400 mm long, and arcs with a 75 mm radius, and a span of 135°, wrapped around an acrylic frame. The coil can be seen in the photograph, Fig. 4.2.

For a DC field, the $B_1$ coils produce about 1 G/A, measured with a gaussmeter. In principle, for AC fields, this might be attenuated somewhat by the presence of the aluminum shielding. This attenuation should be weak, since the shield radius is considerably larger than the coil radius. Measuring the AC field is not possible with the measurement devices we had in the lab, unfortunately. This matters the most when doing free induction decay (FID), since the field strength determines how long the $\pi/2$ pulse needs to be on. It will also affect the adiabaticity condition for AFP. The best test available to us is to simply do FID repeatedly with different currents or pulse durations, to find the maximum signal amplitude from FID.

The $B_1$ coil circuit consists of a function generator which drives the AC current, the coil itself, and a 1 Ω power resistor that is used to monitor the current in the coil.

### 4.1.4 Pickup Coil

The pickup coil measures the changing magnetic flux from precessing spins. By Faraday induction, an electromotive force (EMF) is induced, the current from which generates a magnetic field that tries to oppose an external change in magnetic field. This coil can be easily replaced with a different one in the setup, and is usually matched to the sample container. For example, for the proton NMR experiments done in this section, the coil is wrapped directly around the water bottle used to hold the sample. This maximizes the signal from precession, while minimizing noise from other oscillating fields. The EMF generated in the pickup coil is very small (on the order of a $\mu$V or less in these experiments), so the current in the wires is tiny, and they can be quite thin without worrying about thermal damage. The pickup coil used was wound from 26 gauge wire, and has 190 windings, in a solenoid configuration.

The pickup coil is inductive, of course, so rather than connecting it directly to the amplification circuit, a resonant circuit can be made by adding a capacitor. This is done in an external box (the "tuning box"), so that it is easy to change the tuning capacitor if the pickup coil is changed. The capacitor needs to be chosen appropriately to create a resonant circuit at the correct frequency. The resonant frequency of the circuit is given by

$$\omega = \frac{1}{\sqrt{LC}}, \tag{4.1}$$

where $L$ is the inductance of the pickup coil and $C$ the capacitance of the tuning capacitor.

The pickup coil used will depend on the sample, so its inductance $L$ needs to be measured, and then a tuning box with the correct capacitor needs to be made for each pickup coil. The desired precession frequency also needs to be known, so that the circuit's resonant frequency, $\omega$ can be made to match. After a capacitor has been chosen, the

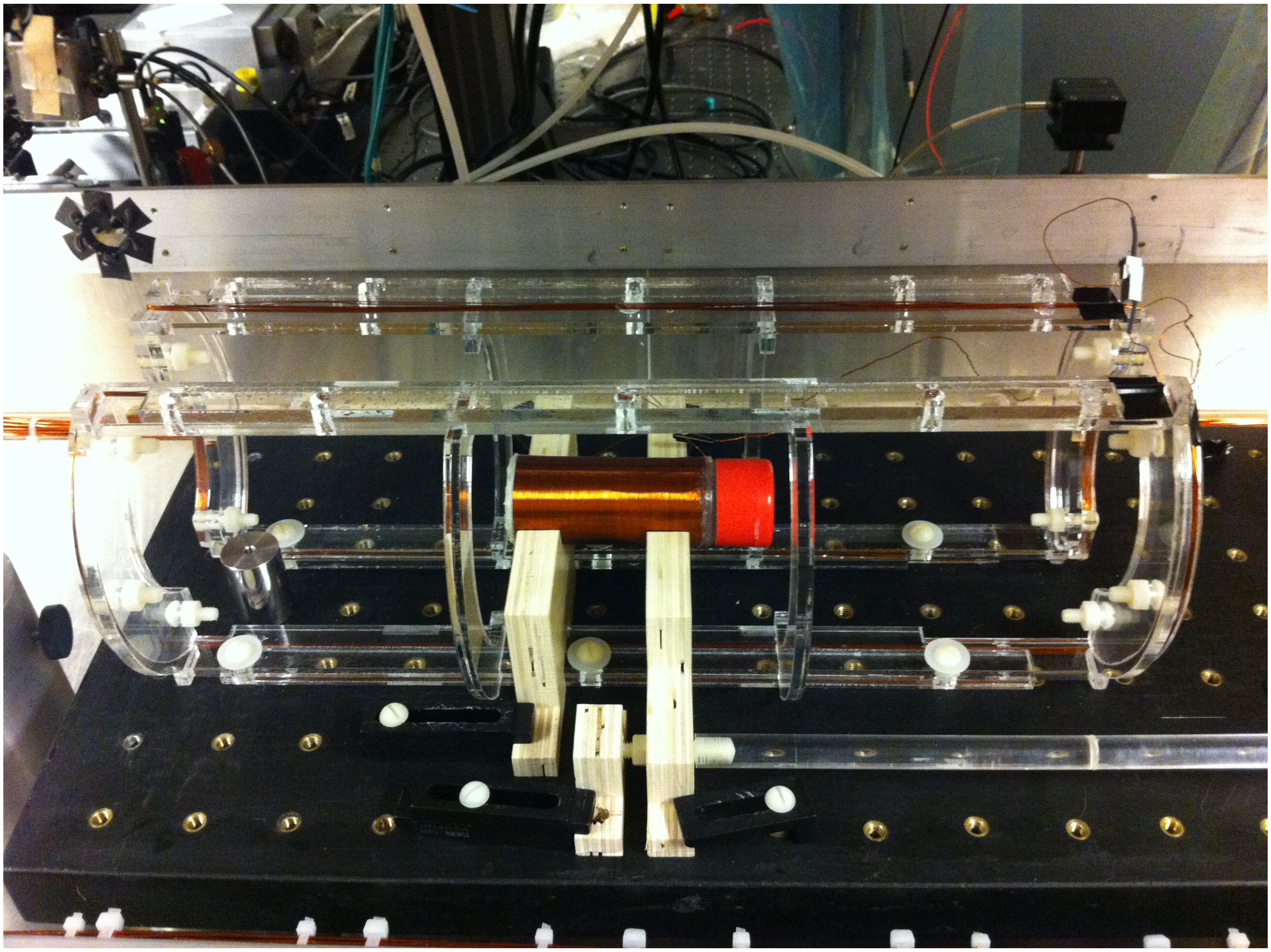

**Figure 4.4:** This is a closeup photo of the pickup coil, wrapped around the water bottle used for these experiments. Rotating the plastic rod at the bottom of the photo changes the alignment between the pickup and $B_1$ coils, to mechanically decouple them and reduce cross-talk. The $B_1$ coil can also be seen, mounted to an acrylic frame. In the back left, there is a hole in the shield to allow the UV laser light in. It is wrapped in black tape to protect wires from sharp edges, since the insulation on the wires used to make the coils is very thin.

actual resonant frequency needs to be measured since tolerances on components, and other inductive and capacitive circuit elements can shift this frequency. The easiest way to measure the resonance of the pickup coil circuit is simply to measure the cross-talk from the $B_1$ coil with the lock-in amplifier. Since this amplifier also drives the $B_1$ coil, changing the frequency on the amplifier changes both the signal in the pickup coil, and the frequency that is measured by the amplifier. The resonant frequency is the frequency where the cross-talk is maximized. For these experiments, the pickup coil's inductance was measured to be 454 $\mu$H. We wanted a precession frequency of around 27 kHz for the protons in our NMR experiment, since that corresponds to about 7 A on the $B_0$ coils, so a capacitor of 76 nF would tune the circuit. The measured resonance with such a capacitor was at 27.07 kHz, so this is the frequency that is used for all of the experiments in this chapter.

For the actual NMR measurements, cross-talk is not desirable, so the pickup coil's angle to the $B_1$ coil can be adjusted. The corner of one of the mounts can be moved around to change the horizontal angle of the container compared to the $B_1$ coil by rotating a threaded rod. This is usually good enough to bring the cross-talk down to about 15 mV before the lock-in amplifier (but after the pre-amp), which has been sufficient for these experiments. Figure 4.4 shows a closeup view of the pickup coil, water bottle, $B_1$ coil and the decoupling mechanism.

The pickup coil circuit consists of the pickup coil and a tuning capacitor. The output is sent to a 100x pre-amp and then into the lock-in amplifier.

### 4.1.5 Lock-in Amplifier

All of the NMR measurements taken in this chapter were done through a lock-in amplifier, which is commonly used when a signal is of a constant, known frequency. They are somewhat different than traditional amplifiers in that they amplify a signal from a specific frequency, while damping any signal or noise at other frequencies. This is done by multiplying the signal by the reference sine wave, and integrating over some time. If the signal being sent to the lock-in amplifier is $A\sin(\omega t)$, and the amplifier's reference frequency is $\omega_{lia}$, then the output depends on the integration time, and the phase between the signal and reference, $\phi_{lia}$:

$$V_{\text{out}}(t') = \int_0^{t'} V_{in}(t)\sin(\omega t)\sin(\omega_{lia}t + \phi_{lia})\mathrm{d}t. \tag{4.2}$$

The output's amplitude diminishes as $\omega$ gets further from $\omega_{lia}$, and does so more rapidly when $t'$ is longer. In the limit where one integrates over all time, so $t' \to \infty$, then the only contribution to the signal is from sources at *exactly* the reference frequency. For finite integration times, this multiplication creates a bandpass filter, with the width increasing for shorter integrations. That means that there is potentially more noise left in the amplified signal when set to a shorter time constant. However, if the signal changes quickly in amplitude, like FID does when the field inhomogeneity is too high, a short time constant is required so that this signal does not get averaged out. This averaging can also make measurements slightly inaccurate. For example, the height of a peak during AFP will become smaller due to this averaging when going to long integration times. The positions of features will also be delayed a bit, which needs to be taken into account when comparing to other simultaneous measurements. These inaccuracies increase as the integration time increases. To compensate for the lost signal to noise ratio (SNR) by going to short integration times, many data runs can be taken and averaged together.

The amplified signal's amplitude also depends on the phase between the raw signal and the reference sine wave used by the lock-in amplifier, $\phi_{lia}$. When they are out of phase, the strength of the output signal will be diminished, going to 0 when the two sine waves are 90° out of phase. The lock-in amplifier I used has two outputs, with the reference frequency for each being out of phase with each other by 90°, called "*x*" and "*y*." The *y* output is determined by equation 4.2, but with $\phi_{lia}$ replaced with $\phi_{lia} + 90°$. With the outputs phased in this way, the true amplitude of the amplified signal can be obtained by adding them in quadrature.

The lock-in amplifier also has a variable setting for the amount of amplification. This is labeled as "sensitivity," since it sets the input range. The output is always -10 V to +10 V, so if the sensitivity is set to 5 mV, for example, there is 2000x amplification. There is also a pre-amp which has a frequency independent amplification of 100x. The output from the lock-in amplifier is sent to an oscilloscope to read and save the measurement data.

## 4.2 Adiabatic Fast Passage (AFP)

The first experiments performed with these coils was AFP on protons in water molecules. Since the experiment is run on a Boltzmann polarized[1] sample, there is a known and repeatable polarization. This is convenient because this way a lack of signal cannot be due to insufficient polarization, and indeed, it was quite simple to find an AFP signal by scanning the $B_0$ field, and so the precession frequency, over a large range. Having such a repeatable polarization also makes it easy to average many runs to improve SNR. This allows us to dramatically reduce the integration time on the lock-in amplifier to get a more accurate signal. By varying the parameters used in the AFP experiments, it is possible to begin characterizing the coils and the fields they produce. This characterization is continued with FID in Section 4.3.

AFP was described in detail in Section 2.6, but I will go over it again briefly here. The oscillating $B_1$ field is left on constantly, and the $B_0$ field is ramped slowly. As the $B_0$ field is ramped, the precession frequency of the nuclei changes. As the precession frequency ramps through the $B_1$ frequency, the spins of the nuclei are adiabatically transferred to the opposite $z$ state as they were originally. As they are transferred, they spiral through the transverse plane and induce an EMF in the pickup coils. Figure 4.5 shows an example of what signals are monitored on the oscilloscope during an AFP measurement. The resonant frequency of the pickup coil circuit is 27.07 kHz, and for protons to precess at that frequency, a $B_0$ field of 0.636 mT (6.36 G) is required. A current of just under 7 A generates this field strength, using these coils.

The power supply being used has a tuning input, so to ramp the field, a ramped input from a function generator can be used. The lock-in amplifier and the $B_1$ frequency need to be exactly the same, which is accomplished most easily by using the lock-in amplifier's reference sin wave itself as a source for the $B_1$ current. One additional function generator needs to be used to drive the bucking coil that cancels residual cross-talk, the details of which are described in Section 4.2.1. The entire circuitry and the equipment used is shown in Fig. 4.6. For the pickup coil, the tuning capacitor is placed in a tuning box to make it easy to swap out for a different one. Conveniently, the bucking coil can also be placed in this box. The pre-amp amplifies the signal by 100x and outputs the amplified difference in voltage between the two leads of the pickup coil circuit. This signal is passed to the lock-in amplifier. The current through the $B_1$ coil is measured by measuring the voltage across a 1 $\Omega$ power resistor on the grounded side of the circuit.

### 4.2.1 Cross-talk

Cross-talk is a significant spurious signal that prevents us from being able to go to lower sensitivity on the lock-in amplifier. In this case, it refers to any signal that is generated in the pickup coil by the oscillation $B_1$ field. So, to maximize SNR, it is important to minimize cross-talk. Other than the mechanical decoupling described in Section 4.1.4, a "bucking" coil is used to drive a current in the pickup coil circuit that is exactly out of phase with the cross-talk when doing AFP. The resulting destructive interference can reduce the cross-talk by several orders of magnitude. Empirically, we did notice that the noise in the signal increases if the bucking coil needs to do more work, however, so the mechanical decoupling still needs to be as good as possible. A good goal for the mechanical decoupling is to get under 15 mV after the pre-amp.

After mechanically decoupling the coils as well as possible, the voltage of the remaining cross-talk is noted

[1] see Section 2.3.1 for a description of Boltzmann polarization

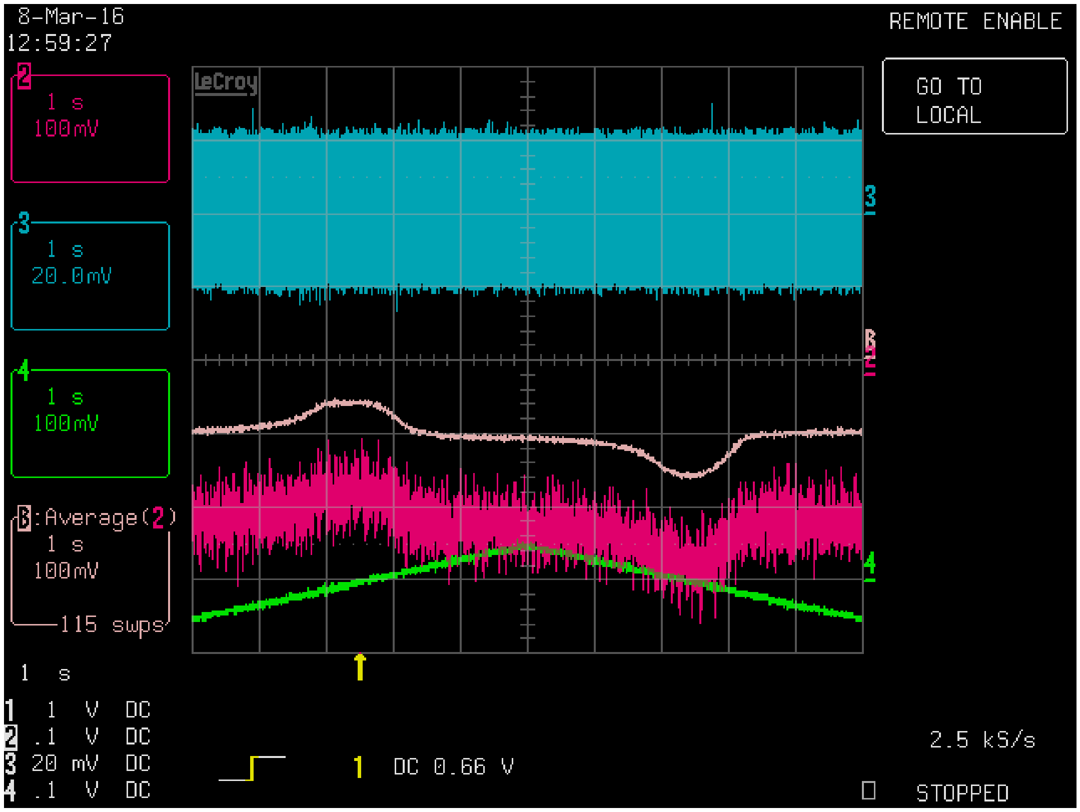


**Figure 4.5:** Here is a sample screenshot of the oscilloscope while performing AFP. The green plot measures signal sent to the power supply for the $B_0$ ramp. The noisy magenta plot is the EMF generated in the pickup coil, de-modulated and amplified by the lock-in amplifier. The light pink plot above that is an average of 115 sweeps of the magenta plot. The blue plot is the current through the $B_1$ coil, and oscillates at 27.07 kHz. At longer time constants, the SNR straight out of the lock-in amplifier is similar to the averaged signal here. The magenta plot was taken with a time constant of 1 ms, and at a time constant of 100 ms, the data look similar to the light pink plot.

and then the $B_1$ coil is turned off. The bucking coil is then turned on and its amplitude is adjusted until the signal through the lock-in amplifier matches that of the cross-talk. Then, the $B_1$ coil is turned back on, and the phase on the bucking coil is adjusted until the cross-talk is minimized. The amplitude and phase of the current through the bucking coil often needs to be adjusted again after the $B_0$ coil has reached thermal equilibrium.

### 4.2.2 AFP results

Most of these AFP experiments were performed with the lock-in amplifier at a 5mV sensitivity (which corresponds to a 2000x amplification, plus an additional 100x from the pre-amp), 1 ms time constant, and 24 dB slope[2]. I performed AFP on protons in water while varying a number of parameters. The goal was to determine the $T_1$ time constant and to confirm the adiabaticity conditions for water for these coils, and so also confirm the $B_1$ field strength. From the width of the AFP signals, it would also be theoretically possible to determine the $B_0$ field gradient, and

[2]The slope here refers to how steep the edges of the bandpass filter are in frequency space. A 24 dB slope is the steepest setting on this lock-in amplifier.

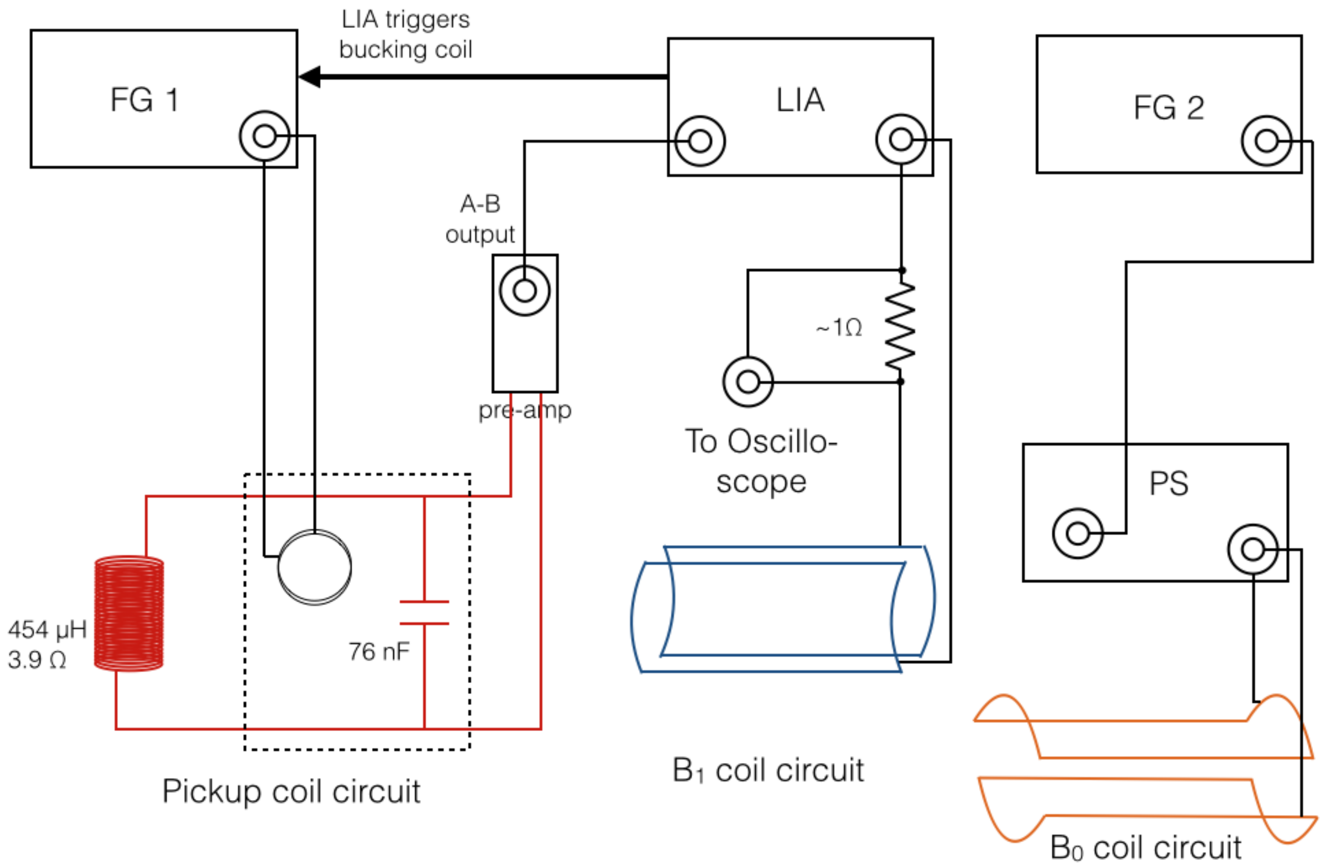


**Figure 4.6:** Here is a schematic of how the function generators and circuits are hooked up for AFP. On the left is the pickup coil circuit. FG1, the first function generator, drives the bucking coil, which is placed inside the tuning box (shown as the dashed box around the tuning capacitor and bucking coil). The coil needs to maintain phase with the $B_1$ coil, but since they are driven by separate devices, this is not guaranteed. To ensure phase, FG1 is actually run in burst mode, triggered by the lock-in amplifier. The voltage across the pickup coil is measured by the LIA, after a 100x pre-amp. The amplifier demodulates the signal, and also drives the $B_1$ coil at the same frequency as this demodulation. A 1 Ohm power resistor is placed in the $B_1$ circuit, and is used to measure the current through this circuit. A second function generator, FG2, drives the ramp on the power supply, PS, which drives the necessary current through the $B_0$ coil. This circuit is completely separate from the pickup and $B_1$ circuits.

from there the $T_2^*$ time, although FID is better suited for that measurement, since there are a lot of factors that can affect the width of the AFP signal that would all need to be carefully accounted for.

When performing AFP, it is important to make sure that the ramp rate is not too fast, or the spins will not follow the field adiabatically, reducing the amplitude of the AFP peak. The condition for adiabaticity is

$$\frac{dB_0}{dt} << \gamma B_1^2. \tag{4.3}$$

With the $B_0$ ramp rate at 4.1 $\mu$T/s, $B_1$ should be much greater than 0.3 $\mu$T. This can be confirmed by repeating AFP measurements for varying strengths of $B_1$. As the $B_1$ field becomes weaker, the chance that a given nucleus transfers to the new spin state decreases.

The probability that a nucleus' spin is *not* transferred to the new spin state is[32]:

$$P_{\text{lost}} = \mathrm{e}^{-\frac{\pi}{2}\frac{\Omega^2}{\partial\delta/\partial t}}, \tag{4.4}$$

where $\Omega$ is the precession frequency of the nucleus, in rad/s, around the $B_1$ field (*not* the $B_0$ field), and $\partial\delta/\partial t$ is the ramp rate of the precession frequency around the $B_0$ field, in rad/s$^2$.

By varying the strength of $B_1$, $\Omega$ is varied:

$$\Omega(B) = \gamma B_1(I) = 2\pi * 42.576 * 10^6 * B_1(I), \tag{4.5}$$

where $B_1(I) = c * I$, some constant times the current. Based on measurements performed with a gaussmeter, $c = 97 \pm 4$ $\mu$T/A.

The $B_0$ ramp rate for this experiment was kept constant at 4.1 $\mu$T/s, so

$$\frac{\partial\delta}{\partial t} = 4.1 * 10^{-6} * 2\pi * 42.576 * 10^6 = 1096.8 \text{ rad/s}^2 \tag{4.6}$$

is the ramp rate in the proper units for equation 4.4.

The data that is obtained by varying the $B_1$ field strength does not give the probability of losing polarization, though, it is the polarization that remains. So, the equation that I fit to is

$$P_{\text{remaining}} = A * (1 - \mathrm{e}^{-\frac{\pi}{2}\frac{(2\pi*42.576*10^6*c*I)^2}{1096.8}}). \tag{4.7}$$

Here, I multiply the whole equation by a scaling factor, $A$, since the data are not normalized. The fit parameter is $c$, the field strength per amp through the $B_1$ coils.

The result from the fit is shown in Fig. 4.7, and was found to be $c = 10.9 \pm 0.3$ $\mu$T/A, almost a full order of magnitude lower than what was measured with the gaussmeter at DC, $c = 97 \pm 4$ $\mu$T/A. It is possible that the attenuation from the shield is greater than expected, but more likely that one of the measurements, either the DC field per amp, or the data and its fit, are incorrect. Since the shield's diameter is about 3x that of the $B_1$ coils, the expected attenuation is approximately $1/3^2$, so the reduction should be by about 11%, rather than the 89% difference found here, between the DC measurement and the result from the fit. [30] Looking back at the adiabaticity condition as well, equation 4.3, for this ramp rate, $B_1$ needs to be much greater than 0.3 $\mu$T. According to the fit, with $c = 10.9$ $\mu$T/A, this condition would correspond to a $B_1$ current of much greater than 27 mA. The gaussmeter measurement, with $c = 97$ $\mu$T/A, would put the condition on the current at much greater than 3 mA for adiabaticity. From Fig. 4.7, it can be seen that at a $B_1$ current of 27 mA, AFP appears to already be adiabatic since the peak heights have reached their maximum. So, it seems likely that the gaussmeter measurement is more accurate. This inconsistency has potential implications for FID experiments as well, since the strength of the $B_1$ field needs to be known so that the duration can be set properly. A method for directly measuring the field strength per amp at 27.07 kHz may be required.

The other parameter I varied was the time between AFP peaks. After each AFP peak, the sample will return to Boltzmann polarization on the $T_1$ time scale, but if another AFP ramp happens before this relaxation is complete, a spin flip still occurs. However, the signal from this flip will be somewhat out of phase with the lock-in amplifier's reference sin wave. Figure 4.8 shows an example of two AFP spin flips that begin with a sample polarized in the

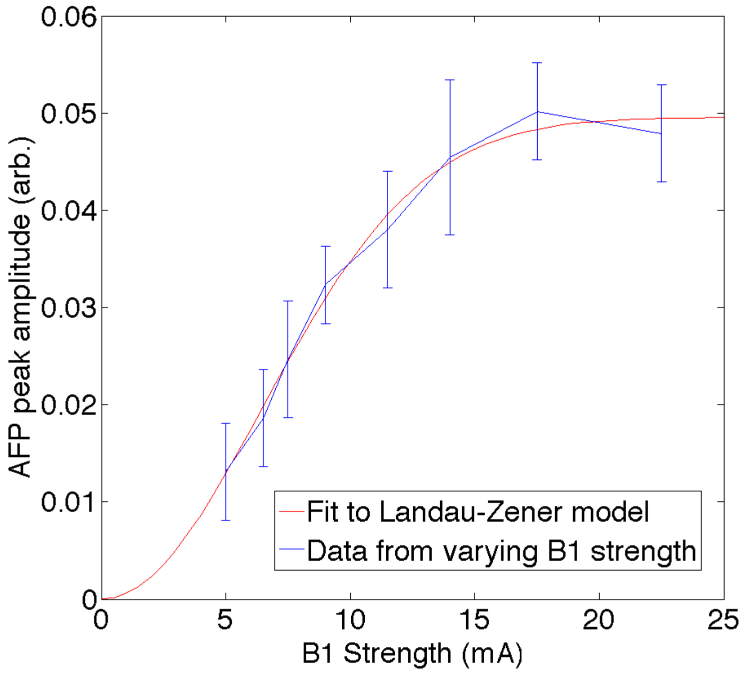


**Figure 4.7:** This is the data obtained by varying the $B_1$ field strength. The data in blue is the height of the AFP peak at that field strength, and the red line is a fit to the Landau-Zener model. This model states that the probability of a spin *not* transferring to new spin state is given by $P = e^{\frac{\pi}{2}\frac{\Omega^2}{\partial\delta/\partial t}}$, where$\partial\delta/\partial t$ is the rate at which the precession frequency of the protons is ramped, and $\Omega = 2\pi\gamma c I$, with $\gamma = 42.576$ MHz/T, $I$ being the current through the coils, and $c$ being the fit parameter; the strength of the $B_1$ field per amp of current through it. The fit found $c = 10.9 \pm 0.3$ $\mu$T/A, almost a full order of magnitude lower than what was found by measuring the DC field produced by a known current with a gaussmeter.

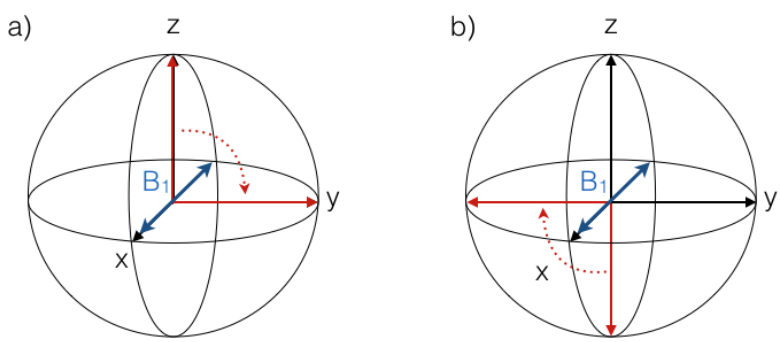


**Figure 4.8:** The phase of the signal from AFP depends on the direction of initial polarization of the sample. Shown here is a portion of the spin flip during AFP, in the rotating frame for simplicity. In panel a), the spin is initially up along the $z$ axis, and halfway through the spin flip, points in the positive $y$ direction. In panel b), the spin is initially *down* along the $z$ axis, and points in the *negative* $y$ direction during the spin flip. The two examples are 180° out of phase with each other, and so is the signal they generate in the pickup coils.

up state in $z$, panel a), and a sample polarized in the down state, panel b). In this example, the signals generated by each of the spin flips are out of phase with each other by 180 °. For this experiment, the lock-in amplifier's phase is set to maximize the signal amplitude out of the "$x$" output for one of the AFP peaks. As long as the time before the next AFP peak is not large compared to the $T_1$ time of the sample, the AFP signal from the next ramp through the resonance will be out of phase with the first, which will result in a smaller peak, or even a negative peak in the "$x$" output.

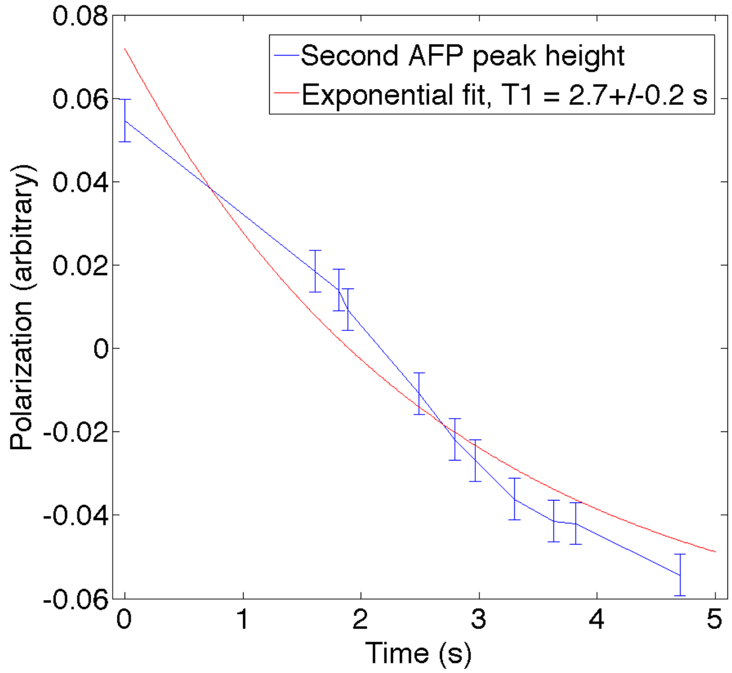


**Figure 4.9:** This is a plot of the heights of the second AFP peaks (the first data point is the initial peak), when the time between peaks is scanned. An exponential decay is fit to these points, where the polarization is $A(1-2\mathrm{e}^{-t/T_1})$. $T_1$ is found to be 2.7±0.2 seconds.

The experiment is repeated, for varying times between AFP peaks, and the height of the second peak is recorded each time. These peak heights can be fit to an exponential decay. The fit equation is found by examining exactly how the polarization behaves after the initial AFP spin flip.

After the first AFP ramp, the nuclei end up polarized in the opposite spin state from Boltzmann equilibrium. The $z$ polarization (or, magnetization) then changes like:

$$M_z(t) = M_{z,\,\mathrm{eq}}(1-2\mathrm{e}^{-t/T_1}), \tag{4.8}$$

where $M_{z,\,\mathrm{eq}}$ is the Boltzmann polarization. In this case, $M_z(0)$ is the polarization at the end of the first spin flip. Over time, the polarization returns to equilibrium (Boltzmann polarization), until the second AFP spin flip is applied, at time $t = t_2$. The phase of the signal generated during this second spin flip compared to the phase of the first flip is

$$\phi = \mathrm{acos}\left(\frac{M_z(t_2)}{M_{z,\,\mathrm{eq}}}\right). \tag{4.9}$$

The relative amplitude of the signal in the "$x$" output of the lock-in amplifier will depend on this phase:

$$\frac{V_2}{V_1} = \cos\phi, \tag{4.10}$$

where $V_1$ is the amplitude of the signal from the first AFP peak, and $V_2$ the amplitude from the second. The three equations 4.8, 4.9, and 4.10 can be combined to arrive at the equation the data should be fit to:

$$V_2 = V_1(1 - 2e^{-t/T_1}). \tag{4.11}$$

This equation is fit to the peak heights (including also the initial peak height, where $t$=0, as the first data point), which is shown in Fig. 4.9. The result of the fit is a $T_1$ time of 2.7±0.2 seconds.

## 4.3 Free Induction Decay (FID)

FID was described in detail in Section 2.7, but I will briefly go over it again here. The spins of a sample that is initially polarized along the $B_0$ field direction are tipped into the transverse plane by a $\pi/2$ pulse from the $B_1$ coils. The sample is then allowed to precess freely around the $B_0$ field. The transverse polarization will disappear over time due to relaxation effects and the $B_0$ field gradient, so the EMF induced in the pickup coil decays exponentially.

For a number of reasons, finding an FID signal is usually more challenging than performing AFP. In principle, the initial signal strength should be the same as the amplitude of the AFP peaks, since in both cases the spins are at their maximum transverse polarization. However, if the FID experiment's $B_1$ pulse is not well tuned, it will not tip the spins by exactly $\pi/2$. In that case, the transverse polarization will not be as strong as it could be, diminishing the initial signal. Measuring the $B_1$ field at its operating frequency is not possible with the equipment in our lab, so it must be estimated. I measured the field strength per amp for a DC field, and found it to be 0.97±0.04 G/A. For the first attempts at FID, I assumed that there would be a negligible difference to the field strength at 27.07 kHz. The presence of the aluminum shield could introduce a frequency dependent attenuation, however. To determine the optimum $B_1$ pulse duration, FID can be repeated while varying the duration or strength of the $B_1$ pulse, looking for the maximum FID signal strength. Cross-talk poses a larger problem than for AFP, since even with a bucking coil, the ring down in the resonant pickup coil circuit of the $B_1$ coil's cross-talk after the $B_1$ pulse turns off is an exponentially decaying signal, just like the FID signal we are looking for. It is mitigated by using a Q-killing resistor, instead, described in detail in Section 4.3.1.

The $B_0$ field needs to be precisely calibrated such that the nuclei precess at the same frequency as the $B_1$ frequency. One of the easiest ways to do so is to perform AFP first, and adjust the center of the $B_0$ ramp such that the AFP peaks are precisely centered. When the ramp is turned off, the field should be sitting exactly on resonance. Care must be taken, however, since the lock-in amplifier's time constant results in a slight time delay of the AFP peaks, due to the averaging it does. This manifests itself as an error in the exact current that resonance occurs, and is seen as an asymmetric positioning of the peaks on the up and down ramps. The time constant should be reduced until this shift is negligible compared to the width of the AFP peaks. Generally, a time constant of a few ms has worked for this purpose in these experiments.

Cross-talk is not completely eliminated, so to make sure that any signal I find is actually from FID, I first took data with the nuclei precession on resonance with the $B_1$ field, and then again with them far off resonance. These

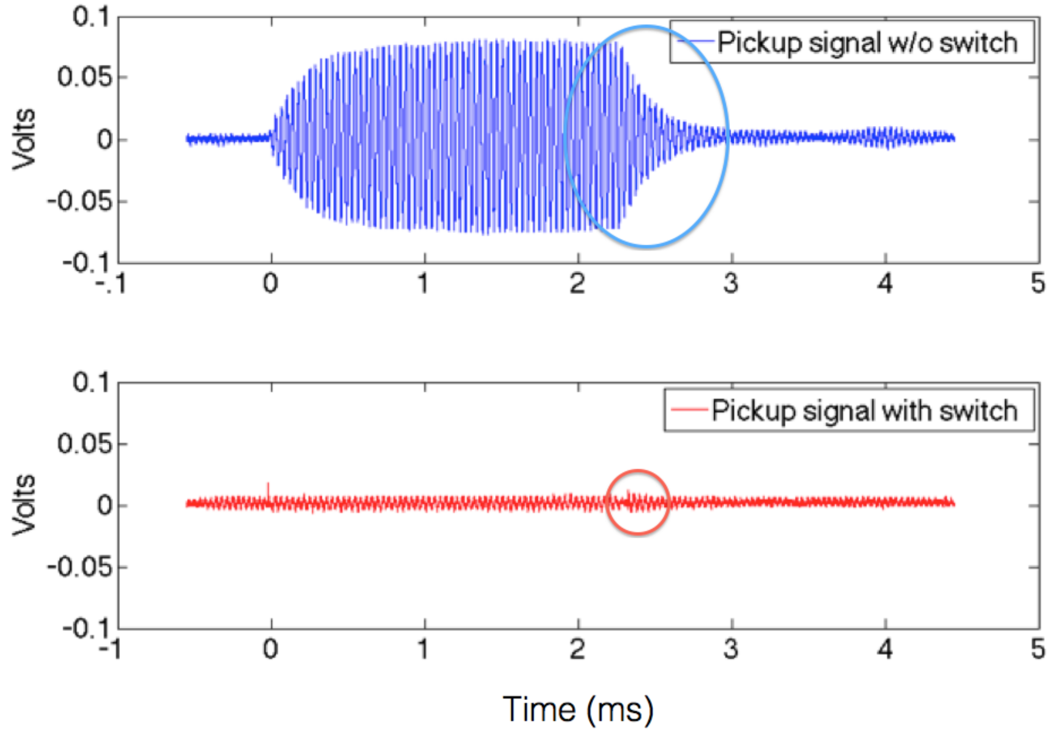


**Figure 4.10:** Shown is the effect of adding a Q-killing resistor to the pickup coil on how much cross-talk is seen from the $B_1$ coil. The top plot is the signal in the pickup coil without the analog switch (or with the switch turned off). For the bottom plot, the $B_1$ coil is at the same strength, and the mechanical decoupling has not changed, but the analog switch is turned on. This way, a large amount of the current generated in the pickup coil is dumped through the switch, damping the cross-talk significantly. The most significant effect is that the ring-down is reduced to almost nothing, so data can be taken as soon as possible after the $B_1$ pulse is turned off. The ring-down in each case is circled in the plots.

data sets are then subtracted from each other, and I look for evidence of FID in the data after the $B_1$ pulse has turned off.

### 4.3.1 Cross-talk

Cross-talk poses some issues for FID experiments, even though the $B_1$ field is off during the actual signal collecting. Since the pickup coil is connected to a resonant circuit, any resonant signal induced in it will build up over several cycles, and also ring down when the source is turned off. Cross-talk generates a resonant signal, and the ring down looks qualitatively identical to an FID signal; it is an exponentially decaying signal that starts just when the $\pi/2$ pulse is turned off.

Cross-talk during the $B_1$ pulse could be mitigated with the bucking coil, just like during AFP, but that requires additional function generators, and setting the phase correctly for the bucking coil would be more difficult than for AFP. There is a more elegant solution. For FID, the ideal configuration would be to have a high-Q resonant circuit during the data gathering part of the experiment, but a damped, low-Q circuit during the $\pi/2$ pulse. This can be achieved by adding a switching resistor to the tuning box. I built the circuit on an external printed circuit board (PCB), which connects to the tuning box via a short BNC cable. This way, the box can be easily used for both FID, with the switching resistor attached and AFP without it. A 5 V signal is sent to the switch during the $\pi/2$ pulse, which turns on the resistor, damping the circuit significantly. The resistor turns off after the pulse is over, restoring the high Q-factor, so the signal from the precessing nuclei is maximized. The resistor is a CD4066BE integrated circuit (IC), with a resistance of about 75 Ω when on (and effectively infinite resistance when off), and is controlled by a function generator, set to "pulsed" output, to +5 V when $B_1$ is on, and 0 V otherwise.

Figure 4.10 shows the results of testing this method. These plots were taken without the use of the lock-in amplifier (although the pre-amp, which amplifies the signal by a factor of 100, was used), so they are not demodulated, leaving the underlying sine wave in the signal intact. The pickup and $B_1$ coils were intentionally left slightly coupled, so that the effect of the resistor could be seen more clearly. The damping is significant, enough to reduce the cross-talk almost down to the noise floor under these conditions.

Figure 4.11 is a schematic of how the coils and electronics are connected, including the Q-killing resistor in the pickup coil circuit. With the switch open (0 V), the resistor has no effect on the circuit, so it maintains a high Q factor. With it closed, I measured about 75 Ω of resistance. Some of the power generated in the pickup coil due to the cross-talk is dissipated in this resistor. The lower the resistance, the more effective this method is. Finding an IC with lower resistance would be potentially beneficial.

### 4.3.2 FID results

When performing FID on protons in water, the experiment can be done repeatedly on the same sample, since the protons return to their Boltzmann polarization on their $T_1$ time scale. For the FID experiments in this section, I repeated the $B_1$ pulse every 1.5 seconds, and averaged many runs together, to increase SNR.

For the first FID attempt, the lock-in amplifier was set to a sensitivity of 5 mV, a time constant of 1 ms and a slope of 24 dB. In this initial run, a very short $T_2^*$ time was expected. Based on the simulations described in Chapter 3, and the center field strength measured from the actual coils, it was expected that the inhomogeneity would be around 2-3 $\mu$T, corresponding to a $T_2^*$ time of around 10-15 ms. Figure 4.12 shows the results of this experiment, including a baseline that was subtracted out to get the FID signal itself, in green on this plot.

The result was encouraging since the $T_2^*$ time looked about right. However, since the potentiometer was mistakenly connected to the wrong coil, the $T_2^*$ time should actually be considerable shorter. Like described in Section 4.1.2, the inhomogeneity is actually closer to about 10 $\mu$T, corresponding to a $T_2^*$ time of around 2 ms.

Figure 4.13 shows the results of repeating the experiment with a shorter time constant on the lock-in amplifier. Due to increased noise, more averages needed to be taken to get adequate SNR. In this case, about 3000 FID runs were averaged together, over a period of about an hour and a half, with a 1.5 second delay between $\pi/2$ pulses. Figures 4.14 and 4.15 show the signals from the two FID measurements, with the data taken during cross-talk truncated, and an exponential fit through the remaining data. The $T_2^*$ time was measured by these fits to be $1.287 \pm 0.015$ ms, and $1.203 \pm 0.016$ ms by the two runs, close to the expected 2 ms. Based on these results, the inhomogeneity across the water bottle is $18.9 \pm 0.9$ $\mu$T.

Despite the averaging, there is still considerable noise, which is clearly sinusoidal, at about 700 Hz, which is particularly noticeable in the baseline measurement, shown in red in Fig. 4.13. Because of this noise, the baseline was not subtracted from the data for the fit. The lock-in amplifier demodulates the signal it receives, so this noise should actually be found at either 27.77 kHz, or 26.37 kHz (700 Hz above or below the amplifier's setting of 27.07

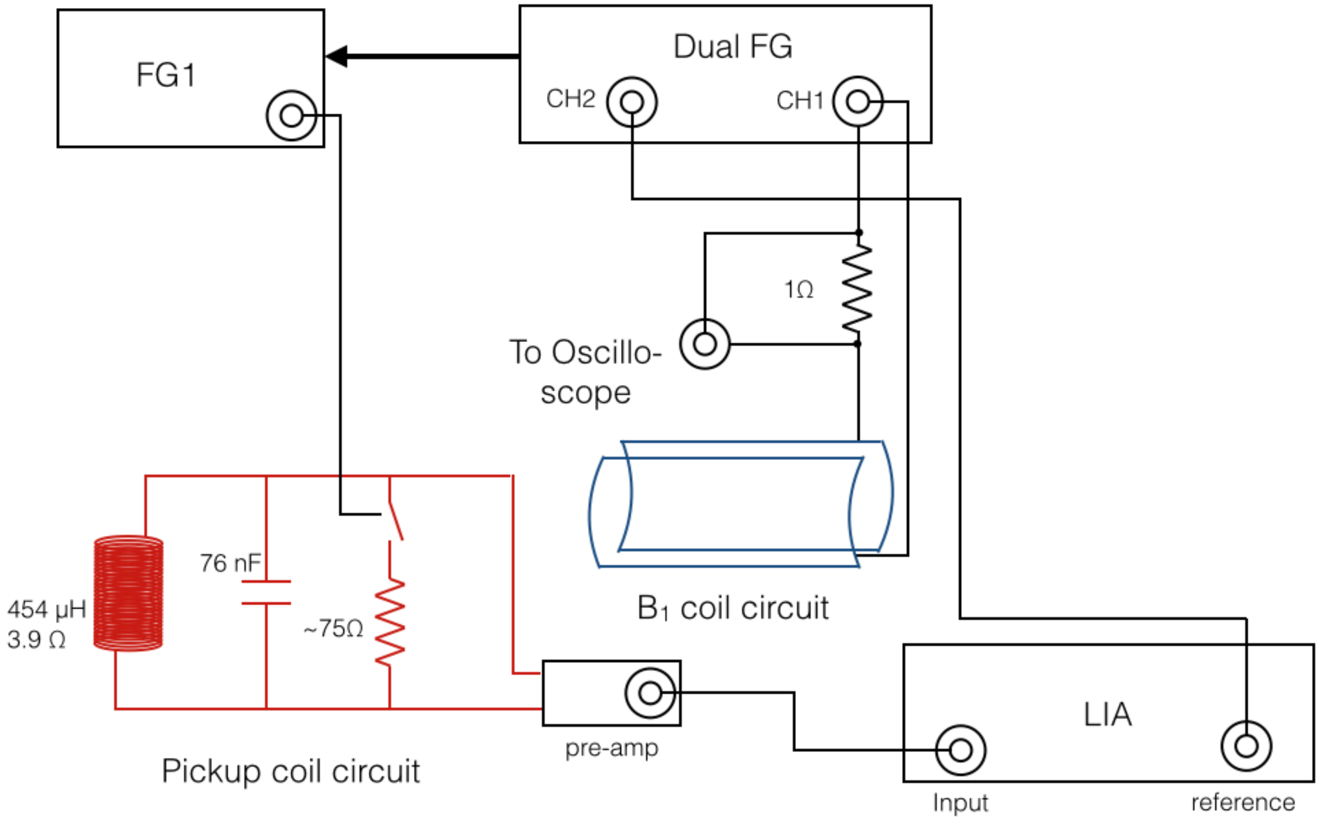


**Figure 4.11:** Here is a schematic of how the circuits and function generators are hooked up for doing FID. Channel 1 on the dual output function generator is used to drive the $\pi/2$ pulse on the $B_1$ coil. To make sure that phase is maintained between the pickup coil circuit's signal and the lock-in amplifiers demodulation, channel 2 of the same function generator is a long burst at the same frequency that is fed into the LIA's reference input. When doing FID on protons in water, the experiment can be repeated. In this case, both channels are run in burst mode, with the reference channel's burst lasting almost the entire burst period, skipping only one cycle. The function generator's burst also triggers a single output function generator, FG1. This is set to send a 5V pulse to the resistor in the pickup coil circuit for the duration of the $\pi/2$ pulse. The pickup coil's signal is sent to the LIA input through a 100x pre-amp.

kHz). To investigate this, I measured the pickup coil's output through the lock-in amplifier, while scanning the reference frequency and with no known sources driving a signal in the pickup coil. This way, any EMF generated in the pickup coil is from a source of noise. I found that there was clearly stronger noise at 27.77 kHz than other nearby frequencies. The frequency or phase of this noise does seem to drift slowly over time, which is why averaging the signal reduces it. It can be filtered out by increasing the time constant, as can be seen from the first FID attempt, with a time constant of 1 ms, but that is not an option unless the $B_0$ field gradient is improved significantly so that the actual FID signal lasts longer. The source of this noise is still unknown.

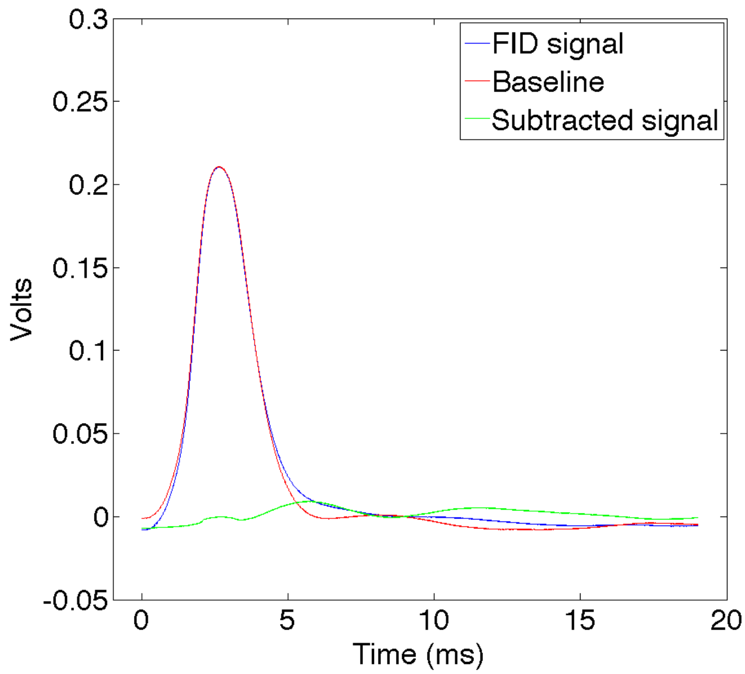


**Figure 4.12:** The results from the initial FID attempt. This experiment was performed with a time constant of the lock-in amplifier set to 1 ms . Data were gathered twice, once with the sample on resonance (blue plot), and once with the sample off resonance by adjusting the $B_0$ field strength (red plot). This way the cross-talk from the $B_1$ coil can be subtracted out. The result of this subtraction is the green plot here. There is some evidence of an FID signal.

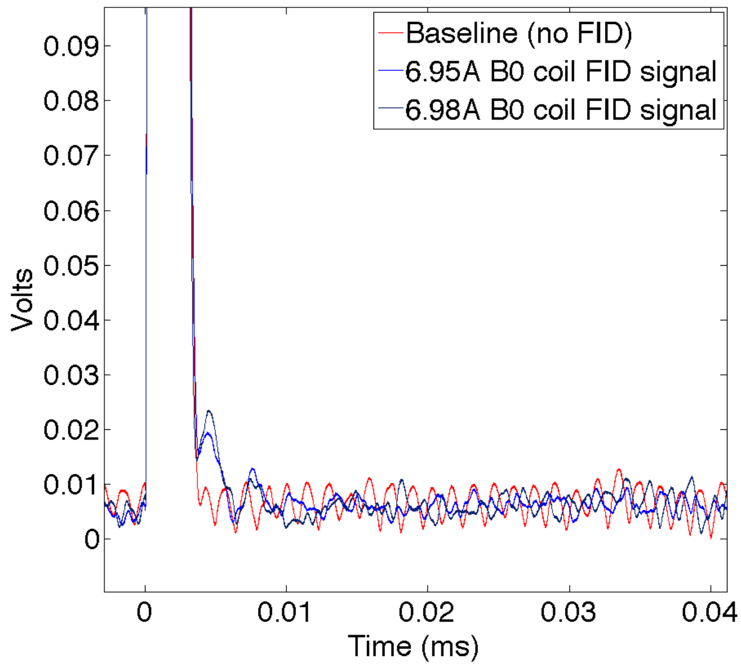


**Figure 4.13:** Another FID attempt, this time with a time constant of 100 $\mu$s. This plot was generated by taking the $x$ and $y$ channel inputs, and adding them in quadrature for each run. Shown are two data sets with the nuclei near resonance with the $B_1$ coil, at 6.95 A and 6.98 A through the $B_0$ coil, as well as a data set with the nuclei far off resonance, as a baseline (the current was about 6 A). In the baseline measurement, the nuclei would be unaffected by the $\pi/2$ pulse, and there would be no precession, and no EMF in the pickup coil. The FID runs look very similar, and there is a noticeable signal above the baseline just after the $B_1$ coil is turned off. The subtracted signals are shown in Figs. 4.14 and 4.15, with an exponential fit of each.

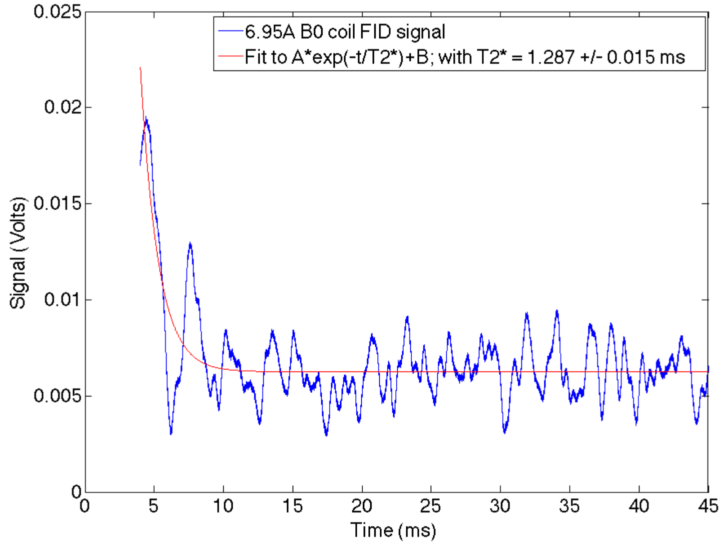


**Figure 4.14:** This is the FID signal at $B_0$ = 6.95 A (blue) and an exponential fit through the data (red). The data before the 5 ms point is removed, since it is contaminated by the remaining cross-talk from the $B_1$ pulse. $T_2^*$ is measured to be $1.287 \pm 0.015$ ms.

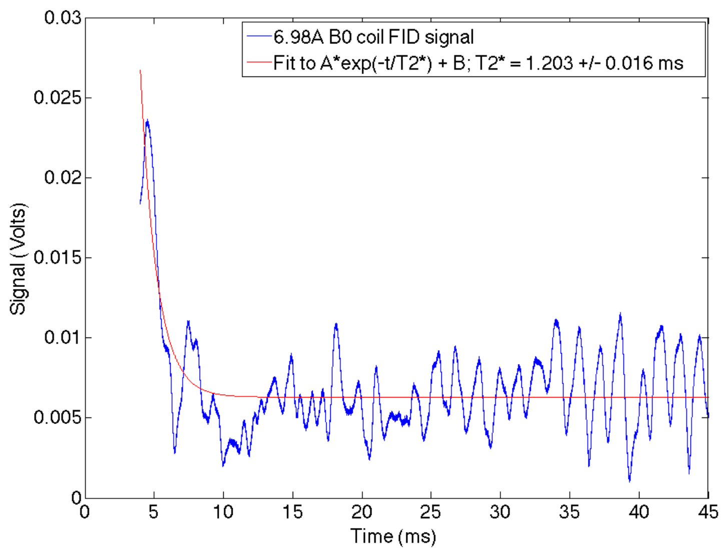


**Figure 4.15:** This is the FID signal at $B_0$ = 6.98 A (blue) and an exponential fit through the data (red). The data before the 5 ms point is removed, since it is contaminated by the remaining cross-talk from the $B_1$ pulse. $T_2^*$ is measured to be $1.203 \pm 0.016$ ms.

### 4.3.3 Spin Echo

The $T_2$ time can be found by doing a spin echo experiment, like described in Section 2.4.3. Figure 4.16 shows how the function generators and other electronics are set up to generate the needed pulses. This can be simplified a great deal by using programmable function generators or switching circuits, but we did this experiment with little time, and with equipment we could find in our lab. We combined the outputs from two function generators to generate the two pulses for the $B_1$ coil, and the outputs from two other function generators to provide the transistor-transistor logic (TTL) signal for the Q-killing switch. These function generators are all triggered on each other so that the pulses and TTL signals are active at the same times. The delay between the $\pi/2$ and the $\pi$ pulses is adjustable on one of the function generators.

This experiment is very similar to FID, but with an added $\pi$ pulse that comes after the sample has depolarized due to an inhomogeneity in the $B_0$ field. After the pulse, the spins will briefly be in phase again, generating a peak in the signal after the $\pi$ pulse. This ”revival peak” will come at a time after the $\pi$ pulse exactly equal to the time between the $\pi/2$ pulse and the $\pi$ pulse.

Figure 4.17 shows the initial attempt I made at finding a spin echo. This experiment was a partial success; there appears to be a small signal where it is expected to be, but the original FID signal is missing, potentially drowned out by leftover ringdown from cross-talk with the $B_1$ coil. It seems very likely that the peak is indeed a spin echo since it would be difficult to explain the existence of a signal there in the data otherwise. Unfortunately, without being able to measure the height of the original FID peak, this data is not useful for determining the $T_2$ time of the sample. Once better data can be taken, the experiment can be repeated, adjusting the delay time between the pulses each time, and recording the height of the revival peak. The heights of these peaks can be fit to an exponential decay, with the time constant of the decay being the $T_2$ time.

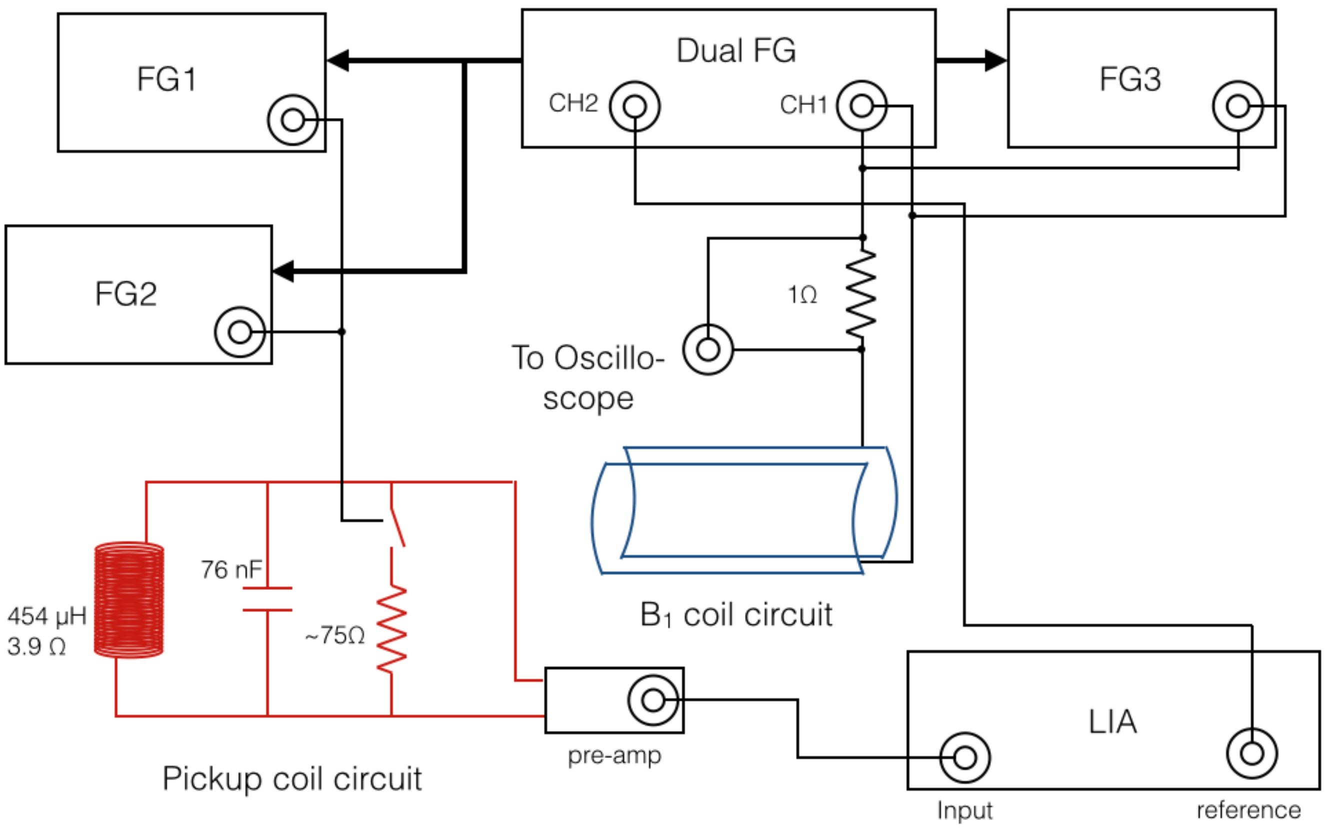


**Figure 4.16:** The spin echo experiment's schematic is quite similar to the FID's. There are two additional function generators used to generate the second pulse. FG2's output is added to FG1's, to supply the two 5V pulses to the Q-killing resistor. FG3 adds a delayed $\pi$ pulse to the $\pi/2$ pulse already generated by CH1 of the dual output FG.

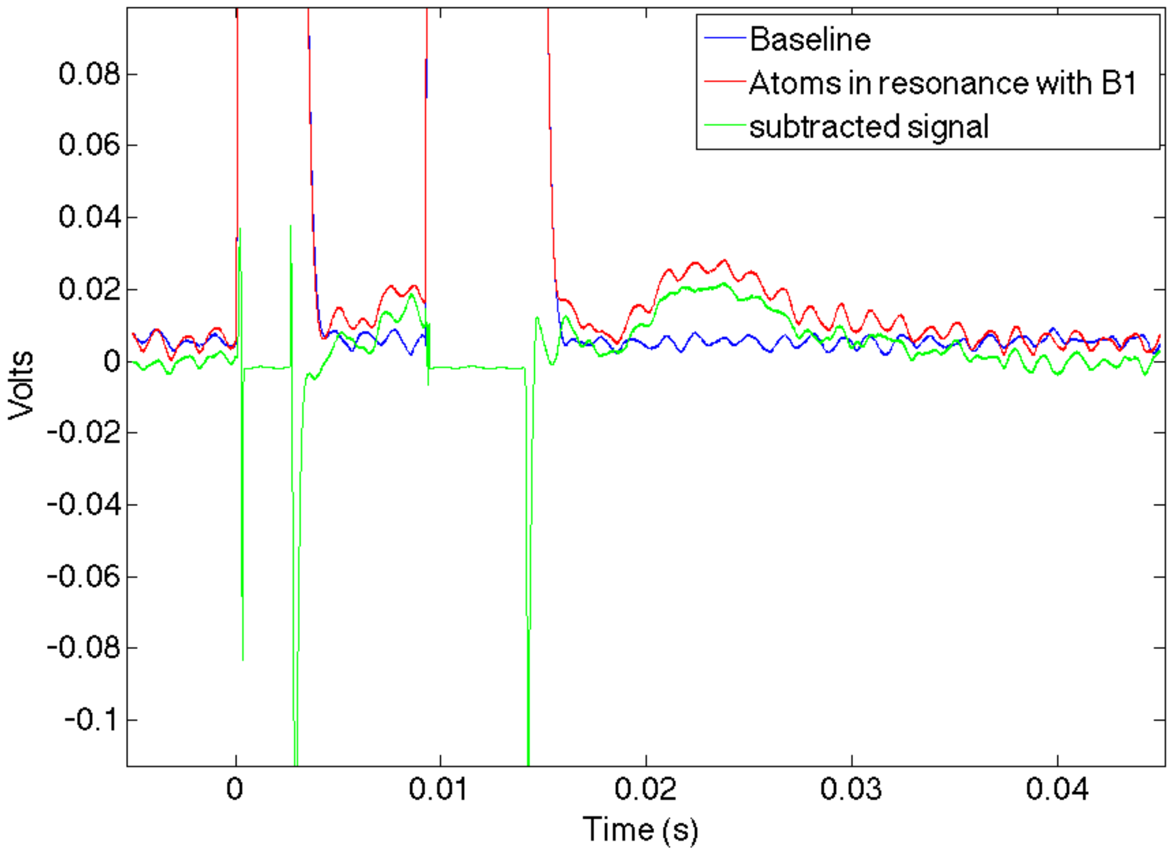


**Figure 4.17:** The signal from a spin echo experiment. The green is the subtracted signal, and there is evidence of a spin echo seen after the second pulse, the $\pi$ pulse. However, the original FID signal is not seen. This experiment should be repeated for confirmation, and if it is successful, repeated for various time delays so that the spin echo peak height can be fit to an exponential decay to determine the $T_2$ lifetime.

# Chapter 5

# Conclusions and Future Work

## 5.1 Conclusion

I have designed and built a set of magnetic coils to use in nuclear magnetic resonance (NMR) experiments, and used them to perform adiabatic fast passage (AFP) and free induction decay (FID) on protons in water. I have shown that they should be useful in their current configuration for measuring the degree of polarization of $^{129}$Xe.

I have characterized the coils, measuring the field they generate, per Amp, as well as the $B_0$ field's homogeneity, especially along the $z$ axis. The $B_0$ coils generate a field of 94.3 $\mu$T/A at their center, when placed above the steel optical table, and with no compensation for the gradient it produces. The $B_0$ field's inhomogeneity along the vertical axis of the water bottle, for the experiments in Chapter 4 was measured with a flux gate to be about 10 $\mu$T The $T_2^*$ time of water was measured twice, with the results $T_2^*$ = 1.287 ± 0.015 ms and $T_2^*$ = 1.203 ± 0.016 ms. The total $B_0$ field gradient across the entire water bottle, calculated from these times is 18.9 ± 0.9 $\mu$T. This means that a large portion of the inhomogeneity is still from the gradient along the $z$ direction due to the steel table's distorting effects on the $B_0$ field. There was an attempt made to do a spin echo experiment, but it was inconclusive.

There is disagreement in the $B_1$ coil's field measurement at 27.07 kHz. When measuring the field strength at direct current (DC) and then using theory to predict the damping effect of the alternating current (AC) shield for the field at 27.07 kHz, the strength should be about $(97 \pm 4)*(1 - r_{\text{coils}}/r\text{shield})$, or about 87.3 ± 3.6 $\mu$T/A. However, fitting the AFP peak heights to a Landau-Zener model gives the result of 10.9 ± 0.3 $\mu$T/A. Looking at the adiabaticity condition and the peak heights, it seems more likely that the DC field measurement is more accurate.

## 5.2 Possible Improvements

The next milestone for this project is to successfully perform $^{129}$Xe FID. To do so, it would be very helpful, and possibly necessary, to improve the signal to noise ratio (SNR) to the point that we do not need to average 100s or 1000s of runs to find an FID signal. Improvements to the AC shield may help in this regard, depending on the actual source of the noise, especially the strong noise at about 27.77 kHz can be damped. A higher SNR can also be achieved by improving the $B_0$ field homogeneity, to maximize the $T_2^*$ time. If the FID signal lasts longer, we can use longer integration times on the lock-in amplifier, improving the signal amplitude, and narrowing the frequency band of the amplifier.

Because all of the data for the results described in Chapter 4 were taken before analyzing them, there are a number of improvements that can be made to the setup which are now clear to us, that were not implemented for this thesis.

### 5.2.1 AC Shield

The effectiveness of the AC shield was never tested rigorously, but there is still a significant noise source at about 27.77 kHz that is seen clearly in the FID data. This noise is either generated somehow inside the shield, is related to the electronics in the pickup coil circuit, or is externally generated noise that is not sufficiently damped by the shield. The easiest way to test the shield, if the noise source is external to it, is to remove the upper $B_0$ coil from the shield, and do NMR without the top half of the shield present. If the noise is no worse than with the shield attached, then the shield is likely not being very effective.

### 5.2.2 B0 Coil Homogeneity

Since the $B_0$ field measurements were done after the NMR experiments, it was not discovered, until too late, that the compensating potentiometer was connected to the wrong coil. The field homogeneity can be easily improved by attaching it to the correct coil. However, fine-tuning this potentiometer is challenging, since the best way to see if the homogeneity overall has improved is to do FID and find the $T_2^*$ time of the sample in that field. By compensating for the field gradient this way, the center field strength is also changed, meaning the resonance frequency needs to be found again each time FID is performed after adjusting the gradient. A more time efficient method is to use an anti-Helmholtz pair of coils as the compensation method. The field of such a pair of coils is 0 at the center, so when adjusting their strength, the gradient is changed, but not the center field strength. This method was initially rejected due to concerns about having the space for such coils, but it would be worth the time and effort to look for ways to make it work.

### 5.2.3 B1 Pulse for FID

In analyzing the AFP data taken while varying the $B_1$ strength, there is strong disagreement between the expected $B_1$ field per amp of current, and that found by using the Landau-Zener model. This means that when performing FID, the $\pi/2$ pulse may not have actually tipped the spins by $\pi/2$. The best way to truly measure the $B_1$ field strength per Amp might be to adjust the duration or amplitude of the $\pi/2$ pulse until the FID signal strength is maximized.

### 5.2.4 FID Repetition Rate

When I performed FID, I repeated the experiment every 1.5 s and averaged the results to improve SNR. However, if the experiment is repeated too quickly, the spins have not had time to return to Boltzmann polarization. The result is that the amplitude of the FID signal is diminished. The $T_1$ time of water is about 1.7 s under most conditions[33], but the measurement I made suggests a longer time, of almost 3 s. The repetition rate for FID should be decreased significantly. Despite the longer repetition time, the increased SNR will make it so fewer runs need to be averaged, which will hopefully result in a quicker, more accurate FID measurement. This makes improving the $B_0$ homogeneity and optimizing the $\pi/2$ pulse quicker, since both improvements require repeated FID experiments.

## 5.3 Next Steps

The next milestone for this project is to successfully perform $^{129}$Xe FID. To do so, it would be very helpful, and possibly necessary, to improve the SNR to the point that we do not need to average 100s or 1000s of runs to find an FID signal. The improvements described in Section 5.2 are all intended to work towards this goal. The $B_0$ coil homogeneity, and the $B_1$ field strength per amp of current are the most important improvements, since they will also improve the signal seen when testing the ultraviolet (UV) laser using this setup.

By performing AFP on $^{129}$Xe, its polarization can be estimated by comparing the amplitude of the signal to that of water, which has a known polarization. There are a number of factors to keep in mind when doing so, however. The precession frequency of $^{129}$Xe is smaller than that of a proton, so each $^{129}$Xe nucleus will contribute less to the electromotive force (EMF) generated in a pickup coil than each proton. Since the precession frequencies are different, a separate tuning box needs to be made for each of the samples. These boxes will inevitably have a different Q-factor. The Q-factor for each tuned circuit needs to be measured so this can be corrected for. The comparison is made the most difficult by the fact that the pickup coil and container are also different between the water and the $^{129}$Xe sample. The signal amplitude depends on factors such as how many windings are in the pickup coil, its diameter, and how much of the space inside the coil is filled with the sample. Despite these challenges, a careful comparison the signal from a water sample is the best way to estimate the $^{129}$Xe polarization.

After finding evidence of sufficiently hyperpolarized $^{129}$Xe, and having successfully performed FID on it, the UV laser can be tested for its ability to measure the $B_0$ magnetic field strength. The laser will be circularly polarized before being shined on the precessing $^{129}$Xe. Due to the additional angular momentum imparted on the $^{129}$Xe atoms when absorbing a photon of this light, only atoms with a particular spin state will be able to absorb the light and be transferred to an excited state. This absorption will be sinusoidal due to the spin precession. Emission from these atoms as they decay back to the ground state is detected, and the frequency of that emission is used to calculate the magnetic field strength from the $^{129}$Xe gyromagnetic ratio.

# Bibliography


[1] Emily Altiere. The adventures of nikita and casper. Master's thesis, University of British Columbia, 2014. → pages iii, 11

[2] J. Beringer (Particle Data Group). Neutron properties. *PR*, D86(010001), 2012. → pages 1

[3] Maxim Pospelov and Adam Ritz. Electric dipole moments as probes of new physics. *Annals of Physics*, 2005. → pages 1, 2

[4] S. Dar. The neutron edm in the sm: A review. *arXiv:hep-ph/0008248v2*. → pages 2

[5] P.J. Mohr, B.N. Taylor, and D.B. Newell. Codata recommended values of the fundamental physical constants: 2010. *NIST*, March 2012. → pages 2

[6] C.A. Baker et al. An improved experimental limit on the electric-dipole moment of the neutron. *Phys. Rev. Lett.*, 97(13):131801, Sep 2006. → pages 2, 7

[7] I.I. Raby, N. F. Ramsey, and J. Schwinger. Use of rotating coordinates in magnetic resonance problems. *Reviews of Modern Physics*, 26(2), 1954. → pages 5

[8] Laura I. Sacolick, Florian Wiesinger, Ileana Hancu, and Mika W. Vogel. B1 mapping by bloch-siegert shift. *Magnetic Resonance in Medicine*, 63, May 2010. → pages 5

[9] N. F. Ramsey. Resonance transitions induced by perturbations at two or more different frequencies. *Physical Review*, 100(4), November 1955. → pages 6

[10] F. Bloch and A. Siegert. Magnetic resonance for nonrotating fields. *Physical Review*, 57, March 1940. → pages 6

[11] J. H. Smith, E. M. Purcell, and N. F. Ramsey. Experimental limit to the electric dipole moment of the neutron. *The Physical Review*, 108(1):292–294, 1957. → pages 6

[12] J. H. Christenson, J. W. Cronin, V. L. Fitch, and R. Turlay. Evidence for the 2 decay of the k20 meson. *Phys. Rev. Lett.*, 13(4):138–140, July 1964. → pages 6

[13] Jen-Chieh Peng. Neutron electric dipole moment experiments. *Modern Physics Letters A*, 23:1397–1408, 2008. → pages 6

[14] I. S. Altarev. A search for the electric dipole moment of the neutron using ultracold neutrons. *Nuclear Physics*, 1980. → pages 6, 7

[15] A. Pichlmaier, V. Varlamov, K. Schreckenbach, and P. Geltenbort. Neutron lifetime measurement with the ucn trap-in-trap mambo ii. *Physics Letters B*, 2010. → pages 7

[16] R. Golub and J.M. Pendlebury. Ultra-cold neutrons. *Rep. Prog. Phys.*, 42:440–501, 1979. → pages 7

[17] E.B. Saloman. Energy levels and observed spectral lines of xenon, xe i through xe liv. *J. Phys. Chem. Ref. Data*, 33(3):765–921, 2004. → pages 8

[18] Sakurai and Napolitano. *Modern Quantum Mechanics*. Pearson Education, Inc., 2nd edition, 2011. → pages 16

[19] J. E. Sansonetti. Wavelengths, transition probabilities, and energy levels for the spectra of rubidium (rb i through rb xxxvii). *J. Phys. Chem. Ref. Data*, 35(1):301–421, 2006. → pages 19, 20

[20] HyperPhysics Concepts. http://hyperphysics.phy-astr.gsu.edu/hbase/hph.html. *date retrieved*, Jan 14 2016. → pages 20

[21] W. Happer. Theory of spin-exchange optical pumping of 3he and 129xe. *Physical Review A*, 58(2):1412–1439, August 1998. → pages 21

[22] F. Bloch. Nuclear induction. *Phys. Rev.*, 1946. → pages 26

[23] Troy Dawson. Development of a xenon polarizer for magnetometry in neutron electric dipole moment experiments. Master's thesis, University of Manitoba, 2013. → pages 27

[24] D.J. Griffiths. *Introduction to Electrodynamics*. Prentice-Hall, Inc., 3rd edition, 1999. → pages 33

[25] C.P. Bidinosti et al. Active shielding of cylindrical saddle-shaped coils. *Journal of Magnetic Resonance*, 177:31–43, 2005. → pages 36, 37, 39, 48

[26] M. Abramowitz and I.A. Stegun, editors. *Handbook of Mathematical Functions With Formulas, Graphs and Mathematical Tables*. National Bureau of Standards, 1972. → pages 38

[27] P. Hammond. Electric and magnetic images. *The Institution of Electrical Engineers*, (379), May 1960. → pages 42

[28] C.C. Finlay et al. International geomagnetic reference field: the eleventh generation. *Geophys. J. Int.*, 183:1216–1230, 2010. → pages 44

[29] S. Fahy, Charles Kittel, and Stevel G. Louie. Electromagnetic screening by metals. *Am. J. Phys,*, 56(11):989–992, November 1988. → pages 47

[30] C.P. Bidinosti and J.W. Martin. Passive magnetic shielding in static gradient fields. *AIP Advances*, 4, 2014. → pages 48, 60

[31] C.P. Bidinosti, Yu Sakamoto, and Koichiro Asahi. General solution of the hollow cylinder and concentric dc surface current. *IEEE Magnetics Letters*, 5, 2014. → pages 48

[32] Kahan McAffer Dare. Tools for trapping and detecting ultracold gases. Master's thesis, University of British Columbia, 2016. → pages 60

[33] Paul A. Bottomley, Thomas H. Foster, Raymond E. Argersinger, and Leah M. Pfeifer. A review of normal tissue hydrogen nmr relaxation times and relaxation mechanisms from 1-100 mhz: Dependence on tiddue type, nmr frequency, temperature, species, excision and age. *Medical Physics*, 1984. → pages 74

# Appendix A

# Matlab Code

This appendix lists holds the simulations that I coded to obtain the data for Chapter 3.

## A.1 Helmholtz Coils

This simulation calculates the magnetic field created by a Helmholtz pair of coils. It is all contained in one file.

```
% Created by Joshua Wienands

% This is a Program to calculate the magnetic field of a pair of coils in
% Helmholtz configuration, or at some other separation distance.
% It is assumed that the atoms are in a cylindrical cell.

% The field is calculated using the finite differences technique. The
% Biot-Savart Law is a differential equation that tells us the strength of
% magnetic field produced by an infinitely short piece of straight wire.
% The exact solution would be to integrate this over the entire wire (which
% is a coil in this case). The approximation comes from instead taking a
% finite length and summing rather than integrating. This is equivalent to
% the coils being made up of short, straight pieces of wire, rather than
% being actual circles.

% You can define the following constants:

% FOR THE MAGNETIC FIELD:
% coil size
% coil separation
% current
% number of windings
% length and radius of cell (which is cylindrical, cannot easily be changed)
%
% resolution in r and distance to go in r
% resolution in z and distance to go in z
% resolution in dL for the Biot-Savart calculation


% NOTE:
% For vectors containing data such as position, velocity, magnetic field,
% the first entry is the x direction, second the y direction, and third the z
% direction.

```

```
% The axis going through the center of the two coils is the z axis.
% The program assumes a cylindrical cell, with its long axis pointing in
% the r (or equivalently, x or y) direction

% Values defined in all caps are either physical constants or constant
% parameters that can be chosen. Their value should not be altered by the code
% later in the program.

% 10A, 100 windings results in 30G field at center for helmholtz config.

clear all;
format long;

%Constants:
MM = 10^-3;
K = 10^-7; % k =  0/4*pi = 10^-7 N/A^2

% simulation resolution
Z_STEPS = 100; % The number of data points in z direction. Increasing this increases simulation time linearly
MAX_D = 20*MM; % Max distance from the center of the coil pair along z to calculate field
               % Make sure to include the size of the cell's radius in this
R_STEPS = 1; % number of data points in R direction, Increasing this increases the simulation time mostly linearly
MAX_R = 120*MM; % Max radial distance from center of the coil pair to calculate field
               % Make sure to include the entire center to corner Cell length within this
L_STEPS = 50; % resolution of the length element dL of the wire in coils
%              100 or so steps here looks to be enough to at least 1% accuracy
%              increasing this increases simulation time linearly

%Coil Parameters:
SEPARATION = 300*MM; % separation between the coils in meters, along z axis
RADIUS = 300*MM; % Radius of the coils in meters
CURRENT = 4.04; % current in Amps
NUM_WINDINGS = 100; % number of windings

% Cell parameters
CELL_RADIUS = 12.7*MM; % radius of the cell in meters
CELL_LENGTH = 200*MM; % length of the cell in meters

B0 = zeros([2*R_STEPS+1, 2*Z_STEPS+1, 4]); % initialize the B0 matrix
%                                            It is sufficient to calculate 1 quadrant
%                                            the rest is symmetric

z_step_size = MAX_D/Z_STEPS; % calculate the z step size in m
r_step_size = MAX_R/R_STEPS; % calculate the r step size in m
l_step_size = 2*pi*RADIUS/L_STEPS; % calculate the length of dL in m


% Calculate the field from the two coils using finite differences technique
% and the Biot-Savart Law. This step can probably still be optimized
% significantly by eliminating nested loops in favor of vectorization. Most
% of the commented out code here is from attempts to do so.

theta = 0:2*pi/L_STEPS:(2*pi-l_step_size);
dL = [-1.0*RADIUS*2*pi*sin(theta)/L_STEPS;RADIUS*2*pi*cos(theta)/L_STEPS;zeros(1,L_STEPS)];
for i = 0:Z_STEPS
    i %#ok<NOPTS> % print the iteration the program is on
    z = z_step_size*i; % start the z steps at z = 0
```

```
    for ii = 0:R_STEPS
        r = r_step_size*ii; % start the r steps at r = 0

        for iii = 1:L_STEPS

            % contribution from lower coil
            % vector pointing from wire to measurement point
            x = [r, 0, z + SEPARATION/2]-[RADIUS*cos(theta(iii)),RADIUS*sin(theta(iii)),0];
            xmag = sqrt((x(1)^2 + x(2)^2 + x(3)^2)); % magnitude of this vector
            dB0 = K*CURRENT*NUM_WINDINGS*cross(dL(:,iii),x)/(xmag^3);

            % contribution from upper coil
            % vector pointing from wire to measurement point
            x = [r, 0, z - SEPARATION/2]-[RADIUS*cos(theta(iii)),RADIUS*sin(theta(iii)),0];
            xmag = sqrt((x(1)^2 + x(2)^2 + x(3)^2)); % magnitude of this vector
            % This is the change in B field in Tesla, add it to the change from other coil
            dB0 = dB0 + K*CURRENT*NUM_WINDINGS*cross(dL(:,iii),x)/(xmag^3);



            % add up the field contribution.
            % currently just the magnitude, direction is commented out
            % above, and only for one quadrant.
            % Calculation only needs to be done for one quadrant, but need
            % to populate the whole matrix, so add appropriately to each of
            % the 4 quadrants by centering around R_STEPS and Z_STEPS
            % Also, be careful to avoid overlap and avoid trying to write
            % to the 0th index of a matrix


            B0((R_STEPS + 1) + ii, (Z_STEPS + 1) + i, 1) = B0((R_STEPS + 1) + ii, ...
                (Z_STEPS + 1) + i, 1) + dB0(1);
            B0((R_STEPS + 1) + ii, (Z_STEPS + 1) + i, 2) = B0((R_STEPS + 1) + ii, ...
                (Z_STEPS + 1) + i, 2) + dB0(2);
            B0((R_STEPS + 1) + ii, (Z_STEPS + 1) + i, 3) = B0((R_STEPS + 1) + ii, ...
                (Z_STEPS + 1) + i, 3) + dB0(3);% Lower right quadrant

            if ( i ~= 0)
                B0((R_STEPS + 1) + ii, (Z_STEPS + 1) - i, 1) = ...
                      B0((R_STEPS + 1) + ii, (Z_STEPS + 1) - i, 1) + dB0(1);
                B0((R_STEPS + 1) + ii, (Z_STEPS + 1) - i, 2) = ...
                      B0((R_STEPS + 1) + ii, (Z_STEPS + 1) - i, 2) + dB0(2);
                B0((R_STEPS + 1) + ii, (Z_STEPS + 1) - i, 3) = ...
                      B0((R_STEPS + 1) + ii, (Z_STEPS + 1) - i, 3) + dB0(3);% Lower left
                if (ii ~= 0)
                    B0((R_STEPS + 1) - ii, (Z_STEPS + 1) - i, 1) = ...
                          B0((R_STEPS + 1) - ii, (Z_STEPS + 1) - i, 1) + dB0(1);
                    B0((R_STEPS + 1) - ii, (Z_STEPS + 1) - i, 2) = ...
                          B0((R_STEPS + 1) - ii, (Z_STEPS + 1) - i, 2) + dB0(2);
                    B0((R_STEPS + 1) - ii, (Z_STEPS + 1) - i, 3) = ...
                          B0((R_STEPS + 1) - ii, (Z_STEPS + 1) - i, 3) + dB0(3);% Upper left
                end
            end

            if ( ii ~= 0)
                B0((R_STEPS + 1) - ii, (Z_STEPS + 1) + i, 1) = ...
                      B0((R_STEPS + 1) - ii, (Z_STEPS + 1) + i, 1) + dB0(1);
```

```matlab
                B0((R_STEPS + 1) - ii, (Z_STEPS + 1) + i, 2) = ...
                    B0((R_STEPS + 1) - ii, (Z_STEPS + 1) + i, 2) + dB0(2);
                B0((R_STEPS + 1) - ii, (Z_STEPS + 1) + i, 3) = ...
                    B0((R_STEPS + 1) - ii, (Z_STEPS + 1) + i, 3) + dB0(3);% Upper right
            end

        end

        B0((R_STEPS+1)+ii,(Z_STEPS+1)+i,4) = sqrt(B0((R_STEPS+1)+ii,...
            (Z_STEPS+1)+i,1)^2+B0((R_STEPS+1)+ii,(Z_STEPS+1)+i,2)^2+ ...
            B0((R_STEPS+1)+ii,(Z_STEPS+1)+i,3)^2);
        B0((R_STEPS+1)-ii,(Z_STEPS+1)+i,4) = sqrt(B0((R_STEPS+1)-ii,...
            (Z_STEPS+1)+i,1)^2+B0((R_STEPS+1)-ii,(Z_STEPS+1)+i,2)^2+ ...
            B0((R_STEPS+1)-ii,(Z_STEPS+1)+i,3)^2);
        B0((R_STEPS+1)+ii,(Z_STEPS+1)-i,4) = sqrt(B0((R_STEPS+1)+ii,...
            (Z_STEPS+1)-i,1)^2+B0((R_STEPS+1)+ii,(Z_STEPS+1)-i,2)^2+ ...
            B0((R_STEPS+1)+ii,(Z_STEPS+1)-i,3)^2);
        B0((R_STEPS+1)-ii,(Z_STEPS+1)-i,4) = sqrt(B0((R_STEPS+1)-ii,...
            (Z_STEPS+1)-i,1)^2+B0((R_STEPS+1)-ii,(Z_STEPS+1)-i,2)^2+ ...
            B0((R_STEPS+1)-ii,(Z_STEPS+1)-i,3)^2);


    end
end


% Plot a slice in the xz plane, with the cell edges drawn in

% draw the cell edges
for i = 1:floor(1+CELL_RADIUS/z_step_size)
    r_index = floor(1+sqrt(CELL_RADIUS^2 - ((i-1)*z_step_size)^2)/r_step_size);
    B0(R_STEPS + r_index,Z_STEPS + i,4) = 0;
    B0(R_STEPS - (r_index-1),Z_STEPS + i,4) = 0;
    B0(R_STEPS + r_index,Z_STEPS - (i-1),4) = 0;
    B0(R_STEPS - (r_index-1),Z_STEPS - (i-1),4) = 0;
end

% plot the magnitude as a heat map.
% this is a slice in the xz plane, going through the origin
imagesc(B0(:,:,4));
colorbar;
caxis([0 B0(R_STEPS,Z_STEPS,4)*1.5]) % constrain the color axis because field gets huge near coils
                                    % constraint is based on the mag. of
                                    % field at the center.

% return; % end here unless you want the next plot also

% Can also plot a slice on the xy plane:

B0_xy = zeros([2*R_STEPS, 2*R_STEPS, 2*Z_STEPS]); % Initialize B0 matrix in xy plane

% Due to symmetry, the magnitude of the field is identical for all theta at
% a given r and z. B0 is a matrix with the magnitude of the field as a
% function of r and z. To plot this in a heat map, we need to create a
% matrix of the field magnitude as a function of x and y for a given z
% do this by looping over all x and y positions, and choose the magnetic
% field strength by looking up its value from r = sqrt(x^2 + y^2), taking a
```

```
% weighted average in cases where the index wouldn't be an integer.
% since we loop over all x and y up to R_MAX, there are many spots where we
% have not calculated the magnetic field. Just leave those as 0. Ideally
% these would be left blank in the plot, I'm not sure how to accomplish
% that.

for i = 1:Z_STEPS % can create a slice for every z
    for ii = 1:R_STEPS
        for iii = 1:R_STEPS % these two loops loop over x and y
            r = sqrt(iii^2 + ii^2); %find index for the value of r for that x and y
            if (r+1)<=R_STEPS % don't have any info for x^2 + y^2 > R_MAX^2, so leave them as 0
                %look for closest r available, rounded down, get field there
                B0_up = B0(R_STEPS + floor(r+1), Z_STEPS + i, 4);
                B0_down = B0(R_STEPS + floor(r), Z_STEPS + i, 4); %same thing, rounded up
                % take a weighted average of the fields, this is the field
                % at that x and y to good approximation
                % Better approximation can be made by considering the
                % actual form of the field vs. r, rather than just assuming
                % it's linear
                B_inter = (1-mod(r, 1))*B0_down + mod(r, 1)*B0_up;

                % Calculation only needs to be done for one quadrant, but need
                % to populate the whole matrix, so add appropriately to each of
                % the 4 quadrants by centering around R_STEPS
                % Also, be careful to avoid overlap and avoid trying to write
                % to the 0th index of a matrix
                B0_xy(R_STEPS+(iii-1), R_STEPS+(ii-1), Z_STEPS + (i-1)) = B_inter; % Lower right quadrant
                B0_xy(R_STEPS-(iii-1), R_STEPS+(ii-1), Z_STEPS + (i-1)) = B_inter; % Upper right
                B0_xy(R_STEPS+(iii-1), R_STEPS-(ii-1), Z_STEPS + (i-1)) = B_inter; % Lower left
                B0_xy(R_STEPS-(iii-1), R_STEPS-(ii-1), Z_STEPS + (i-1)) = B_inter; % Upper left

                B0_xy(R_STEPS+(iii-1), R_STEPS+(ii-1), Z_STEPS - (i-1)) = B_inter; % Lower right quadrant
                B0_xy(R_STEPS-(iii-1), R_STEPS+(ii-1), Z_STEPS - (i-1)) = B_inter; % Upper right
                B0_xy(R_STEPS+(iii-1), R_STEPS-(ii-1), Z_STEPS - (i-1)) = B_inter; % Lower left
                B0_xy(R_STEPS-(iii-1), R_STEPS-(ii-1), Z_STEPS - (i-1)) = B_inter; % Upper left

                % Draw the cell edges by setting the field to be 0 there.
                % long edge first

                if ii == round(CELL_RADIUS/r_step_size)
                    if iii < round(CELL_LENGTH/(2*r_step_size))
                        B0_xy(R_STEPS+(iii-1), R_STEPS+(ii-1), Z_STEPS) = 0; % Lower right quadrant
                        B0_xy(R_STEPS-(iii-1), R_STEPS+(ii-1), Z_STEPS) = 0; % Upper right
                        B0_xy(R_STEPS+(iii-1), R_STEPS-(ii-1), Z_STEPS) = 0; % Lower left
                        B0_xy(R_STEPS-(iii-1), R_STEPS-(ii-1), Z_STEPS) = 0; % Upper left


                    end
                end

                % short edge next
                if iii == round(CELL_LENGTH/(2*r_step_size))
                    if ii < round(CELL_RADIUS/r_step_size)

                        B0_xy(R_STEPS+(iii-1), R_STEPS+(ii-1), Z_STEPS) = 0; % Lower right quadrant
                        B0_xy(R_STEPS-(iii-1), R_STEPS+(ii-1), Z_STEPS) = 0; % Upper right
                        B0_xy(R_STEPS+(iii-1), R_STEPS-(ii-1), Z_STEPS) = 0; % Lower left
```

```
                        B0_xy(R_STEPS-(iii-1), R_STEPS-(ii-1), Z_STEPS) = 0; % Upper left
                    end
                end


            end
        end
    end
end



% plot the magnitude as a heat map
% this is for a slice in the xy plane

imagesc((10^4)*B0_xy(:,:,1)); % the last index determines z position. 1 is the center
colorbar;

% no need to re-scale color axis as long as we are not near the coils
% can still be useful to increase field magnitude resolution around the cell itself

caxis([(10^4)*B0_xy(R_STEPS,R_STEPS)*0.99 (10^4)*B0_xy(R_STEPS,R_STEPS)]);
```

## A.2 Saddle Coils

This simulation calculates the magnetic field created by a pair of coils in the saddle geometry. The simulation calls on two functions which calculate the contribution from a small piece of a curved part of the wire, or the length of one of the rungs, respectively. There is also a function I wrote to read the file generated by this simulation.

### A.2.1 Saddle Coil Simulation

```
MM = 10^(-3); % convert from mm to m by *MM

TABLE_POS = 310*MM; % distance from the center of the cell to the table
TABLE_ORIENT = 1; % How the table and coils are oriented.
                % 1: coils produce field perpendicular to table
                % 2: coils produce field parallel to table
                % other value: don't calculate image field
USE_FUNC = 1;
C_RATIO = 1;

SHIFT = 0*MM;
DEFORM = 0*MM;

ALPHA = 135*pi/180; %span of each coil in radians
RADIUS = 75*MM; %radius of the coils in meters
LENGTH = 400*MM; %length of the coils in meters
K = 10^(-7); % k =  0/4
CURRENT = 1; %current in amps
WINDINGS = 10; %number of windings of the coil

num_dL_curves = 200;

xy_steps = 1; % number of points in the x and y directions
```

```
B_STEPS_Z = 200; %number of points the z direction

CELL_RADIUS = 12.7*MM; %radius of the Xenon cell in meters
CELL_LENGTH = 200*MM; %length of the Xenon cell in meters

dL_curves_mag = ALPHA*RADIUS/num_dL_curves;

d_theta = ALPHA/num_dL_curves; % How much theta changes over dL

b_step_size = CELL_LENGTH/B_STEPS_Z; % step size in the z direction

xy_step_size = CELL_RADIUS*2/xy_steps; % step size in the x or y direction

B_field = zeros(xy_steps, xy_steps, B_STEPS_Z,4); % initialize the magnetic field
dBrods = [0;0;0];
dBcurved = [0;0;0];
dBr_image = [0;0;0];
dBc_image = [0;0;0];
deform_array = 2*DEFORM*rand(40,1) - DEFORM;
deform_angle = 2*pi*rand(40,1);
d_array = zeros(num_dL_curves, 1);
d_angle = zeros(num_dL_curves, 1);


for i = 1:num_dL_curves
    index = ceil(i*10/num_dL_curves);
    d_array(i) = deform_array(index);
    d_angle(i) = deform_array(index);
end

deformation = [d_array d_angle];


for bx = 1:xy_steps
    for by = 1:xy_steps
        bx
        by
        for bz = 1:B_STEPS_Z

            if B_STEPS_Z == 1 && xy_steps == 1
                b_pos = [0
                    0
                    0];

            elseif B_STEPS_Z == 1

                b_pos = [(xy_step_size*bx - CELL_RADIUS)
                    (xy_step_size*by - CELL_RADIUS)
                    0];

            elseif xy_steps == 1

                b_pos = [0
                    0
                    (b_step_size*bz - 0.5*CELL_LENGTH)];

            else
```

```
                b_pos = [(xy_step_size*bx - CELL_RADIUS)
                    (xy_step_size*by - CELL_RADIUS)
                    (b_step_size*bz - 0.5*CELL_LENGTH)]; %position the field is being measured at
            end


            dBrods = rods_BiotSavart_field(ALPHA,LENGTH,RADIUS,b_pos,CURRENT*WINDINGS, C_RATIO, ...
                    0, SHIFT);
            dBcurved = curved_BiotSavart_field(ALPHA,LENGTH,RADIUS,dL_curves_mag,b_pos, ...
                    CURRENT*WINDINGS,d_theta, C_RATIO, 0, SHIFT, deform_array);

            if TABLE_ORIENT == 1
                dist = [-2*TABLE_POS; 0; 0];
                image_pos = b_pos - dist;
                dBr_image = rods_BiotSavart_field(ALPHA,LENGTH,RADIUS,image_pos,CURRENT*WINDINGS, ...
                        C_RATIO, 1, SHIFT);
                dBc_image = curved_BiotSavart_field(ALPHA,LENGTH,RADIUS,dL_curves_mag,image_pos, ...
                        CURRENT*WINDINGS,d_theta, C_RATIO, 1, SHIFT, deform_array);

            else
                dBr_image = [0;0;0];
                dBc_image = [0;0;0];
            end


            B_field(bx, by, bz, 1) = B_field(bx,by,bz,1) + dBrods(1) + dBcurved(1) + ...
                dBr_image(1) + dBc_image(1);
            B_field(bx, by, bz, 2) = B_field(bx,by,bz,2) + dBrods(2) + dBcurved(2) + ...
                dBr_image(2) + dBc_image(2);
            B_field(bx, by, bz, 3) = B_field(bx,by,bz,3) + dBrods(3) + dBcurved(3) + ...
                dBr_image(3) + dBc_image(3);

            B_field(bx, by, bz, 4) = sqrt(B_field(bx, by, bz,1)^2 + ...
                B_field(bx, by, bz,2)^2 + ...
                B_field(bx, by, bz,3)^2);
        end

    end
end



%prepare everything to record to text file
bsize = size(B_field); %size of the magnetic field matrix
xsize = bsize(1); %split into x, y and z sizes
ysize = bsize(2);
zsize = bsize(3);
%open a file to write to, add some description to the file name
%number of dL steps and coil size at least

% build the file name
alphadeg = ALPHA*180/pi;
if CELL_LENGTH > 0.3 || CELL_RADIUS > 0.02
    region = 'big';
else
    region = 'cell';
end
```

```
if B_STEPS_Z > xy_steps
    axes = 'z';
elseif B_STEPS_Z < xy_steps
    axes = 'xy';
else
    axes = 'xyz';
end

if USE_FUNC == 1
    func = '_wfunc';
else
    func = '';
end

if TABLE_ORIENT == 1
    img = '_ximage';
elseif TABLE_ORIENT == 2
    img = '_yimage';
else
    img = '';
end


leng = LENGTH/MM;
radi = RADIUS/MM;

filename = sprintf('%ddLsteps_%ddeg_%dmmx%dmm_coil_%dA_%s_region_%s%s%s%1.3f_I_ratio_%1.3f_yshift', ...
int16(num_dL_curves),int16(alphadeg),int16(leng),int16(radi),int16(CURRENT*WINDINGS),...
      region,axes,func,img, C_RATIO, SHIFT);
i = 2;

%if the file already exists, add a number to the end of it.
if exist(sprintf('%s.txt',filename),'file')
    while exist(sprintf('%s%d.txt',filename,i),'file')
        i = i+1;
    end
    filename = sprintf('%s%d',filename,i);
end
filename = sprintf('%s.txt',filename);
fileid = fopen(filename,'w');

%print a header; the length, radius of coil, current, span of the coil in
%degrees, as well as step sizes and number of steps in each direction
%Matlab gets upset when reading if there are any non-numeric characters,
%also there should be 4 values per line
fprintf(fileid, '%f\t%f\t%f\t%f\t0\t0\t0\n', LENGTH, RADIUS, CURRENT*WINDINGS, 180*ALPHA/pi);
fprintf(fileid,'%d\t%d\t%d\t%d\t%d\t%f\t0\n', xy_steps, xy_step_size, xy_steps, xy_step_size, ...
      B_STEPS_Z, b_step_size);

% write the magnitude of the magnetic field to a text file
for i = 1:xsize
    for j = 1:ysize
        for k = 1:zsize
            xcoord = i*xy_step_size;
            ycoord = j*xy_step_size;
            zcoord = k*b_step_size;
```

```
            %print in scientific notation (%e)
            fprintf(fileid, '%e\t%e\t%e\t%1.10e\t%1.10e\t%1.10e\t%1.10e\n',xcoord,ycoord,zcoord, ...
                B_field(i,j,k,4), B_field(i,j,k,1), B_field(i,j,k,2), B_field(i,j,k,3));
        end
    end
end


fclose('all'); %close the file
```

### A.2.2 Magnetic Field From a Curved Section of Wire

```
function dBc = curved_BiotSavart_field(alpha, len, radius, dLmag, bpos, current, ...
        d_theta, current_ratio, image, shift)

    % Calculate the magnetic field due to the 4 curved portions of

    if image == 1
        coilshift = [0 shift];
    else

        coilshift = [shift 0];
    end
    K = 1e-7;
    zr = 0.5*len; % z pos stays constant
    dBc = [0;0;0];
    i = 1;

    for a = 0.5*d_theta:d_theta:alpha

            % Find the x and y components for a point on a curved part
            % of the coil, get the distance to the measurement point,
            % use Biot-Savart law to get the contribution to the field

            theta1 = alpha/2 - a; %angle for the first curved part
            xr = radius*cos(theta1);
            yr = radius*sin(theta1); %x and y components for the point


            r1 = bpos - [xr; yr; zr] + [coilshift(1); coilshift(2); 0]; %get distance
            r1mag = sqrt(r1(1)^2 + r1(2)^2 + r1(3)^2); %distance squared

            %get dL direction, magnitude was obtained before
            dLx = dLmag*sin(theta1);
            dLy = -1.0*dLmag*cos(theta1);
            dLr1 = [dLx; dLy; 0];

            %contribution from that curved piece


            %do the same thing again for the next piece
            % same coil, but other side, so flip z
            r2 = bpos - [xr; yr; -1.0*zr] + [coilshift(1); coilshift(2); 0];
            r2mag = sqrt(r2(1)^2 + r2(2)^2 + r2(3)^2);
            dLr2 = -1.0*dLr1;

```

```
            %again, for curved piece 3
            %flip x, y position, +z again though
            r3 = bpos - [-1.0*xr; -1.0*yr; zr] + [coilshift(2); coilshift(1); 0];
            r3mag = sqrt(r3(1)^2 + r3(2)^2 + r3(3)^2);
            dLr3 = dLr1;



            %finally, the 4th curved piece
            %flip x, y, z (or add rather than subtract)
            r4 = bpos + [xr; yr; zr] + [coilshift(2); coilshift(1); 0];
            r4mag = sqrt(r4(1)^2 + r4(2)^2 + r4(3)^2);
            dLr4 = -1.0*dLr1;

            if image == 1
                dB1 = K*current*(cross(dLr1,r1)/r1mag^3);
                dB2 = K*current*(cross(dLr2,r2)/r2mag^3);
                dB3 = K*current*current_ratio*(cross(dLr3,r3)/r3mag^3);
                dB4 = K*current*current_ratio*(cross(dLr4,r4)/r4mag^3);


            else
                dB1 = K*current*current_ratio*(cross(dLr1,r1)/r1mag^3);
                dB2 = K*current*current_ratio*(cross(dLr2,r2)/r2mag^3);
                dB3 = K*current*(cross(dLr3,r3)/r3mag^3);
                dB4 = K*current*(cross(dLr4,r4)/r4mag^3);
            end

            dBc = dBc + dB1 + dB2 + dB3 + dB4;
            i = i+1;

    end

end
```

### A.2.3 Magnetic Field From a Straight Rod

```
function dBr = rods_BiotSavart_field(alpha, len, radius, b_pos, current, current_ratio, image, shift)


    % Calculate the exact field at b_pos due to the 4 rod portions of the
    % saddle coil pair. No finite differences needed, the general formula
    % for the magnitude is:
    %
    %       B = (K*I/s)*[sin(theta2) - sin(theta1)]
    %
    % K is a constant, I is the current, s is the distance between b_pos
    % and the rod, theta1 is the angle between s and the vector pointing
    % from the beginning of the rod to b_pos, and theta2 is the angle
    % between s and the vector pointing from the end of the rod to b_pos.

    K = 1e-7; % constant

    % x and y positions of the rods. X axis goes through the coils, y axis
```

```
% goes between them. Z axis goes down the coil axis. Rods are centered
% around the origin.

if image == 1
    x = [radius*cos(alpha/2)
        radius*cos(pi - alpha/2)
        radius*cos(pi + alpha/2)
        radius*cos(-1.0*alpha/2)]; % x positions of the 4 rods

    y = [radius*sin(alpha/2)
        radius*sin(pi - alpha/2) + shift
        radius*sin(pi + alpha/2) + shift
        radius*sin(-1.0*alpha/2)]; % y positions of the 4 rods

else

    x = [radius*cos(alpha/2)
        radius*cos(pi - alpha/2)
        radius*cos(pi + alpha/2)
        radius*cos(-1.0*alpha/2)]; % x positions of the 4 rods

    y = [radius*sin(alpha/2) + shift
        radius*sin(pi - alpha/2)
        radius*sin(pi + alpha/2)
        radius*sin(-1.0*alpha/2) + shift]; % y positions of the 4 rods
end

% distance between the rod and the point. If the point is past the edge
% of the rod along the z axis, then this is the distance to where the
% rod would be if it were longer.
dist = [sqrt((b_pos(1)-x(1))^2+(b_pos(2)-y(1))^2)
    sqrt((b_pos(1)-x(2))^2+(b_pos(2)-y(2))^2)
    sqrt((b_pos(1)-x(3))^2+(b_pos(2)-y(3))^2)
    sqrt((b_pos(1)-x(4))^2+(b_pos(2)-y(4))^2)];

% get the angle made by the x axis and the vector pointing from the rod
% to b_pos.
phi = asin((b_pos(1) - x)./dist);

% angle between s and the line connecting the beginning of the rod to
% b_pos
theta1 = [atan((-0.5*len - b_pos(3))/dist(1))
    atan((-0.5*len - b_pos(3))/dist(2))
    atan((-0.5*len - b_pos(3))/dist(3))
    atan((-0.5*len - b_pos(3))/dist(4))];

% angle between s and the line connecting the end of the rod to b_pos
theta2 = [atan((0.5*len - b_pos(3))/dist(1))
    atan((0.5*len - b_pos(3))/dist(2))
    atan((0.5*len - b_pos(3))/dist(3))
    atan((0.5*len - b_pos(3))/dist(4))];


if image == 1
    % field contribution to the x direction is the magnitude*cos(phi). Phi
    % was calculated above.
    dBrx = (K*current/dist(1))*(sin(theta2(1)) - sin(theta1(1)))*cos(phi(1)) + ...
```

```
            (K*current*current_ratio/dist(2))*(sin(theta2(2)) - sin(theta1(2)))*cos(phi(2)) + ...
            (K*current*current_ratio/dist(3))*(sin(theta2(3)) - sin(theta1(3)))*cos(phi(3)) + ...
            (K*current/dist(4))*(sin(theta2(4)) - sin(theta1(4)))*cos(phi(4));

        % field contribution to the x direction is the magnitude*sin(phi). Phi
        % was calculated above.
        dBry = (K*current/dist(1))*(sin(theta2(1)) - sin(theta1(1)))*sin(phi(1)) + ...
            (K*current*current_ratio/dist(2))*(sin(theta2(2)) - sin(theta1(2)))*sin(phi(2)) + ...
            (K*current*current_ratio/dist(3))*(sin(theta2(3)) - sin(theta1(3)))*sin(phi(3)) + ...
            (K*current/dist(4))*(sin(theta2(4)) - sin(theta1(4)))*sin(phi(4));

    else
        % field contribution to the x direction is the magnitude*cos(phi). Phi
        % was calculated above.
        dBrx = (K*current*current_ratio/dist(1))*(sin(theta2(1)) - sin(theta1(1)))*cos(phi(1)) + ...
            (K*current/dist(2))*(sin(theta2(2)) - sin(theta1(2)))*cos(phi(2)) + ...
            (K*current/dist(3))*(sin(theta2(3)) - sin(theta1(3)))*cos(phi(3)) + ...
            (K*current*current_ratio/dist(4))*(sin(theta2(4)) - sin(theta1(4)))*cos(phi(4));

        % field contribution to the x direction is the magnitude*sin(phi). Phi
        % was calculated above.
        dBry = (K*current*current_ratio/dist(1))*(sin(theta2(1)) - sin(theta1(1)))*sin(phi(1)) + ...
            (K*current/dist(2))*(sin(theta2(2)) - sin(theta1(2)))*sin(phi(2)) + ...
            (K*current/dist(3))*(sin(theta2(3)) - sin(theta1(3)))*sin(phi(3)) + ...
            (K*current*current_ratio/dist(4))*(sin(theta2(4)) - sin(theta1(4)))*sin(phi(4));
    end

    % make a vector from the components. There is no field in the z
    % direction at any point due to the rods.
    dBr = [dBrx; dBry; 0];
end
```

### A.2.4 A Function to Read the Simulation Output File

```
% header refers to how many lines make up the header in the text file
% before the B1 data starts.

function [B1 B1x B1y B1z] = read_B1_data3(inputFile)

formatSpec = '%e %e %e %e %e %e %e';
sizeA = [7 Inf]; % 7 columns of data

fileid = fopen(inputFile)

A = fscanf(fileid,formatSpec,sizeA); % read the data in

fclose('all');

A = transpose(A); % transpose the data to make analysis easier

length = A(1,1) % first row contains coil data
radius = A(1,2)
current = A(1,3)
alpha = A(1,4)

xsteps = A(2,1) % second row contains simulation data
```

```
x_step_size = A(2,2)
ysteps = A(2,3)
y_step_size = A(2,4)
zsteps = A(2,5)
z_step_size = A(2,6)
i = 3;

B1 = zeros(xsteps,ysteps,zsteps); % the rest is the magnetic field
B1x = zeros(xsteps,ysteps,zsteps); % at each point
B1y = zeros(xsteps,ysteps,zsteps); % initialize the output data
B1z = zeros(xsteps,ysteps,zsteps);


% divide the data into the magnitude of the magnetic field
% and the field in each of the cardinal directions
for x = 1:xsteps
    for y = 1:ysteps
        for z = 1:zsteps
            B1(x, y, z) = A(i,4);
            B1x(x, y, z) = A(i,5);
            B1y(x, y, z) = A(i,6);
            B1z(x, y, z) = A(i,7);

            i = i+1;
        end
    end
end


end
```